FACULTY
OF MATHEMATICS
AND PHYSICS
Charles University

MASTER THESIS

Kristián Vitovský

Hydrodynamical simulations of circumstellar discs

Astronomical Institute of Charles University

Supervisor of the master thesis:	doc. Mgr. Miroslav Brož, Ph.D.
Study programme:	Physics
Study branch:	Astronomy and Astrophysics

Prague 2023

I declare that I carried out this master thesis independently, and only with the cited sources, literature and other professional sources. It has not been used to obtain another or the same degree.

I understand that my work relates to the rights and obligations under the Act No. 121/2000 Sb., the Copyright Act, as amended, in particular the fact that the Charles University has the right to conclude a license agreement on the use of this work as a school work pursuant to Section 60 subsection 1 of the Copyright Act.

In .... date ....

Author's signature

To my awesome invincible mother!

Title: Hydrodynamical simulations of circumstellar discs

Author: Kristián Vitovský

Institute: Astronomical Institute of Charles University

Supervisor: doc. Mgr. Miroslav Brož, Ph.D., Astronomical Institute of Charles University

Abstract: In this work, we study the dynamics of circumstellar discs, with a focus on the β Lyræ A binary system. This system has been extensively observed by photometry, spectroscopy and interferometry. All these observations were recently interpreted by a radiation-transfer kinematic model [Brož et al., 2021]. In order to apply dynamical models, we first review the theory of steady-state viscous accretion discs, including the α-parametrisation of the viscosity.

We modified the analytical models of Shakura and Sunyaev [1973] for a general opacity prescription, $\kappa = \kappa_0 \rho^A T^B$, and derived radial profiles of various quantities (Σ, T, H). The profiles were computed for the accretion rate $\dot{M} = 2 \cdot 10^{-5}\, M_\odot\, \mathrm{yr}^{-1}$, inferred from the observed rate of change of the binary period. To achieve this rate, the surface densities Σ must be much higher (of the order of $10000\,\mathrm{kg\,m^{-2}}$ for $\alpha = 0.1$) than in the kinematic model. Viscous dissipation and radiative cooling in the optically thick regime lead to high mid-plane temperatures. The disk is still gas pressure dominated.

More general models were computed numerically. We used 1-dimensional radiative hydrodynamic models [Chrenko et al., 2017], accounting for viscous, radiative as well as irradiation terms. The initial conditions were taken from the analytical models. The simulations achieved a steady state on the viscous timescale. To reconcile temperature profiles, we have to distinguish three different temperatures: mid-plane, atmospheric and irradiation. The latter two are comparable to observations (30000 to 12000 K). We demonstrate that the aspect ratio of 0.08 can be achieved in the hydrostatic equilibrium, as opposed to Brož et al. [2021] who considered the disc to be vertically unstable.

Keywords: Cirsumstellar matter Hydrodynamics Accretion discs Binary stars β Lyræ

Contents

Briefoduction

Be stars have been studied for more than 150 years, for example, the first-ever known Be stars β Lyræ has 912 references in the Simbad database. Instead o reviewing all of them, we refer the reader to the bachelor thesis ”A Study of the Long-term Brightness and Colour Variations of the Be Star 88 Herculis” [Vitovský, 2019], i.e., the author of this master thesis, where a detailed discussion of Be stars observations and various phenomena can be found.

However, the proposal of this thesis had a different focus. The first goal was to understand the theory later used for analytical and numerical models of stellar systems (see chapter 1). Namely, the eulerian hydrodynamics (section 1.1), the thin accretion discs theory (section 1.2), and one particular numerical model (section 1.3).

The second goal was to review the numerical methods, commonly used in hydrodynamical simulations (chapter 2).

The third goal was to apply the thin accretion disc theory to the β Lyræ system. Actually, we had to modify the classical analytical models [Shakura and Sunyaev, 1973], in order to obtain relevant profiles of hydrodynamical quantities and gain insight to the dynamics of the system (chapter 3).

The fourth goal was to run numerical radiative-hydrodynamic (RHD) simulations (e.g., Chrenko et al. [2017]), which includes more complex opacities and more complete physics (chapter 4).

So be it...

1. Theoretical hydrodynamics

In this thesis, we use the Eulerian hydrodynamics to study circumstellar matter around the mass-transferring β-Lyræ A star. In this section, we derive the set of Eulerian hydrodynamical equations from fundamental principles as a basis for the numerical and analytical applications later in this thesis.

1.1 Derivation of Eulerian Hydrodynamics

1.1.1 Notation

In the following derivations, we use the notation as follows:

N is the number of point-mass particles in an N-body system

$\boldsymbol{z}_i$ is a vector of generalised positional coordinates belonging to the ith particle.

$\boldsymbol{s}_i$ is a vector of generalised momenta belonging to the i-th particle.

$\boldsymbol{Z} = (\boldsymbol{z}_1, \boldsymbol{s}_1, ..., \boldsymbol{z}_N, \boldsymbol{s}_N)$ that is a vector of all positional coordinates and all momenta belonging to the N-body system.

$\boldsymbol{r}_i$ is a vector of cartesian coordinates belonging to the i-th particle.

$\boldsymbol{p}_i$ is a vector of cartesian momenta belonging to the ith particle.

$\boldsymbol{X} = (\boldsymbol{r}_1, \boldsymbol{p}_1, ..., \boldsymbol{r}_N, \boldsymbol{p}_N)$ that is a vector of all cartesian positional coordinates and all momenta belonging to the N-body system.

The following commentary on the derivation of the Eulerian hydrodynamics was based on the NAST008 lectures given at the Astronomical institute of the Faculty of Mathematics and Physics of Charles University [Šubr and Švanda] and the book Landau and Lifshitz.

1.1.2 Luioiville's Equation and the Distribution Function

Let us first summarize the derivation of Eulerian Fluid equations from the first principles. Our goal here isn't an absolute mathematical validity but a clarification of assumptions adopted in the Eulerian hydrodynamics.

Definition 1 (Distribution function)**.** *We define the distribution function $D_N = D_N(\boldsymbol{Z})$ of an N-point mass particle system via its relation to the probability $P(\Omega)$ of the system being found in a fixed subset Ω of the phase space;*

$$P(\Omega) = \int_{\Omega} D_N \mathrm{dZ} \tag{1.1}$$

The distribution function plays the role of density in what we may call the *fluid of states* in a useful analogy. *Liouvilles's theorem* states that an element of the fluid of states does not change its volume as the system evolves in time. This incompressibility means that only the fluid's flow through the boundaries of an arbitrary subset Ω of phase space can change $P(\Omega)$. This is true for arbitrarily small Ω, hence we get:

$$\frac{\partial D_N}{\partial t} = -\nabla \cdot (D_N \dot{\boldsymbol{Z}}), \tag{1.2}$$

where $\dot{Z}$ is the generalized momentum. The Hamiltonian canonical equations imply that this can be rewritten using the Poisson brackets as:

$$\frac{\partial D_N}{\partial t} = \{\mathcal{H}, D_N\}_P \tag{1.3}$$

where $\mathcal{H}$ is the Hamiltonian of the system. This is the most common form of the *Liouvilles's equation* and it will serve as a starting point in our derivation.

In cases that are of interest all particles of the system are indistinguishable, hence a reduced distribution function $f(\boldsymbol{z}_1, \boldsymbol{s}_1))$ will give the probability density of any single particle of the system.

Definition 2 (Reduced distribution fuction). *The probability density of any single particle of the system is given by the* Reduced Distribution Function $f(\boldsymbol{z}_1, \boldsymbol{s}_1)$*, that is obtained by averaging the distribution function D_N of the system:*

$$f(\boldsymbol{z}_1, \boldsymbol{s}_1) = \frac{1}{(N-1)!} \int_{PS} D_N(\boldsymbol{Z}) d^3\boldsymbol{z}_2 d^3\boldsymbol{s}_2 ... d^3\boldsymbol{z}_N d^3\boldsymbol{s}_N. \tag{1.4}$$

Here we chose to leave coordinates with $i = 1$ out of the integration, we emphasize that this is an arbitrary choice that only plays a role in the notation, this is because our particles are indistinguishable. In a more general case where D_N would not be symmetric in particle permutation, we would get a different single-particle distribution function for each particle.

1.1.3 Boltzmann Equation

We now choose specific types of coordinates:

$$\boldsymbol{z}_i \to \boldsymbol{r}_i, \qquad \boldsymbol{s}_i \to \boldsymbol{p}_i,$$

In these new coordinates, we now assume a specific separable form of the Hamiltonian.

$$\mathcal{H} = \sum_{i=1}^{\mathrm{N}} \frac{\boldsymbol{p}_i^2}{2m} + \sum_{i=1}^{\mathrm{N}} V\left(\boldsymbol{r}_i\right) + \sum_{i=1}^{\mathrm{N}} \sum_{\substack{j=1 \\ j\neq i}}^{\mathrm{N}} w\left(\boldsymbol{r}_i, \boldsymbol{r}_j\right), \tag{1.5}$$

where m is the mass of one particle, $V(\boldsymbol{r})$ is the external potential and $w(\boldsymbol{r}_i, \boldsymbol{r}_j)$ is the interaction term. Here we must emphasize, that the choice of a system is from now on truly constrained and we have lost generality. We further define single-particle Hamiltonian h the part of the chosen hamiltonian that corresponds to a single particle, that is:

$$h(\boldsymbol{r}_i, \boldsymbol{p}_i) \equiv \frac{\boldsymbol{r}_i^2}{2m} + V(\boldsymbol{r}_i) \tag{1.6}$$

We rewrite the Liouvilles's equation using the definition of Poisson brackets and the assumed Hamiltonian, we get:

$$\frac{\partial D_{\mathrm{N}}}{\partial t} = \sum_{i=1}^{\mathrm{N}} \left(\frac{\partial D_{\mathrm{N}}}{\partial \boldsymbol{p}_i} \cdot \frac{\partial h}{\partial \boldsymbol{r}_i} - \frac{\partial D_{\mathrm{N}}}{\partial \boldsymbol{r}_i} \cdot \frac{\partial h}{\partial \boldsymbol{p}_i} \right) + \sum_{i,j} \frac{\partial w\left(\boldsymbol{r}_i, \boldsymbol{r}_j\right)}{\partial \boldsymbol{r}_i} \cdot \frac{\partial D_{\mathrm{N}}}{\partial \boldsymbol{p}_i} \tag{1.7}$$

where

- $\mathcal{H} \to h$ because only the i-th particle denpends on the $\boldsymbol{r}_i, \boldsymbol{p}_i$.
- w does not depend on p_i.

Now we will integrate the whole equation over the whole phase-space in all but one pair of phase space coordinates (note the appropriate normalisation), for orderliness we will comment on each term separately:

LHS; We switch the order of integration and partial differentiation, hence we can use the definition of the reduced distribution function:

$$\begin{aligned} &\frac{1}{(N-1)!} \int_{PS} \frac{\partial D_{\mathrm{N}}}{\partial t} d^3\boldsymbol{r}_2 d^3\boldsymbol{p}_2 ... d^3\boldsymbol{r}_N d^3\boldsymbol{p}_N = \\ &\qquad = \frac{1}{(N-1)!} \frac{\partial}{\partial t} \int_{PS} D_{\mathrm{N}} d^3\boldsymbol{r}_2 d^3\boldsymbol{p}_2 ... d^3\boldsymbol{r}_N d^3\boldsymbol{p}_N = \\ &\qquad\qquad = \frac{\partial f(\boldsymbol{r}_1 . \boldsymbol{p}_1)}{\partial t} \end{aligned} \tag{1.8}$$

The order of mathematical operations can be switched if D_N and $\frac{\partial D_\mathrm{N}}{\partial t}$ are both continuous in phase-space. We omit proving this rigorously and simply state that these are reasonable assumptions about systems, that we are interested in.

RHS 1. term; We can split the sum in two different parts.

1. The coordinates which we differentiate by are those corresponding to the chosen particle (that is, the ones we do not integrate over); the partial differentiation of the single particle hamiltonian behaves as a constant with respect to the integral and we can (under similar assumptions as on the LHS) switch the order of integration and differentiation of D_N, hence we get:

$$\begin{aligned}&\frac{\partial h}{\partial \boldsymbol{r}_1}\int_{PS}\frac{\partial D_\mathrm{N}}{\partial \boldsymbol{p}_1}d^3\boldsymbol{r}_2d^3\boldsymbol{p}_2...d^3\boldsymbol{r}_Nd^3\boldsymbol{p}_N\\ &\qquad\qquad -\frac{\partial h}{\partial \boldsymbol{p}_1}\int_{PS}\frac{\partial D_\mathrm{N}}{\partial \boldsymbol{r}_1}d^3\boldsymbol{r}_2d^3\boldsymbol{p}_2...d^3\boldsymbol{r}_Nd^3\boldsymbol{p}_N\\ &\qquad\qquad\qquad\qquad =\frac{\partial h}{\partial \boldsymbol{r}_1}\cdot\frac{\partial f}{\partial \boldsymbol{p}_1}-\frac{\partial h}{\partial \boldsymbol{p}_1}\cdot\frac{\partial f}{\partial \boldsymbol{p}_1}.\end{aligned} \tag{1.9}$$

   we now use the Hamilton's canonical equations and arrive at:

$$\frac{\partial h}{\partial \boldsymbol{r}_1}\cdot\frac{\partial f}{\partial \boldsymbol{p}_1}-\frac{\partial h}{\partial \boldsymbol{p}_1}\cdot\frac{\partial f}{\partial \boldsymbol{r}_1}=-\dot{\boldsymbol{p}}_1\cdot\frac{\partial f}{\partial \boldsymbol{p}_1}-\dot{\boldsymbol{r}}_1\cdot\frac{\partial f}{\partial \boldsymbol{r}_1}. \tag{1.10}$$

2. The rest of the sum can be broken down into sub-integrals of shape:

$$\iint\left(\frac{\partial D_\mathrm{N}}{\partial \boldsymbol{p}_i}\cdot\frac{\partial h}{\partial \boldsymbol{r}_i}-\frac{\partial D_\mathrm{N}}{\partial \boldsymbol{r}_i}\cdot\frac{\partial h}{\partial \boldsymbol{p}_i}\right)\mathrm{d}^3\boldsymbol{r}_i\ \mathrm{d}^3\boldsymbol{p}_i. \tag{1.11}$$

   We can approach the integration of each i-th term of the sum analogously, we will integrate the first product per partes with respect to $\boldsymbol{p}_i$ and the second product with respect to $\boldsymbol{r}_i$. Each per partes integration produces a boundary term with D_N, when integrating over all of the phase space these boundary terms must be zero because $D_N \to 0$ as the phase space coordinate goes to infinity for any physically relevant system. We are left with:

$$-\iint D_\mathrm{N}\frac{\partial h}{\partial \boldsymbol{r}_i\partial \boldsymbol{p}_i}\ \mathrm{d}^3\boldsymbol{r}_i\ \mathrm{d}^3\boldsymbol{p}_i+\iint D_\mathrm{N}\frac{\partial h}{\partial \boldsymbol{p}_i\partial \boldsymbol{r}_i}\ \mathrm{d}^3\boldsymbol{r}_i\ \mathrm{d}^3\boldsymbol{p}_i. \tag{1.12}$$

   We see that the two terms cancel out if can switch the order of partial differentiation of h, this is valid if both second derivatives of h are continuous; again without rigorous proof we state, that this will be the case for single particle hamiltonians of physically relevant systems.

RHS 2. term; The last term has the form:

$$\frac{(N-1)}{(N-1)!}\int_{PS}\sum_{i,j}\frac{\partial w\left(\boldsymbol{r}_i,\boldsymbol{r}_j\right)}{\partial \boldsymbol{r}_i}\cdot\frac{\partial D_\mathrm{N}}{\partial \boldsymbol{p}_i}d^3\boldsymbol{r}_2d^3\boldsymbol{p}_2...d^3\boldsymbol{r}_Nd^3\boldsymbol{p}_N. \tag{1.13}$$

Only the $(N-1)$ terms where i =1 will be non-zero (i =1 represents the chosen particle in our notation), this is due to $\frac{\partial w(r_i,r_j)}{\partial r_i}$ being independent of momenta, hence it behaves as a constant when integrating with respect to momenta, we get the sub integral:

$$\int_{PS}\frac{\partial D_\mathrm{N}}{\partial \boldsymbol{p}_i}d^3\boldsymbol{p}_i=[D_N]_{\boldsymbol{p}_i\to\infty}\to 0. \tag{1.14}$$

Again we used the aforementioned condition for boundaries. The particles are *undistuguashable*, hence the $(N-1)$ of them will be all equivalent and independent of index j, for example, choose $j=2$ as the index of the second particle in the interaction. We are left with

$$\frac{(N-1)}{(N-1)!}\int_{PS}\frac{\partial w\left(\boldsymbol{r}_1,\boldsymbol{r}_2\right)}{\partial \boldsymbol{r}_1}\cdot\frac{\partial D_\mathrm{N}}{\partial \boldsymbol{p}_1}d^3\boldsymbol{r}_2d^3\boldsymbol{p}_2...d^3\boldsymbol{r}_Nd^3\boldsymbol{p}_N. \tag{1.15}$$

Let us focus on the sub-integral:

$$\frac{(N-1)}{(N-1)!}\int_{PS}\frac{\partial D_{\mathrm{N}}}{\partial \boldsymbol{p}_1}d^3\boldsymbol{r}_3 d^3\boldsymbol{p}_3 ... d^3\boldsymbol{r}_N d^3\boldsymbol{p}_N$$
$$= \frac{1}{(N-2)!}\frac{\partial}{\partial \boldsymbol{p}_1}\int_{PS} D_{\mathrm{N}} d^3\boldsymbol{r}_3 d^3\boldsymbol{p}_3 ... d^3\boldsymbol{r}_N d^3\boldsymbol{p}_N$$
$$= \frac{\partial f_2}{\partial \boldsymbol{p}_1}. \quad (1.16)$$

Where we first switched the order of integration and differentiation again (under the same aforementioned assumptions) and then implicitly defined the two-particle distribution function (which describes the probability density of any two particles) analogous to the single-particle distribution function. We plug this result back into the whole integral, we are left with:

$$\int_{PS}\frac{\partial w\left(\boldsymbol{q}_1,\boldsymbol{q}_2\right)}{\partial \boldsymbol{q}_1}\cdot\frac{\partial f_2}{\partial \dot{\boldsymbol{q}}_1}\mathrm{d}^3\boldsymbol{q}_2\mathrm{d}^3\dot{\boldsymbol{q}}_2 \overset{\text{notation}}{=} \left(\frac{\partial f}{\partial t}\right)_{\text{collisions}}. \quad (1.17)$$

we call the leftover integral the *collisional term* and define here a typical notation for it. The collisional term contains an integration of f_2 and there isn't anything else we can do in this term exactly, that is without using approximations.

Since the indexes have now lost meaning, it is practical to modify our notation:

$$\boldsymbol{r}_1 \equiv \boldsymbol{r}, \qquad \boldsymbol{p}_1 \equiv \boldsymbol{p}, \qquad \dot{\boldsymbol{p}}_1 \equiv \dot{\boldsymbol{p}}.$$

In this new notation, we plug in all the terms:

$$\boxed{\frac{\partial f}{\partial t}+\dot{\boldsymbol{p}}\cdot\frac{\partial f}{\partial \boldsymbol{p}}+\dot{\boldsymbol{r}}\cdot\frac{\partial f}{\partial \boldsymbol{r}}=\left(\frac{\partial f}{\partial t}\right)_{\text{collisions}}.} \quad (1.18)$$

We arrived at the *Boltzmann equation*, which gives the evolution of the single-particle distribution function. If we also consider Newton's second law we can further modify the second term on the left hand side by introducing the *external forces* $\boldsymbol{\mathcal{F}}$:

$$\frac{\partial f}{\partial t}+\boldsymbol{\mathcal{F}}\cdot\frac{\partial f}{\partial \boldsymbol{p}}+\dot{\boldsymbol{r}}\cdot\frac{\partial f}{\partial \boldsymbol{r}}=\left(\frac{\partial f}{\partial t}\right)_{collisions} \quad (1.19)$$

1.1.4 Vlasov Approximation and Vlasov equation

Our goal is to obtain an equation which is easier to solve than Luoiville's equation, to this end we will have to accept approximations for f_2. Let us split f_2 to a sum of two terms:

$$f_2 = f_{2_{un}} + f_{2_{corr}} \quad (1.20)$$

where $f_{2_{un}}$ corresponds to the distribution function of *uncorrelated* events and $f_{2_{corr}}$ to the distribution function of *correlated* events. Naturally, the probability density of uncorrelated events is given by:

$$f_{2_{un}}(\boldsymbol{r}_1,\boldsymbol{r}_2,\boldsymbol{p}_1,\boldsymbol{p}_2) = f(\boldsymbol{r}_1,\boldsymbol{p}_1)\cdot f(\boldsymbol{r}_2,\boldsymbol{p}_2). \quad (1.21)$$

Note that the typical event here in question is finding two particles at two pairs of phase space coordinates.

Approximation 1 (Vlasov approximation)**.** *Under the assumptions that f_2 can be calculated as a superposition of $f_{2_{un}}$ and $f_{2_{corr}}$ and that $f_{2_{un}} \gg f_{2_{corr}}$holds; we choose to neglect $f_{2_{corr}}$ in f_2, hence:*

$$f_2(\boldsymbol{r}_1,\boldsymbol{r}_2,\boldsymbol{p}_1,\boldsymbol{p}_2) = f(\boldsymbol{r}_1,\boldsymbol{p}_1)\cdot f(\boldsymbol{r}_2,\boldsymbol{p}_2). \quad (1.22)$$

We will now investigate what shape the collision term takes under the Vlasov approximation:

$$\begin{aligned}\left(\frac{\partial f}{\partial t}\right)_{collisions} &= \int_{PS} \frac{\partial w\left(\boldsymbol{r}_1, \boldsymbol{r}_2\right)}{\partial \boldsymbol{r}_1} \frac{\partial f(\boldsymbol{r}_1, \boldsymbol{p}_1)}{\partial \boldsymbol{p}_1} f\left(\boldsymbol{r}_2, \boldsymbol{p}_2\right) \mathrm{d}^3\boldsymbol{r}_2 \mathrm{d}^3\boldsymbol{p}_2 \\ &= \frac{\partial f(\boldsymbol{r}_1, \boldsymbol{p}_1)}{\partial \boldsymbol{p}_1} \frac{\partial}{\partial \boldsymbol{r}_1} \int_{PS} w\left(\boldsymbol{r}_1, \boldsymbol{r}_2\right) f\left(\boldsymbol{r}_2, \boldsymbol{p}_2\right) \mathrm{d}^3\boldsymbol{r}_2 \mathrm{d}^3\boldsymbol{p}_2. \qquad (1.23)\end{aligned}$$

once again, we switched the order of mathematical operations, and once again we omitted a formal proof, that this is possible. We further note that $w\left(\boldsymbol{r}_1, \boldsymbol{r}_2\right)$ is the interaction energy between two particles, that is the potential energy of one single particle in the force field of another particle. Hence the last integral which is a ”continuous sum” of all contributors of one test particle's potential energy represents the complete potential field $\phi(\boldsymbol{r})$ created by force fields of all particles. Plugging back in we get the collision term:

$$\left(\frac{\partial f}{\partial t}\right)_{collisions} = \frac{\partial f(\boldsymbol{r}_1, \boldsymbol{p}_1)}{\partial \boldsymbol{p}_1} \frac{\partial}{\partial \boldsymbol{r}_1} \left(\phi(\boldsymbol{r}_1)\right). \qquad (1.24)$$

Now, we will assume that $\mathcal{F}$ in eq. 1.19 can be expressed as the gradient of some scalar potential field:

$$\mathcal{F} = -\frac{\partial}{\partial \boldsymbol{r}} \left(V(\boldsymbol{r})\right). \qquad (1.25)$$

Again this is a reasonable assumption for $\mathcal{F}$ because a typical example of an external force field will be the gravitational field (in systems relevant to this thesis: the gravity of stars in a binary system). We can now plug the collision term under the Vlasov approximation and our assumption about $\mathcal{F}$ into eq. 1.19.

$$\boxed{\frac{\partial f}{\partial t} + \dot{\boldsymbol{r}} \cdot \frac{\partial f}{\partial \boldsymbol{r}} - \frac{\partial}{\partial \boldsymbol{r}} \left(V(\boldsymbol{r}) + \phi(\boldsymbol{r})\right) \cdot \frac{\partial f}{\partial \boldsymbol{p}} = 0.} \qquad (1.26)$$

We arrived at the *Vlasov equation* which is a specific case of the Boltzmann equation. Under our assumed Hamiltonian, Hamilton's canonical equations give a simple relation between velocities $\dot{\boldsymbol{r}} \equiv \boldsymbol{u}$ and momenta $\boldsymbol{p} = m\boldsymbol{u}$, hence we can express the Vlasov equation in velocities instead of momenta, we get:

$$\frac{\partial f}{\partial t} + \boldsymbol{u} \cdot \frac{\partial f}{\partial \boldsymbol{r}} - \frac{1}{m} \frac{\partial}{\partial \boldsymbol{r}} \left(V(\boldsymbol{r}) + \phi(\boldsymbol{r})\right) \cdot \frac{\partial f}{\partial \boldsymbol{u}} = 0 \qquad (1.27)$$

1.1.5 Eulerian Hydrodynamics

The Vlasov equation still contains very detailed information; it describes (under the specified approximations) the evolution of the single-particle distribution function. For systems relevant to this thesis (fluids), where N is very high and the influence of individual particles can be neglected, it is more useful to view the N-point mass system as an entity contentious in space and neglect its microscopic structure. To describe this entity we assign quantities corresponding to particles local in space and average over the velocity dimension of the phase-space, hence we lose the dependency on the velocities of particles. Note here that from a mathematical point of view our description was already continuous because we took a statistical approach and described particles by continuous distribution functions. We could say that the change in approach here lies in starting to view the system as continuous also in the sense of a physical model. Let us first list quantities which will be used to describe fluid.

- Average local **mass density** ρ of a fluid element:

  $$\rho \equiv \int_{-\infty}^{\infty} m \cdot f(\boldsymbol{r}, \boldsymbol{u}) d^3\boldsymbol{u}. \qquad (1.28)$$

  We state that m is the mass of a single particle and f gives the probability density of a single particle, so this way of introducing density is quite intuitive.

- **Velocity** v of a fluid element:

$$\rho \boldsymbol{v} \equiv \int_{-\infty}^{\infty} m\boldsymbol{u} \cdot f(\boldsymbol{r}, \boldsymbol{u}) d^3\boldsymbol{u} \tag{1.29}$$

  we average out all random motion of local particles and arrive at the systematic bulk motion of particles in a fluid element.

- **Internal energy per fluid mass element** ϵ:

$$\rho\epsilon \equiv \int_{-\infty}^{\infty} \frac{1}{2} m|\boldsymbol{u} - \boldsymbol{v}|^2 \cdot f(\boldsymbol{r}, \boldsymbol{u}) d^3\boldsymbol{u}. \tag{1.30}$$

  This time only the kinetic energy due to random motion of local particles is added up. ϵ will clearly be related to the local temperature T of the fluid.

The set of equations themselves is again obtained by reducing the information contained in the Vlasov equation by averaging, this is done by taking the zeroth, first and second moment of the Vlasov equation in the velocity dimension. That is:

$$\begin{matrix} \text{Continuity eq.} \\ \text{Euler eq.} \\ \text{Energy eq.} \end{matrix} \equiv \begin{matrix} \text{zeroth m.} \\ \text{first m.} \\ \text{third m.} \end{matrix} \equiv \int_{-\infty}^{\infty} \begin{pmatrix} m \\ m\boldsymbol{u} \\ \frac{1}{2}m|\boldsymbol{u}|^2 \end{pmatrix} \cdot [\text{Vlasov equation}]\, d^3\boldsymbol{u} \tag{1.31}$$

The step-by-step derivations of each equation does not reveal anything useful to this thesis, so they are omitted here. We simply introduce each equation in its final form and clarify new quantities that play a role in them.

1.1.5.1 Continuity equation

The zeroth moment of the Vlasov equation yields:

$$\boxed{\frac{\partial\rho}{\partial t} + \nabla \cdot (\rho\boldsymbol{v}) = 0} \tag{1.32}$$

which is a form of mass conservation law.

1.1.5.2 Euler equation

The role of the equation of motion is played by the first moment:

$$\boxed{\frac{\partial\boldsymbol{v}}{\partial t} + (\boldsymbol{v} \cdot \boldsymbol{\nabla})\boldsymbol{v} = \sum_{k}^{\#forces} \boldsymbol{F}_k - \frac{1}{\rho}\boldsymbol{\nabla}P + \frac{1}{\rho}\boldsymbol{\nabla} \cdot \boldsymbol{\pi}} \tag{1.33}$$

Here we have introduced some new quantities:

$\boldsymbol{F}_k$ are external forces acting on the fluid element.

P represents the pressure and $\boldsymbol{\pi}$ the stress tensor. Where do we get them from? The integration of the second term produces (under the Nabla operator) $\rho\langle u_i u_j\rangle$ written element-wise, that is u_i representing the ith element of a particles velocity vector, angle brackets correspond to the averaging integral. We write the particle's velocity as the superposition of the local bulk velocity v and thermal (random) component (δv). Hence:

$$\begin{aligned} \langle v_i v_j\rangle = \langle (v_i + \langle(\delta v)_i\rangle)(v_j + \langle(\delta v)_j\rangle)\rangle \\ = v_i v_j + v_i\langle(\delta v)_j\rangle + v_j\langle(\delta v)_i\rangle + \langle(\delta v)_i(\delta v)_j\rangle \\ = v_i v_j + \langle(\delta v)_i(\delta v)_j\rangle \end{aligned} \tag{1.34}$$

this is clearly true, because $\langle(\delta v)_i\rangle = 0$ must be true by definition. $v_i v_j$ produces $(\boldsymbol{v} \cdot \boldsymbol{\nabla})\boldsymbol{v}$ in the final equation. We are left with the tensor: $\langle(\delta v)_i(\delta v)_j\rangle$, we split it into two parts:

1. its trace, which leads us to the definition of pressure:

$$P \overset{\text{def.}}{\equiv} \frac{1}{3}\rho\langle\sum_{i}^{i=3}(\delta v)_i^2\rangle. \tag{1.35}$$

   That is if we imagine an elementary cube the fluid, pressure is connected to the momentum flux in directions perpendicular to the cube's faces. Here we may also emphasize that this way of introducing pressure consistently straight from the definition gives:

$$\rho\epsilon \equiv \frac{1}{2}\rho\langle|(\boldsymbol{\delta v})|^2\rangle \equiv \frac{3}{2}P. \tag{1.36}$$

2. what is left is a traceless tensor, that is the stress tensor $\boldsymbol{\pi}$:

$$\pi_{ij} \overset{\text{def.}}{\equiv} \rho\langle\left(\frac{1}{3}\sum_{i}^{i=3}(\delta v)_i^2\right)\delta_{ij} - ((\delta v)_i(\delta v)_j)\rangle. \tag{1.37}$$

   That again in reference to an elementary cube of the fluid; the stress tensor is connected to momentum flux in directions tangential to the faces of the cube. We note, that the choice of a sign is only a matter of definition.

1.1.5.3 Energy equation

The second moment gives:

$$\boxed{\rho\frac{\mathrm{d}\epsilon}{\mathrm{d}t} = -P\nabla\cdot\boldsymbol{v} - \boldsymbol{\nabla}\cdot\boldsymbol{\mathcal{C}} + \mathcal{D},} \tag{1.38}$$

where we have again introduced the pressure as before and:

- From a microscopic point of view the random flux of momentum carried by particles undergoing thermal motions is a the of conductivity, hence we define:

$$\boldsymbol{\mathcal{C}} \overset{def.}{\equiv} \frac{1}{2}\rho\langle(\boldsymbol{\delta v})|(\boldsymbol{\delta v})|^2\rangle. \tag{1.39}$$

- Momentum exchange between fluid elements causes energy dissipation in the fluid:

$$\mathcal{D} = \pi_{ij}\frac{\partial v_i}{\partial r_j}. \tag{1.40}$$

  that is the *local dissipation measure $\mathcal{D}$*.

1.2 Basic Theory of Thin Accretion Discs

The centre of mass of this thesis is an accretion disc. In this section, we summarize the standard basic theory connected to so-called "thin accretion discs". The relations introduced here will later be used to build the numerical model.

1.2.1 Thin disc approximation

Let us first introduce what we mean by a thin accretion disc and the assumptions that we make in our theoretical model.

Assumption 1 (Gravity well and cylindrical symmetry)**.** *We assume a gravitational potential well generated by a central spherical object. We place rotating gas in such a well. We assume that the gas takes a shape with cylindrical symmetry, where the axis of symmetry is parallel to the angular momentum vector of the gas.*

It seems sensible to start using the word disc already at this point. We do not give a strict definition for the term disc and leave it as an intuitive title, we do not imply that assumption 1 must necessarily hold for the term disc to make sense. For example, later in this thesis, we will inspect circumstellar matter, where cylindrical symmetry is ruined because of the presence of another gravitating body. We may think of many systems in an analogy to perturbation theories the standard model that we are beginning to describe will determine the main structure of the disc with added elements (like a binary companion) causing deviations from this state.

Assumption 2 (Timescales of redistribution)**.** *We assume that in our system the timescale on which angular momentum is redistributed between the particles is much longer than the timescale on which energy is dissipated and the orbital period. That is we can expect that when angular momentum redistribution happens, the energy is already caught up [Pringle, 1981].*

We further assume that the timescale of interest in our inspections is short enough that the change of mass of the central object $\dot{M}_\star$ *as a result of accretion is negligible [Pringle, 1981].*

$$\dot{M}_\star \approx 0 \tag{1.41}$$

We will later show 2 that assumption two is consistent with the theory of thin accretion discs. Assumption 2 is also needed for the following consideration to hold.

Assumption 3 (Azimuthal and radial velocity of fluid elements.)**.** *We assume that the orbital velocity* v_θ *is much larger than the radial velocity* v_R *in the disc [Karas, 1996];*

$$v_R \ll v_\theta \tag{1.42}$$

We note that 2 and 3 are clearly not independent.

1.2.2 Flattening and circularisation

Why is assumption 1 or the term disc viable from the physical point of view? Let us first imagine a cloud of gas spread approximately spherically around a spherical gravitating body, which will attract cells of the gas cloud. In a general situation cells of the cloud will have a non-zero angular momentum $\boldsymbol{l_p}$ with respect to the central object.

$$\boldsymbol{l_p}^a \overset{def.}{\equiv} \boldsymbol{r}^a \times \boldsymbol{p}^a \tag{1.43}$$

where $\boldsymbol{r}$ is the positional vector with respect to the centre of the central body, $\boldsymbol{p}$ again represents the cells's momentum and index $a = 1, ..., N$ with N being the number of cells constituting the gas cloud. We note here, that cells are objects of a non-infinitesimal size.

Angular momentum of an isolated system is conserved

If we first consider just one isolated cell placed into orbit as here described, we see that due to the conservation of angular momentum it will not be accreted onto the central object until a means of extracting its angular momentum is introduced and it will stay on a Keplerian orbit. If such a means of gradually extracting the cells's angular momentum is introduced it will gradually spiral into the potential well releasing the cell's potential energy and so another question arises; what can happen to this energy?

The cloud's complete angular momentum $\boldsymbol{L_{cloud}}$ is given by a superposition of all cells' angular momenta.

$$\boldsymbol{L_{cloud}} = \sum_{a=1}^{a=N} \boldsymbol{l_p}^a \tag{1.44}$$

$\boldsymbol{L_{cloud}}$ will in a realistic situation be again non-zero: $\boldsymbol{L_{cloud}} \neq \boldsymbol{0}$. Reagrding a cloud as we have set it up here we can expect two things to happen:

1. **Flattening.** At first, we can imagine individual cells in a multitude of different Keplerian orbits, from a local point of view with almost no preference of direction. In such a gas cloud cells with intersecting Keplerian orbits will collide. Each collision means an exchange of angular momentum. On the global scale of the cloud where a large number of such collisions happen this means:

    - If we set up an orthogonal system with a base defined by $\boldsymbol{L_{cloud}}/|\boldsymbol{L_{cloud}}|$ and an elementary vectors perpendicular to it; components of $\boldsymbol{l_p^a}$ that are perpendicular $\boldsymbol{L_{cloud}}$ will in time with many collisions cancel out.
    - Components of $\boldsymbol{l_p}$ parallel to $\boldsymbol{L_{cloud}}$ and components antiparallel to $\boldsymbol{L_{cloud}}$ of $\boldsymbol{l_p}$ will add up. Excess of parallel components will cancel out exactly with antiparallel components. This of course decides if the final system rotates in a clockwise or anticlockwise direction.

    hence we end up with cells orbiting close to the plane perpendicular to $\boldsymbol{L_{cloud}}$ and only in one direction determined by the orientation of $\boldsymbol{L_{cloud}}$.

2. **Circularisation**. Let us consider a conclusion from the two body problem [Wie, 1998]; specific total energy $\mathcal{E}_{tot}$ of an Keplerian orbit is given my:

    $$\mathcal{E}_{tot} = -\frac{1}{2}\frac{[G(M_\star + m_p)]^2}{|\boldsymbol{l_p}|^2}(1 - e^2) \tag{1.45}$$

    where $M_\star$ is the mass of the central object, m_p mass of the cell, e eccentricity of the cells's orbit and l_p the cells specific angular momentum. This equation implies that for a given angular momentum a circular orbit has the lowest energy. In a gas cloud, the energy of cells will undergo dissipation (due to work done by viscous forces, as discussed later), hence the orbits of cells will be circularized.

Hence we see that the rather general system which we started with will tend toward a disc-like configuration with circular orbits.

Discs can come in many shapes and sizes, we will concentrate on a specific configuration.

Assumption 4 (The disc is thin)**.** *Given that R represents the disc's extent in the radial direction and H the disc's thickness, that is extent in the direction parallel to $\mathbf{L_{cloud}}$ (we will comment on what we mean by the extent of the disc in a specific direction later and ask the reader to take it at this point as an intuitive measure), we assume that the disc is thin, that is:*

$$H \ll R \tag{1.46}$$

Assumption 5 (The disc's mass is negligible)**.** *When considering the shape of the potential well we assume that it is determined by the central body with mass $M_\star$. That is for the mass of the disc M_{disc} the following holds:*

$$M_\star \gg M_{\mathrm{disc}} \tag{1.47}$$

hence we can neglect M_{disc}.

1.2.3 Angular momentum and accretion

What role do discs play in the accretion process itself?

> *The essential connection between accretion and disc-like structures; the discs provide the necessary mechanisms for the redistribution of angular momentum and transfer of energy, that allow some particles to fall onto the accreting body.*

The term *viscosity* is used to describe the sum of processes that lead to the change and redistribution of angular momentum in a disc [Pringle, 1981].

1.2.4 Viscosity

We will first comment on the enigmatic nature of viscosity and subsequently, describe the role it plays on the macroscopic scale of discs as well as how we can approach it in a practical manner.

In the first approach, we may think about viscosity in analogy with solids as the measure of friction between adjacent layers; for example, a viscous liquid flowing through a cylindrical pipe has a higher bulk velocity in the middle of the pipe and will gradually decrease towards the wall of the pipe, this gradient is due to interactions between layers of the fluid, the measure of these interactions will be viscosity. As we will show later in more detail these interactions lead to an exchange of angular momentum between layers and on a macroscopic scale to the redistribution of angular momentum in the disc. The meaning of the word viscosity is not universal in scientific literature. Sometimes the term refers only to so-called molecular viscosity, that is interaction between layers caused solely by random motions of particles, and sometimes it is used as a value representing the complete measure of angular momentum transfer between layers of the fluid. In this thesis, we use this term in the latter meaning.

1.2.4.1 Local scale

There are several possible sources of viscosity on the local level and in truth, their relative importance in accretion discs remains an open question. Estimates show that the molecular viscosity in the considered conditions would lead to timescales of redistribution of angular momentum in typical discs far longer than the age of the universe [Karas, 1996]. Convection within the disc has also been considered as the main mechanism, but models show that even though convection is possible for discs of a lower temperature it cannot be the leading source of viscosity [Pringle, 1981]. Modelling of Keplerian disc shows that convection leads to negligible or inward angular momentum transport for Keplerian discs [Balbus et al., 1996].

Observed accretion rates along with other considerations about observed discs indicate that turbulence could be a viable candidate to support angular momentum transfer at the necessary rate. First, let us consider turbulence arising from hydrodynamical instability.

- Instabilities such as eddies of different scales cause a systematic intrusion of particles from one layer of the fluid into another. In a simple model, such turbulence implies that there will be some motion perpendicular to the main streamlines, hence particles will come into contact with particles corresponding to a different streamline.

  It is questionable whether such turbulence occurs [Pringle, 1981].

  Criterion 1 (Rayleigh criterion for stability)**.** *The system is hydrodynamically stable if:*

  $$\frac{\partial(r^2\Omega(r))}{\partial r} > 0 \tag{1.48}$$

  where r is the distace from the rotational axis and $\Omega(r)$ the angular velocity at r.

  We will inspect this criterion under the assumption of a Keplerian disc, as is approximately the case for circumstellar discs in Be star binary systems [Rivinius et al., 2013]. Circular orbits of particles can be approximated by trajectories determined by the equilibrium of the centrifugal force and gravity:

  $$\Omega_K^2 r = -\frac{d\Phi}{dr} = \frac{GM_\star}{r^2} \implies \Omega_K = \sqrt{\frac{GM_\star}{r^3}} \tag{1.49}$$

hence applying the criterion:

$$\frac{\partial \Omega_K r^2}{\partial r} = \sqrt{\frac{GM_\star}{2r}} > 0 \tag{1.50}$$

If we further consider a more general profile of Ω with a simple dependence on r in the form of $\Omega \propto r^{-\xi}$, then the criterion gives us stability for $\xi < 4$. The criterion implies stability for most discs.

An often-cited candidate for a driver of angular momentum exchange is magneto-rotational instability.

- Balbus and Hawley [1991] showed that the conditions for the magneto-rotational instability to occur are met for a wide range of discs. All that is needed is a decreasing radial angular velocity dependency;

  $$\frac{\partial \Omega(r)}{\partial r} < 0 \tag{1.51}$$

  and a weak poloidal magnetic field. 3D simulations by Arlt and Rüdiger [2001] showed that the instability is indeed a functional mechanism to cause turbulent flows in Keplerian discs that translate to viscous angular momentum redistribution.

1.2.4.2 Global scale

Let us now turn to the global scale of the problem. To summarise what has already been partially hinted at:

- For matter orbiting a gravitating body to fall into its potential well and in an extreme case onto the body, it must lose its angular momentum.
- If the matter is part of a viscous disc around the central body, viscous forces will arise between adjacent layers of the fluid leading to angular moment exchange.
- Angular momentum from the inner (closer to the central body) parts of the disc will be transported outwards. Except for the leftover angular momentum of fluid elements falling onto the central body the complete sum of all angular momentum in an isolated disc is conserved.
- Fluid elements that lose enough of their angular momentum will fall onto a more inner circular orbit, that is deeper into the gravitational potential well, hence some of their gravitational potential energy is freed.

Let us imagine our axiosymmetric discs as a set of concentric rings around the central body. Each ring has a radius of R and rotates around the axis of rotation with $\Omega(R)$, the thickness of each ring is dR. The magnitude of the specific angular momentum of particles in a ring is given by:

$$l = R^2 \Omega(R) \tag{1.52}$$

We will inspect what happens when due to some turbulent flow two particles of adjacent rings switch positions. Particle going from:

R to $R + dR$: brings $l = (R + dR)R\Omega(R)$

$R + dR$ to R: brings $l = R(R + dR)\Omega(R + dR)$

The change of specific angular momentum at R is equal to:

$$\Delta l = R(R + dR)(\Omega(R + dR) - \Omega(R)) \tag{1.53}$$

Now we will approximate the effect of such switches happening all around the rings and we assume that the switches happen at some turbulent velocity v_t. The torque G (change of angular momentum per unit time) for the ring at $R + dR$ caused by an outer ring is [Pringle, 1981]:

$$G(R) \approx M_{\text{ring}} v_t \Delta l = 2\pi R H \rho v_t R(R + dR)(\Omega(R + dR) - \Omega(R)) \tag{1.54}$$

M_{ring} denotes the mass of the whole ring, H denotes the vertical extent of the disc at R and ρ is volume density at R. We further define $\Sigma = H\rho$ where Σ is vertically integrated density and we introduce kinematic viscosity as $\nu \equiv v_t dR$, for the sake of the argument we note it has the correct dimension. We get:

$$2\pi R^2 \Sigma \nu (R + dR) \frac{(\Omega(R + dR) - \Omega(R))}{dR} \xrightarrow{dR \to 0} 2\pi R^3 \Sigma \nu \frac{\Omega(R)}{dR} \approx G(R) \tag{1.55}$$

we see that dimension-wise we have the circumference of the disc $2\pi R$, then a 2D version of density Σ and $R^2 \frac{d\Omega}{dR} \propto \frac{\Delta l}{R}$, so ν has intuitively the meaning of the rate of angular momentum exchange, which is what we expect viscosity to be from our earlier considerations, hence the introduced definition seems correct. The net effect on a studied ring from an outer and inner neighbour will be in the limit $\xrightarrow{dR \to 0}$ equal to [Pringle, 1981]:

$$G_{\text{NET}} = \frac{\partial G}{\partial R} \tag{1.56}$$

The local power of viscous forces $\dot{E}_{dR}$ is then equal to;

$$\dot{E}_{dR} = G_{\text{NET}} \cdot \Omega(R) \tag{1.57}$$

The net power of viscous forces across the disc is obtained by per partes integration from the inner boundary R_{innb} to the outer boundary R_{outnb}, yielding;

$$\dot{E}_{\text{NET}} = \Delta E_{\text{outnb}} - \Delta E_{\text{innb}} - \int_{\text{Disk}} D_{\text{ring}}(R) dR \tag{1.58}$$

ΔE_{outnb} and ΔE_{innb} denote the flow of energy through the boundaries and $D_{\text{ring}}(R)$ denotes energy dissipation in a single ring. Local energy dissipation per unit area $D(R)$ is then derived [Pringle, 1981] using from 1.55 ;

$$D(R) = \frac{1}{2} \frac{1}{2\pi R} G(R) \frac{\partial \Omega}{\partial R} = \frac{1}{2} \nu \Sigma (R \frac{d\Omega(R)}{dR})^2 \tag{1.59}$$

Naturally, since kinematic viscosity controls the process that frees gravitational potential energy, energy dissipation is proportional to it. Lastly, an equation for the evolution of Σ can be derived from standard hydrodynamics after vertical integration Pringle [1981]:

$$\frac{\partial \Sigma}{\partial t} = -\frac{3}{R} \frac{\partial}{\partial R} [R^{\frac{1}{2}} \frac{\partial}{\partial R} (\nu \Sigma R^{\frac{1}{2}})] \tag{1.60}$$

An equation with a first temporal derivative on the left-hand side and a second spatial derivative on the right-hand side is of the heat transfer type:

$$\dot{f} = \Delta f \tag{1.61}$$

and we see that the kinematic viscosity plays the role of a controlling parameter, for example, if we consider a viscosity constant with R ($\nu \neq \nu(R)$) we can take it out of the derivative and for specific Σ-profile it will be the rate of temporal evolution. For a limit case of $\nu = 0$ there will be no temporal evolution and the Σ-profile will remain constant. As a model situation, we can imagine a viscous fluid initially organised in a single ring around the central object, in analogy with heat transfer this equation would push the matter smoothly spreading to smaller and larger radii.

1.2.4.3 Steady-state Keplerian disc

If we adopt the following assumptions [Pringle, 1981]:

- **Assumption 6** (Steady state)**.** *The disc is in a steady state, that is for all quantities q:*

  $$\frac{\partial q}{\partial t} = 0; \tag{1.62}$$

- **Assumption 7** (Keplerian flow)**.** *Matter flows around the central object with a Keplerian angular velocity:*

  $$\Omega = \Omega_K = \sqrt{\frac{GM_\star}{R^3}}, \tag{1.63}$$

then we can derive from eq. 1.60 a steady-equation for the surface density:

$$\Sigma = \frac{\dot{M}}{3\pi\nu}\left(1 - \sqrt{\frac{R_\star}{R}}\right), \tag{1.64}$$

and then by plugging into eq. 1.59:

$$D(R) = \frac{3GM\dot{M}}{8\pi R^3}\left(1 - \sqrt{\frac{R_\star}{R}}\right) \tag{1.65}$$

we obtain the energy dissipation rate.

1.2.4.4 α-parametrisation

The microphysics of viscosity remain an unsolved problem and an exact calculation of ν from first principles is difficult, if not impossible. We will introduce a parametrised description of the viscosity, independent of detailed microphysics [Shakura and Sunyaev, 1973].

Assumption 8 (Stress Tensor)**.** *We take into account specific components of the viscous stress tensor:*

$$\boldsymbol{\pi} = \begin{pmatrix} \pi_{rr} & \pi_{r\phi} & \pi_{rz} \\ \pi_{\phi r} & \pi_{\phi\phi} & \pi_{\phi z} \\ \pi_{zr} & \pi_{z\phi} & \pi_{zz} \end{pmatrix}, \tag{1.66}$$

namely $\pi_{r\phi}$, where r represents the radial component and ϕ the azimuthal component of a cylindrical coordinate system. That is we neglect all other components of the tensor.

Assumption 9 (Ideal gas)**.** *We assume that the disc is made up of ideal gas and adopt the equation of state in the form;*

$$P = \rho\frac{k_B T}{\mu m_u}, \tag{1.67}$$

where P denotes the pressure, ρ the volumetric density, k_B the Boltzmann constant, T the temperature, μ the mean molecular weight and m_u the atomic mass unit.

Keeping in mind the earlier considerations we will try to find a proportionality of the assumed viscous stress tensor for the cases of hydrodynamical and magnetic turbulence.

1. **Hydrodynamical turbulence.** Earlier we defined the kinematic viscosity as :

$$\nu = v_t dR. \tag{1.68}$$

We can interpret v_t as a typical velocity of eddies and dR as their maximum size. Let us now use a simple model approximating the vertical extent of the disc.

Assumption 10 (Vertical hydrostatic equilibrium)**.** *We assume that the disc is in a hydrostatic equilibrium along the z direction of cylindrical coordinates. We further assume that the disc has an isothermal vertical profile.*

If in the vertical direction, the disc is in hydrostatic equilibrium and the mass of the disc is negligible compared to $M_\star$, we can write (z being the vertical coordinate of the disc):

$$\frac{1}{\rho}\frac{\partial P}{\partial z} = -\frac{\partial}{\partial z}\left[\frac{GM_\star}{(r^2+z^2)^{\frac{1}{2}}}\right]. \tag{1.69}$$

For a thin disc, which we assumed, we can approximate the right-hand side with a homogeneous gravitational field in the vertical direction:

$$\frac{1}{\rho}\frac{\partial P}{\partial z} \approx -\frac{GM_\star z}{r^3} \tag{1.70}$$

We evaluate the left-hand side at $z = H$ and consider the following proportionalities:

- $$\frac{\partial P}{\partial z} \propto \frac{P}{H} \tag{1.71}$$
- by definition (for an isothermal ideal gas):

  $$\frac{P}{\rho} \propto c_s^2, \tag{1.72}$$

  where c_s denotes the sound speed in the gas.
- and again by definition of the Keplerian velocity $v_k = \Omega_k R$:

  $$v_k^2 = \frac{GM}{R}. \tag{1.73}$$

Altogether, we get:

$$\frac{H}{R} \propto \frac{c_s}{v_k} \tag{1.74}$$

Upto this point, we haven't defined H, but we will use this proportionality for an a posteriori definition [Pringle, 1981]:

Definition 3 (Pressure scale-height/Disc semi-thickness)**.** *We define the disc semi-thickness as:*

$$H \overset{def.}{\equiv} \frac{c_s}{v_k} R \tag{1.75}$$

We now add a further assumption:

Assumption 11 (Maximum size of eddies)**.** *We assume that the largest eddies will be the size of the pressure scale height H.*

Hence under the accepted assumptions, we can state the following proportionality for the viscous stress tensor [Shakura and Sunyaev, 1973]:

$$\pi_{(r\phi)_{\text{visc}}} = \rho\nu r \frac{d\Omega(r)}{dr} \propto -\rho v_t H \frac{v_k}{R} \propto -\rho c_s^2 \frac{v_t}{c_s}, \tag{1.76}$$

where we implicitly assumed the Keplerian angular velocities 7.

2. **Turbulence generated by chaotic magnetic fields.** Let us consider the energy of the gas (or plasma) [Shakura and Sunyaev, 1973];

   - The energy density of a magnetic field $\boldsymbol{h}$ is equal to:

   $$\mathcal{E}_{\text{mag}} = \frac{|\boldsymbol{h}|^2}{8\pi} \tag{1.77}$$

   from now on we denote $|\boldsymbol{h}| = h$.

   - Thermal energy density (kinetic energy of random particle motions) can be calculated as;

   $$\mathcal{E}_{\text{th}} = \frac{\rho c_s^2}{2} \tag{1.78}$$

   We can derive a proportionality for the magnetic stress tensor as:

   $$\pi_{(r\phi)_{\text{mag}}} = \left| \frac{\boldsymbol{h_r} \times \boldsymbol{h_\phi}}{8\pi} \right| \propto -\frac{h^2}{8\pi} \propto -\frac{h^2}{4\pi\rho c_s^2}\rho c_s^2 \tag{1.79}$$

The complete stress tensor will be given by a superposition of the two Shakura and Sunyaev [1973]:

$$\begin{aligned} \pi_{(r\phi)} &= \pi_{(r\phi)_{\text{visc}}} + \pi_{(r\phi)_{\text{mag}}} \\ &\propto -\rho c_s^2 \frac{v_t}{c_s} - \frac{h^2}{4\pi\rho c_s^2}\rho c_s^2 \propto -\left(\frac{v_t}{c_s} + \frac{h^2}{4\pi\rho c_s^2}\right)\rho c_s^2 \\ &\propto -\alpha\rho c_s^2 \end{aligned} \tag{1.80}$$

we have introduced an α parametrization of the total stress tensor first suggested by [Shakura and Sunyaev, 1973]:

$$\alpha = \left(\frac{v_t}{c_s} + \frac{h^2}{4\pi\rho c_s^2}\right). \tag{1.81}$$

If we apply the definition of sound speed we see that this result can be rewritten as:

$$\pi_{(r\phi)} \propto -\alpha P \tag{1.82}$$

hence we expect higher pressure to lead to greater viscous stress. The advantage of this approach is that we can study the large-scale evolution of the disc without being dependent on the specific microscopic configuration. Yet models of the microphysics of viscosity can look for correlations with the α parameter. For example, 3D simulations conducted by [Arlt and Rüdiger, 2001] show that when magnetic fields are introduced α increases rapidly. What can say about α [Shakura and Sunyaev, 1973]?

1. ($\frac{v_t}{c_s} < 1$) is to be expected. If turbulence were to turn supersonic, it would lead to rapid heating of the disc which would increase the velocity of random motions, that is the sound speed would increase. This would make the turbulent velocity subsonic again.

2. As we expect the magnetic fields to remain chaotic and no structure organised by the magnetic fields to arise it is natural to assume that the energy of the magnetic field will be lower than thermal energy:

$$\frac{\rho c_s^2}{2} > \frac{h^2}{8\pi} \implies \frac{h^2}{4\pi\rho c_s^2} < 1 \tag{1.83}$$

Hence $\alpha < 1$ is to be expected if one source of viscosity dominates over the other.

We could have arrived at this parametrisation just by straightforwardly applying our assumptions. If the eddy responsible for angular momentum exchanger between annuli in 1.55 is to be subsonic and equal to or smaller than H in size we can simply write from 1.68:

$$\nu = \alpha c_s H \qquad \text{with} \qquad \alpha < 1 \tag{1.84}$$

This is a parametrised version of our original definition of kinematic viscosity 1.68 [Pringle, 1981]. There is no trustworthy way to constrain the size of α further for all disc cases in general, hence the search within the range $\langle 0; 1\rangle$ must be left to observations and simulations.

In principle, α can be and is expected to be dependent on r. One way of approaching this was introduced by ([Flock et al., 2016]). We plug the α prescription for kinematic viscositz into 1.64;

$$\Sigma = \frac{\dot{M}}{3\pi\alpha(R)Hc_s}\left(1 - \sqrt{\frac{R_\star}{r}}\right) \tag{1.85}$$

we see that for a given accretion rate $\dot{M}$ kinematic viscosity will determine the Σ-profile of the disc. If we expect there will be regions with a lot of large-scale turbulence (α high) we will get a lower density and regions with little turbulence (α low) will be high-density regions. For a given midplane temperature profile of a disc $T = T(R)$, the magnetorotational instability will occur in regions where the gas is sufficiently ionised, which we equate to regions where the temperature will be higher than some T_{MRI}. We expect these regions to be highly turbulent and hence have high kinematic viscosity, which is parametrised by α_{MRI}. Regions of $T < T_{\mathrm{MRI}}$ will have mostly laminar flow, hence low kinematic viscosity, which is parametrised by α_{DEAD}. [Flock et al., 2016] proposed a formula to ensure a smooth transition between the regions:

$$\alpha = (\alpha_{\mathrm{MRI}} - \alpha_{\mathrm{DEAD}})\left[\frac{1 - \tanh(\frac{T_{\mathrm{MRI}} - T}{\Delta T})}{2}\right] + \alpha_{\mathrm{DEAD}} \tag{1.86}$$

The input parameters of this dependence are: T_{MRI}, $\Delta T, \alpha_{\mathrm{MRI}}$ and α_{DEAD}. [Flock et al., 2016] that varying ΔT from 10K to 50K did not modify the conclusions of their model. The effects of varying T_{MRI} and α_{DEAD} we reported as modest. α_{MRI} plays the role of the main controlling parameter α and the largest overall effect on viscous forces, hence varying it has a significant influence on the disc structure.

We have also stated that α should in principle depend on R but here we note that in applications an α constant with R is often used. For hot circumstellar matter (like around the β Lyr A system) 1.86 reduces to $\alpha =$ const. because the whole disc is fully ionised.

1.2.5 Timescales

In this section, we discuss different characteristic timescales of a steady-state Keplerian disc. We will also show that our derivations so far are consistent with assumption 2.

1.2.5.1 Dynamical timescale

We can approach the dynamical scale from two sides. First, we can think about a timescale that arises from the disc's rotation around the central object:

Timescale 1 (Dynamical timescale from rotation). *For a disc rotating around a gravitating centre with a rotational velocity of Ω we introduce the typical timescale at a certain radius from the central object for dynamical processes as equal to the rotational period at that radius, that is:*

$$t_{\mathrm{dyn}} = \frac{1}{\Omega} \tag{1.87}$$

On the other hand, dynamical processes govern the emergence of hydrostatic equilibrium in the direction perpendicular to the disc's plane [Czerny, 2019]. Let us derive an expression for this vertical timescale t_z. Consider the z component (cylindrical coordinates) of the hydrodynamic equation of motion for a time-dependent disc. Here we assume that terms in the equation must be comparable and compare the pressure gradient to the acceleration in the z direction. This intuitively makes sense, a falling particle will be met by the pressure gradient and since we assume that the disc tends towards hydrostatic equilibrium in the vertical direction, the pressure gradient must end up equal to the gravity. We then take averages over the z direction of both sides of the equation:

$$\rho\frac{\partial v_z}{\partial t} \approx -\frac{\partial P}{\partial z} \quad \rightarrow \quad \bar{\rho}\frac{\bar{v_z}}{t_z} \approx \frac{P}{H} \tag{1.88}$$

The average velocity in the z direction will by definition be equal to $\bar{v_z} = H/t_z$ and a fraction of pressure and density gives us sound speed, we get:

$$\frac{H^2}{t_z^2} = \bar{c_s}^2 \tag{1.89}$$

Hence the timescale for the emergence of hydrostatic equilibrium in the z direction is equal to the approximate time it would take for a sound wave to travel through the disc parallel to the z axis [Czerny, 2019]:

Timescale 2 (Dynamical timescale from a vertical hydrostatic equilibrium)**.** *For a disc where a vertical hydrostatic equilibrium emerges, we can calculate the typical timescale for this dynamical process as:*

$$t_z = \frac{H}{\bar{c_s}} \tag{1.90}$$

From the definition of the pressure scale height H (eq. 3) we see that the two approaches to the dynamical timescale are equal. This is obvious if we imagine one particle orbiting the central object, for it to go through the mid-plane it will take a maximum of one orbit.

$$t_{\mathrm{dyn}} = t_z \tag{1.91}$$

1.2.5.2 Sound speed timescale

Timescale 3 (Sound speed timescale)**.** *We define the characteristic sound speed timescale at a radius R as the time it would take for an acoustic wave to reach that radius from the central object if it kept the sound speed c_s calcualted at that radius the whole time.*

$$t_{c_s} = \frac{R}{c_s} \tag{1.92}$$

From the definition of the pressure scale height (eq. 3) we obtain;

$$t_{c_s} = \frac{R}{H}\frac{1}{\Omega_K} \tag{1.93}$$

Applying the thin disc approximation 4 we know that $\frac{R}{H} \gg 1$.

1.2.5.3 Thermal timescale

For thermal physical mechanisms, the time it takes for a vertical thermal balance to emerge can be considered a characteristic timescale of the disc. We look for a timescale that is a measure of how quickly energy redistributes itself in the disc. A straightforward model, following a similar intuition as one would for the Kevin-Helmholtz timescale for stars, will give us a good approximation [Czerny, 2019].

Timescale 4 (Thermal timescale)**.** *Let us consider a unit area of the disc at a certain radius from the central object (assuming polar symmetry), the unit area will have a thermal energy content of* E_{th} *and a radiative flux of* F_{rad}*. We define the thermal timescale of a disc at a certain radius as the time it takes for all of a unit area thermal energy content to be radiated away, that is:*

$$t_{th} = \frac{E_{th}}{F_{rad}} \tag{1.94}$$

Let us now investigate the numerator and denominator under all the aforementioned assumptions. In the hydrodynamical energy equation we further assume that:

- the advection term is negligible, that is $v \cdot \nabla \epsilon = 0$.
- conduction is negligible, that means for the conduction term $\nabla q = 0$
- we add a radiation term to the energy equation but assume that energy is radiated away only through the face of the disc, that means $(\nabla F_{\text{rad}})_R = (\nabla F_{\text{rad}})_\phi = \ 0$

Under the ideal gas assumption we get the thermal energy content:

$$E_{\text{th}} \propto T \propto PV \propto P(H \cdot 1) \propto PH \tag{1.95}$$

We will now derive a specific proportionality for F_{rad}. Under the given assumptions the energy conservation equation simplifies to:

$$0 = -\frac{dF_{\text{rad}}}{dz} - \pi_{R\phi} R \frac{d\Omega_K}{dR} \tag{1.96}$$

We can calculate the radial differential of angular frequency for a Keplerian disc, which after being multiplied by r gives $\frac{3}{2}\Omega_K$ and plug in the α prescription for viscosity:

$$\frac{dF_{\text{rad}}}{dz} = \frac{3}{2}\alpha P \Omega_K \tag{1.97}$$

Avreaging in the z-direction leads to an expression for F_{rad}:

$$F_{rad} = \frac{3}{2}\alpha P \Omega_K H \tag{1.98}$$

Under these assumptions we get the thermal timescale [Czerny, 2019]:

$$t_{th} = \frac{E_{th}}{F_{rad}} \propto \frac{PH}{\alpha P \Omega_K H} = \frac{1}{\alpha \Omega_K} \tag{1.99}$$

This conclusion will be useful later in comparing the different timescales.

1.2.5.4 Viscous timescale

Viscosity is a measure of how fast viscous processes can redistribute angular momentum in a system. Viscous processes will hence govern large-scale mass redistribution in the disc such as accretion. A characteristic timescale for these processes is the time it takes for angular momentum to be diffused over a characteristic length scale of the system. By taking 1.64 and plugging in for $\dot{M}$, we can see;

$$v_R \propto \frac{\nu}{R} \tag{1.100}$$

Hence we define;

Timescale 5 (Viscous timescale)**.** *For kinematic viscosity* ν *at radius* R *the viscous time scale is defined as the time it takes to diffuse angular momentum in the disc up to this radius, this timescale is given by:*

$$t_\nu = \frac{R^2}{\nu} \tag{1.101}$$

As in the case of the thermal timescale, we will find an expression for this timescale 1.101 under all the aforementioned assumptions. If we plug in the α parametrisation for kinematic viscosity and use the definition fro pressure scale height 3, we get [Czerny, 2019]:

$$t_\nu = \frac{1}{\alpha}\frac{R^2}{H}\frac{1}{c_s} = \frac{1}{\alpha}\left(\frac{R}{H}\right)^2\frac{1}{\Omega_K} \tag{1.102}$$

Applying the thin disc approximation 4 we know that $\frac{R}{H} \gg 1$. This expression will be helpful to us to relate this timescale to the other timescales.

1.2.5.5 Comaprison of the timescales

We have obtained expressions that are straightforward to compare for all four timescales.

$$t_{dyn} = \frac{1}{\Omega_K} \qquad t_{c_s} = \left(\frac{R}{H}\right)\frac{1}{\Omega_K} \qquad t_{th} = \frac{1}{\alpha}\frac{1}{\Omega_K} \qquad t_\nu = \frac{1}{\alpha}\left(\frac{R}{H}\right)^2\frac{1}{\Omega_K}$$

If we remind ourselves that:

1. by definition $\alpha \leq 1$.
2. the disc is thin then $\frac{R}{H} \gg 1$.

We can conclude, that the following two hierarchies hold [Pringle, 1981]:

1. $$t_{dyn} \leq t_{th} \ll t_\nu \tag{1.103}$$
2. $$t_{dyn} < t_{c_s} \ll t_\nu \tag{1.104}$$

The first hierarchy shows that the derivations we have conducted to this point are consistent with our assumption about timescales at the beginning of our discussion of thin accretion discs 2. Another way of looking at the emergence of these three timescales is in the context of mechanisms behind different instabilities. [Shakura and Sunyaev, 1976] found that the viscous and thermal instabilities develop as a bifurcation of unstable modes, hence further underlining the separation. The obtained hierarchy has a few practical implications for studying discs:

- since $t_{dyn} \ll t_\nu$ we assume that a vertical hydrostatic equilibrium has already established itself.
- since $t_{th} \ll t_\nu$ we also assume that vertical thermal equilibrium has established itself.

1.3 The Fargo model

We will now turn to the specific physics taken into account in the numerical model applied in this thesis. The code FARGO_THORIN [Chrenko et al., 2017] was built to simulate the interactions of three entities under the influence of a dominant central gravitating object: two fluids (a gas disc and a pebble disc) and planetary embryos. The primary motivation was the study of protoplanetary discs. A full overview of the accounted-for physics in the model is described by the authors of the code in [Chrenko et al., 2017]. The aim here is to simulate a circumstellar gaseous disc in a binary system, hence many aspects of the full model were not used. We study the interactions of a gaseous disc in the gravitational field of the central star.

1.3.1 The set of 2D RHD equations

In the first section, we derived a general form of fluid equations, here we will introduce a specific case of fluid equations that are implemented in the code. We do not state the full set available in the code [Chrenko et al., 2017] because as was described above not all terms we relevant to the problem.

- The hydrodynamical model works with 2D arrays, that is we work with vertically integrated quantities. We define a cylindrical coordinate system where R represents the radial component, ϕ represents the azimuthal angle and z is the vertical coordinate perpendicular to the disc's plane. We set the origin in the centre of the central star and let the unit vector $\boldsymbol{e}_z$ be parallel with the integrated angular momentum vector of the whole disc. A vertically integrated value X_{2D} is formally always derived from its 3D counterpart X_{3D} as:

$$X_{2D} = \int_{-\infty}^{+\infty} X_{3D} dz \tag{1.105}$$

where H is the disc's semi-thickness as defined earlier 3.

t is time.

Σ is vertically integrated mass density ρ.

$\boldsymbol{v}$ is a gas element's verically integrated velocity. It is a 2D vector: $\boldsymbol{v} = (v_r, v_\phi)$.

P is the vertically integrated pressure.

$\boldsymbol{\pi}$ is the viscous stress tensor.

Φ is the gravitational potential.

ϵ is the vertically integrated internal energy of the gas.

Q_{visc} represents viscous heating.

Q_{irr} represents stellar irradiation.

Q_{rad} represents radiative diffusion.

T is the midplane temperature of the gas.

The exact meaning of each term will be specified in subsequent sections. In this notation, the set of implemented fluid equations is as follows [Chrenko et al., 2017].

$$\frac{\partial \Sigma}{\partial t} + \nabla \cdot (\Sigma v) = 0 \tag{1.106}$$

$$\frac{\partial \boldsymbol{v}}{\partial t} + \boldsymbol{v} \cdot \nabla \boldsymbol{v} = -\frac{1}{\Sigma}\nabla P + \frac{1}{\Sigma}\nabla \cdot \boldsymbol{\pi} - \frac{\int \rho \nabla \Phi \mathrm{d}z}{\Sigma} \tag{1.107}$$

$$\frac{\partial \epsilon}{\partial t} + \nabla \cdot (\epsilon \boldsymbol{v}) = -P\nabla \cdot \boldsymbol{v} + Q_{\text{visc}} + Q_{\text{irr}} - Q_{\text{rad}} \tag{1.108}$$

To close the set an ideal gas equation of state is implemented:

$$P = \Sigma \frac{\mathcal{R}T}{\mu} = (\gamma - 1)\epsilon \tag{1.109}$$

where the three constants are $\mathcal{R}$ the universal gas constant, μ mean molecular weight and γ is the adiabatic index.

1.3.2 Vertical profile of the gas

Although the calculation is done in 2D the equation of motion still contains an integral over 3D mass density ρ in the gravitational force term. This is approached by assuming a simple gaussian formula for the density profile in the vertical direction, that is [Chrenko et al., 2017]:

$$\rho(r, \phi, z) = \frac{\Sigma}{\sqrt{2\pi}H} \exp\left(-\frac{z^2}{2H^2}\right) \tag{1.110}$$

we see that the quantitative value of the volume density ρ is implied by quantities determined by the fluid equations. H is defined the same as in 3.

1.3.3 Gravitational potential of the disk

The [Chrenko et al., 2017] model approximates the gravitational potential between a particle and the fluid using a formula by [Klahr and Kley, 2006];

$$\phi_{\text{em}} = \begin{cases} -\frac{GM_{\text{em}}}{d}, & (d > r_{\text{sm}}) \\ -\frac{GM_{\text{em}}}{d}\left[\left(\frac{d}{r_{\text{sm}}}\right)^4 - 2\left(\frac{d}{r_{\text{sm}}}\right)^3 + 2\frac{d}{r_{\text{sm}}}\right], & (d \leq r_{\text{sm}}) \end{cases} \tag{1.111}$$

M_{em} denotes the mass of the embryo, d is the 3D distance to the gas cell a r_{sm} is the smoothing lenght. Smoothing lengths are used to avoid values diverging when $d \to 0$ in the case of discretized equations. Here we always choose $r_{\text{sm}} = 0.5R_{\text{H}}$, R_{H} being the Hill's sphere. This formula is for a 3D case, to compute the gravitational acceleration of the 2D gas cells, specific force density f projected onto the midplane obtained [Chrenko et al., 2017];

$$f_{\text{em}}(s) = -\int \rho \frac{\partial \phi_{\text{sec}}}{\partial s}\,\mathrm{d}z \tag{1.112}$$

Due to the set vertical profile for ρ (section 1.3.2) the model neglects the influence of the embryo on the vertical profile of the disc [Chrenko et al., 2017]. We note that same as in 5, the model assumes that the mass of the disc is negligible compared to the central star, that is the disc has no self-gravity.

1.3.4 Viscous stress tensor

The viscous stress tensor is calculated according to [Masset, 2002];

$$\begin{aligned} \pi_{rr} &= 2\eta D_{rr} - \frac{2}{3}\eta \nabla \cdot \boldsymbol{v} \\ \pi_{\phi\phi} &= 2\eta D_{\phi\phi} - \frac{2}{3}\eta \nabla \cdot \boldsymbol{v} \\ \pi_{r\phi} &= \tau_{\phi r} = 2\eta D_{r\phi} \end{aligned} \tag{1.113}$$

where;

$$\begin{aligned} D_{rr} &= \frac{\partial v_r}{\partial r} \\ D_{\phi\phi} &= \frac{1}{r}\frac{\partial v_\phi}{\partial \phi} + \frac{v_r}{r} \\ D_{r\phi} &= \frac{1}{2}\left[r\frac{\partial}{\partial r}\left(\frac{v_\phi}{r}\right) + \frac{1}{r}\frac{\partial v_r}{\partial \phi}\right] \end{aligned} \tag{1.114}$$

η denotes the vertically integrated dynamical viscosity.

$$\eta = \Sigma\nu \tag{1.115}$$

ν is as before kinematic viscosity. The code offers three modes for kinematic viscosity;

1. Kinematic viscosity is a constant

$$\nu = \mathrm{const} \tag{1.116}$$

2. The [Shakura and Sunyaev, 1973] α- prescription for kinematic viscosity as described in section 1.2.4.4.

$$\nu = \alpha H c_s \tag{1.117}$$

   c_s denotes the sound speed and H is the pressure scale height. $\alpha = \mathrm{const}$ is chosen at the input.

3. The α prescription for viscosity with $\alpha = \alpha(R)$ according to [Flock et al., 2016] as was discussed in equation 1.86.

In this thesis, the second option was always used. The third option didn't add anything to the model, since the whole disc is hot enough to be fully ionised. That means equation 1.86 reduced to $\alpha = \alpha_{\mathrm{MRI}}$ everywhere.

1.3.5 Energy balance

Let us discuss the terms of the energy equation [Chrenko et al., 2017].

1.3.5.1 Viscous heating

Viscous energy dissipation in the disc is computed as [Chrenko et al., 2017];

$$Q_{\mathrm{visc}} = \frac{1}{2v\Sigma}\left(\pi_{rr}^2 + 2\pi_{r\theta}^2 + \pi_{\theta\theta}^2\right) + \frac{2v\Sigma}{9}(\nabla \cdot \boldsymbol{v})^2 \tag{1.118}$$

1.3.5.2 Radiative diffusion

The FARGO_THORIN model assumes that energy radiates away only through the face of the disc [Chrenko et al., 2017]. Then the 3D radiative flux $\boldsymbol{F}_{\mathrm{3D}}$ of a gas cell can be approximated as;

$$Q_{\mathrm{rad}} = \int_{-\infty}^{\infty} \nabla_{\mathrm{3D}} \cdot \boldsymbol{F}_{\mathrm{3D}} \mathrm{d}z \simeq \int_{-\infty}^{+\infty} \frac{\partial F_z}{\partial z}\,\mathrm{d}z + 2H\nabla \cdot \boldsymbol{F} \equiv Q_{\mathrm{vert}} + 2H\nabla \cdot \boldsymbol{F}. \tag{1.119}$$

The Stefan-Boltzman law is used to calculate the energy radiated away at H;

$$Q_{\mathrm{vert}} \simeq \frac{2\sigma_{\mathrm{R}} T^4}{\tau_{\mathrm{eff}}}, \tag{1.120}$$

σ_B denotes the Stefan-Boltzmann constant. Effective optical depth τ_{eff} is incorporated to model the effects on the energy when travelling through the disc's vertical profile. τ_{eff} is calculated according to accretion disc atmospheres by [Hubený, 1990].

$$\tau_{\mathrm{eff}} = \frac{3}{8}\tau_{\mathrm{opt}} + \frac{1}{2} + \frac{1}{4\tau_{\mathrm{opt}}}, \tag{1.121}$$

Where the optical depth τ_{opt} is measured from the mid-plane up and approximated by [Chrenko et al., 2017];

$$\tau_{\mathrm{opt}} \simeq C_k \frac{\kappa\Sigma}{2}, \tag{1.122}$$

κ denotes opacity, C_k is a correction factor for the drop in opacity above the midplane. $C_k = 0.6$ is chosen approximate results from 3D modeling [Chrenko et al., 2017].

For the second radial flux part of equation 1.119 the flux-limited diffusion approximation is used as derived by [Levermore and Pomraning, 1981];

$$\boldsymbol{F} = -\lambda_{\lim} \frac{16\sigma_{\mathrm{R}}}{\rho_0 \kappa} T^3 \nabla T \tag{1.123}$$

ρ_0 denotes the midplane volume density, T the midplane temperature and $\lambda_{\mathrm{lim}}$is the so-called flux limiter [Chrenko et al., 2017]. The flux limiter is introduced to prevent large scale gradients which wouldn't be consistent with the assumptions of the approximation [Levermore and Pomraning, 1981]. The flux limiter is calculated according to [Kley, 1989].

The so-called one-temperature approach is utilised [Chrenko et al., 2017]; it is assumed that the radiation is thermalized to the same temperature as the gas [Kley et al., 2009].

1.3.5.3 Stellar irradiation

Heating from the central star is assumed to only through the disc's faces. And is treated in analogy with vertical radiative loses Q_{vert} (equation 1.120);

$$Q_{\mathrm{irr}} = \frac{2\sigma_{\mathrm{R}} T_{\mathrm{irr}}^4}{\tau_{\mathrm{eff}}} \tag{1.124}$$

T_{irr} denotes the effective temperature of the radiation falling onto the disc's surface at r. It is calculated by the projection of the radiative flux from the central star on the surface [Chrenko et al., 2017];

$$T_{\mathrm{irr}}^4 = (1-A)\left(\frac{R_\star}{r}\right)^2 T_\star^4 \sin\delta. \tag{1.125}$$

A denotes the disc's albedo and the angle δ is yielded by [Chrenko et al., 2017];

$$\delta = \arctan\left(\frac{\mathrm{d}H}{\mathrm{d}r}\right) - \arctan\left(\frac{H-0.4R_\star}{r}\right). \tag{1.126}$$

1.3.6 Initial conditions

Vertically integrated internal ϵ and vertically integrated density Σ
The initialization of the internal energy of the gas ϵ and the vertically integrated density Σ is conducted through an iterative routine applying an energy balance between viscous heating and vertical radiative losses and stellar irradiation. The terms of this energy balance are not calculated in their full form (as they were described in the preceding sections) but rather the simplified expressions of a steady state disc, as they were described in section 1.2 are applied.

$$Q'_{\mathrm{visc}} + Q'_{\mathrm{irr}} = Q'_{\mathrm{vert}} \tag{1.127}$$

Q'_{visc} is used in the form of equation 1.59 with ν, Σ plugged in from equation 1.64. Q'_{irr} is calculated as in equation 1.124 with $\tau_{\mathrm{eff}} = 1$ assumed and an approximation for the $\sin\delta$ term.

$$\sin\delta \simeq \frac{0.4R_\star + \frac{2}{7}H}{r} \tag{1.128}$$

Q'_{vert} is the same as in equation 1.120. The initial value for Σ at each radius is obtained as:

$$\Sigma = \frac{\dot{M}}{3\pi\nu} \tag{1.129}$$

which is an approximation of the equation 1.64. The whole iterative algorithm which is applied at each r can be summarized as:

1. An estimate of temperature T_0 from energy is obtained from the equation of state 1.109.

2. T_0 is used to calculate an estimate of sound speed and pressure scale height. From sound speed, an estimate of viscosity is calculated through equation 1.117.

3. The estimate of viscosity is plugged into equation 1.129 to obtain an estimate of Σ.

4. The $T0$ estimate of temperature, The Σ estimate and the estimate of viscosity are plugged into the energy balance 1.127 to obtain a second estimate of temperature T_1.
5. T_0 and T_1 are compared and if the difference is larger than tolerated a new temperature T_0 is taken randomly from the interval (T_0, T_1). Another iteration starts from the second step.

Finally: When the difference of T_0 and T_1 is sufficiently small, the routine is stopped and the internal energy of the gas is calculated from the average of the two temperatures again using equation 1.109 and the last Σ estimate.

To find the first estimate of T_0 the user must input initial profiles of Σ and H in the form of power laws.

Radial and azimuthal velocity of the gas v_r, v_ϕ

- The initial radial velocity profile is taken from the theory of steady-state Keplerian discs (described in section 1.2):

$$v_r = -\frac{3}{2}\frac{\nu}{r} \tag{1.130}$$

- The initial azimuthal velocity of gas cells is obtained according to Masset [2002];

$$v_\phi = \frac{GM_\star}{r}\left(1 - \frac{H}{r}\right) \tag{1.131}$$

  that is slightly sub-Keplerian in order to account for the radial pressure gradient.

We note that initial conditions as they are described here were not yet implemented in the code described in [Chrenko et al., 2017].

1.3.7 Boundary conditions

Outer Boundary

Boundary conditions in the model are enforced for a "ghost" ring of gas cells that lies beyond the outermost ring, this ring can be thought of as a reservoir of matter to be fed into the disc. First, the arithmetic average of the vertically integrated density Σ and the vertically integrated energy ϵ of two neighbouring is obtained. The two values for Σ and ϵ and the vertically integrated equation of state 1.109 are used to find a power law for temperature. Using this power law the temperature is extrapolated to the "ghost" ring (denoted T_g). For the temperature in the ghost ring sound speed is calculated and subsequently (using the prescription 1.117) viscosity ν_g is obtained. The imposed boundary condition then are:

- The vertically integrated density of the "ghost" ring is assumed to be:

$$\Sigma_\mathrm{g} = \frac{\dot{M}}{3\pi\nu_\mathrm{g}} \tag{1.132}$$

  which is an approximation of equation 1.64 from the theory of Keplerian steady-state discs.

- The vertically integrated internal energy is then obtained from the equation of state 1.109:

$$\epsilon_\mathrm{g} = \frac{\Sigma_\mathrm{g} T_\mathrm{g} \mathcal{R}}{\mu(\gamma - 1)} \tag{1.133}$$

- Radial velocity in the ghost ring is again taken from Keplerian steady-state disc theory:

$$v_{r\mathrm{g}} = \frac{3}{2}\frac{\nu_\mathrm{g}}{R} \tag{1.134}$$

- Azimuthal velocity $v_{\phi \mathrm{g}}$ in the "ghost ring" is assumed to be the same as in the outermost active ring.

Inner Boundary
The inner boundary conditions are treated in the same manner as the outer boundary conditions but for a "ghost" ring located beyond the innermost active ring. We note that boundary conditions as they are described here were not yet implemented in the code described in [Chrenko et al., 2017].

1.3.7.1 Damping zones

For gas cells close to the boundaries wave-damping zones are set up. For quantity q in the set-up zone the following damping is set up [Chrenko et al., 2017];

$$\textbf{??}\frac{dq}{dt} = -\frac{q - q_0}{t_{\mathrm{damp}}} p(r) \tag{1.135}$$

q_0 denotes the target value to which the hydrodynamic quantity is damped, t_{damp} is a characteristic time-scale on which the damping occurs and $p(r)$ is a dimensionless parabolic function which is 0 at beginning of the zone and 1 at the boundary [de Val-Borro et al., 2006]. The target values q_0 for each quantity are defined by the boundary conditions as described above.

2. Numerical methods

In this chapter, we summarize the basic algorithms and numerical methods applied in this thesis. The FARGO_THORIN hydrocode is built on the basis of the Fargo algorithm [Masset, 2000] and the van leer extrapolation method [Van Leer, 1977], both are described in this chapter.

2.1 Discretization, the finite difference method

The Differential equations in FARGO_THORIN [Chrenko et al., 2017] are solved numericaly, in their discretized form. The equations were discretized using the finite difference method. The finite difference method can be derived from Taylor's expansion. The functional value of a function $f(x)$ close to x_0 can be approximated to an arbitrary precision as:

$$f(x_0 + s) = f(x_0) + \frac{f'(x_0)}{1!}s + \frac{f''(x_0)}{2!}s^2 + ... + \frac{f^n(x_0)}{n!}s^n + O(s^{n+1}) \tag{2.1}$$

where s is small. Neglecting all terms of power s^2 or higher, we are left with;

$$f(x_0 + s) \approx f(x_0) + f'(x_0)s + O(s^2) \tag{2.2}$$

Solving for $f'(x_0)$ we arrive at:

$$f'(x_0) \approx \frac{f(x_0 + s) - f(x_0)}{s} + O(s) \tag{2.3}$$

We see that the error of this method is proportional to the step size s, which we found by dividing the whole equation by s. For numerical applications, differential operators are discretized on some kind of structure (mesh, grid). The step s is then the characteristic length between two points of the structure.

2.1.1 Staggered Polar Mesh

A natural structure to use discretized hydrodynamic quantities describing a circumstellar disc is a polar mesh. The polar mesh used in FARGO_THORIN is defined according to [Masset, 2000] as follows:

- In the radial direction, the mesh is evenly split into N_r rings.
- In the azimuthal direction, the mesh is evenly split into N_ϕ sectors, each having the angular width $\Delta\phi = \frac{2\pi}{N_\phi}$.
- The inner boundary is placed at the radius R_{innb} and the outer boundary is placed at R_{outnb}. The two mesh boundaries coincide with the beginning and end of the innermost and outermost rings of cells.
- Beyond each boundary, a ring of "ghost" cells is added, where boundary conditions are applied as described in section 1.3.7 [Stone and Norman, 1992]. Hydrodynamical equations are not solved in the ghost cells.
- Scalar quantities such as the vertically integrated density Σ or the internal energy ϵ are located in the center of these cells.
- Vector quantities such as components of the 2D gas velocity vector are placed at the interfaces between cells. The radial velocities v_r are placed at the interfaces between rings, centred in azimuth in the individual cells. The azimuthal velocities v_ϕ are placed at the interfaces between sectors, centered in radius in the individual cells.

In this chapter, i is always the radial index and j the azimuthal index.

2.2 Operator splitting and van Leer's second-order upwind interpolation

2.2.1 Operator splitting

The solver used by FARGO_THORIN uses a time-explicit Eulerian method. To improve accuracy each time step is split into substeps. If a differential operator connected to a quantity Q is considered such as:

$$\frac{\partial Q}{\partial t} = \mathcal{L}(Q) \tag{2.4}$$

It is assumed that it can be split into parts according to:

$$\mathcal{L}(Q) = \mathcal{L}_1(Q) + \mathcal{L}_2(Q) + \mathcal{L}_3(Q)... \tag{2.5}$$

A finite difference representation of each part of the operator is then denoted as:

$$\mathcal{L}_i \rightarrow L_i$$

Hence, an operator split procedure for the above-defined operator can be written as follows:

$$\frac{(Q^1 - Q^0)}{\Delta t} = L(Q^0) \tag{2.6}$$

$$\frac{(Q^2 - Q^1)}{\Delta t} = L(Q^1) \tag{2.7}$$

$$\frac{(Q^3 - Q^2)}{\Delta t} = L(Q^2)... \tag{2.8}$$

The top indices denote partially updated quantities [Stone and Norman, 1992]. Operator splitting is reported to be more accurate than a single-step integration. The time-step in FARGO_THORIN is split into [Masset, 2000, Stone and Norman, 1992]:

Source step: In three sub-steps, hydrodynamical quantities within cells are updated.

Transport step: Quantities are transported between cells due to fluid advection.

In the following subsections, we describe each step individually, including the numerical algorithms they are based on.

2.2.2 Source step

The source step solves the finite difference approximation of sink and source terms of the RHD equations, introduced in section 1.3.

$$\Sigma \frac{\partial \boldsymbol{v}}{\partial t} = -\nabla P + \nabla \cdot \boldsymbol{\pi} - \int_{-\infty}^{\infty} \rho \nabla \Phi \mathrm{d}z \tag{2.9}$$

$$\frac{\partial \epsilon}{\partial t} = -P \nabla \cdot \boldsymbol{v} + Q_{\mathrm{visc}} + Q_{\mathrm{irr}} - Q_{\mathrm{rad}} \tag{2.10}$$

The source step is divided into three sub-steps, let us discuss each sub-step separately [Stone and Norman, 1992]:

Sub-step 1.: Velocities are updated, to account for pressure gradients, gravitational acceleration and curvature terms arising from the polar coordinate system.

Sub-step 2.: The viscous stress tensor is updated using the velocities from the first sub-step. Subsequently, velocities are updated due to viscous stresses and an imposed artificial viscosity. Finally, the energy equation is updated for dissipation from the artificial viscosity.

Sub-step 3.: Energy is updated for compressional heating, viscous heating, vertical cooling and stellar irradiation.

2.2.2.1 Substep 1.

Sub-step 1. updates the 2D velocities according to pressure gradients, gravitational forces and curvature terms arising from the polar coordinates. The finite difference prescription is as follows [Stone and Norman, 1992].

$$\begin{aligned}\frac{v_{r_{i,j}}^{ss1} - v_{r_{i,j}}^{orig}}{\Delta t} = -\frac{(P_{i,j}^{orig} - P_{i-1,j}^{orig})}{r_i - r_{i-1}} \cdot \frac{2}{\rho_{i,j}^{orig} + \rho_{i-1,j}^{orig}} \\ + \frac{a_{g_{i,j}}^{orig} + a_{g_{i-1,j}}^{orig}}{2} + \frac{[(v_{\Theta_{i,j}}^{orig} + v_{\Theta_{i,j+1}}^{orig} + v_{\Theta_{i-1,j}}^{orig} + v_{\Theta_{i-1,j+1}}^{orig})/4]^2}{r_i^{inf}}\end{aligned} \tag{2.11}$$

$$\frac{v_{\phi_{i,j}}^{ss1} - v_{\phi_{i,j}}^{orig}}{\Delta t} = -\frac{(P_{i,j}^{orig} - P_{i,j-1}^{orig})}{(2\pi/N_\phi)r_i} \cdot \frac{2}{\rho_{i,j}^{orig} + \rho_{i,j-1}^{orig}} + \frac{a_{g_{i,j}}^{orig} + a_{g_{i,j-1}}^{orig}}{2} \tag{2.12}$$

The top index $ss1$ denotes a partial update (from this sub-step) of the quantity, whilst the top index $orig$ denotes the value of the quantity before the update. $P_{i,j}$ is the pressure at the centre of the cell, identified by indexes i, j. $\rho_{i,j}$ is the volumetric density at the centre of the cell. $a_{g_{i,j}}$ is the gravitational acceleration acting on the cell.

2.2.2.2 Substep 2.

In FARGO_THORIN, sub-step 2 is further divided into three actions.

1. The viscous stress tensor as described in section 1.3.4 is updated with the updated velocities from the first sub-step.
2. Using the updated viscous stress tensor, the velocities are again updated due to the divergence of the viscous stress tensor in eq. 4.9.
3. THE artificial viscosity is imposed to prevent discontinuities in the quantities that would break down the finite difference method. If a shock arises, the artificial viscosity will spread it over a defined number of cells in a smooth manner. The artificial viscosity follows from the formula [Stone and Norman, 1992]:

$$q_1 = \begin{cases} C^2 \rho_{i,j} (v_{r_{i+1,j}} - v_{r_{i,j}})^2 & \text{if } (v_{r_{i+1,j}} - v_{r_{i,j}}) < 0. \\ 0 & \text{otherwise.} \end{cases} \tag{2.13}$$

$$q_2 = \begin{cases} C^2 \rho_{i,j} (v_{r_{i,j+1}} - v_{r_{i,j}})^2 & \text{if } (v_{r_{i,j+1}} - v_{r_{i,j}}) < 0. \\ 0 & \text{otherwise.} \end{cases} \tag{2.14}$$

   C defines the number of cells over which the shock is spread. In a real fluid, viscosity would spread the shock only over a few particle mean free paths, here $C = 1.41$ so that the shock is spread over multiple zones. To minimize the effect of this in parts of the mesh with smooth transitions, notice that the artificial viscosity is proportional to the strength of the discontinuity. The finite difference update is conducted in the following procedure [Stone and Norman, 1992]:

$$\frac{v_{r_{i,j}}^{ss2} - v_{r_{i,j}}^{ss1}}{\Delta t} = -\frac{(q_{1_{i,j}} - q_{1_{i-1,j}})}{r_i - r_{i-1}} \cdot \frac{2}{\rho_{i,j}^{orig} + \rho_{i-1,j}^{orig}} \tag{2.15}$$

$$\frac{v_{\phi_{i,j}}^{ss2} - v_{\phi_{i,j}}^{ss1}}{\Delta t} = -\frac{(q_{2_{i,j}} - q_{2_{i,j-1}})}{(2\pi/N_\phi)r_i} \cdot \frac{2}{\rho_{i,j}^{orig} + \rho_{i,j-1}^{orig}} \tag{2.16}$$

$$\frac{\epsilon_{i,j}^{ss2}-\epsilon_{i,j}^{ss1}}{\Delta t} = -q_{1_{i,j}}\frac{v_{r_{i+1,j}}-v_{r_{i,j}}}{r_{i+1}^{inf}-r_{i}^{inf}} - q_{2_{i,j}}\frac{v_{\phi_{i,j+1}}-v_{\phi_{i,j}}}{(2\pi/N_{\phi})r_i} \tag{2.17}$$

For simplification top index $ss1$ is kept even though the velocities were updated at the beginning of this sub-step. The coordinates with the top index inf denote the coordinates of the interfaces.

2.2.2.3 Substep 3.

The third sub-step accounts for all sink and source terms in the energy equation 4.10. This is conducted with an implicit scheme. By applying the equation of state 1.109, we can derive an equation for the source step part of the energy equation 4.10. We can then apply the following approximation for Q_{vert} as defined in equation 1.120 to linearize the temperature [Chrenko et al., 2017].

$$\begin{aligned}(Q_{\text{vert}})_{i,j} &= \frac{2\sigma_{\text{B}}}{(\tau_{\text{eff}})_{i,j}}\left(T_{i,j}^{\text{old}}\right)^4\left(1+\frac{T-T^{\text{old}}}{T^{\text{old}}}\right)^4_{i,j} \\ &\approx \frac{2\sigma_{\text{B}}}{(\tau_{\text{eff}})_{i,j}}\left[4\left(T^{\text{old}}\right)^3 T - 3\left(T^{\text{old}}\right)^4\right]_{i,j} \equiv \left(Q'_{\text{vert}}\,T - Q''_{\text{vert}}\right)_{i,j}.\end{aligned} \tag{2.18}$$

T^{old} is the temperature from the previous time step, otherwise, we follow the same notation as in section 1.3. The source terms of the energy equation in the finite difference approximation can now be rearranged into a matrix equation of the form:

$$A_{i,j}T_{i,j} + B_{i,j}T_{i+1,j} + C_{i,j}T_{i-1,j} + D_{i,j}T_{i,j+1} + E_{i,j}T_{i,j-1} = T_{i,j}^{\text{old}} + \Delta t\left(\frac{Q_{\text{visc}} + Q_{\text{irr}} + Q''_{\text{vert}}}{\Sigma c_V}\right)_{i,j} \tag{2.19}$$

c_V is the specific heat capacity at constant volume. The successive over-relaxation method is implemented to solve this linear problem [Chrenko et al., 2017].

2.2.3 Transport step

The transport step finds solutions to the fluid advection terms in the hydrodynamical equations [Stone and Norman, 1992].

$$\frac{d}{dt}\int_V \rho dV = -\int_S \rho\vec{v}\cdot d\vec{S} \tag{2.20}$$

$$\frac{d}{dt}\int_V \rho v dV = -\int_S \rho v^2\hat{v}\cdot d\vec{S} \tag{2.21}$$

$$\frac{d}{dt}\int_V \epsilon dV = -\int_S \epsilon\vec{v}\cdot d\vec{S} \tag{2.22}$$

V denotes the gas cell volume. The equations above state that the rate of change within a gas cell is equal to the divergence of the flux through the interfaces of the cells. The flux $\mathcal{F}_{i,j}^{k}$ of a hydrodynamical quantity q in the k-th direction is equal to:

$$\mathcal{F}_{i,j}^{k} = \langle v_{i,j}^{k} q_{i,j}^{inf_k}\tilde{S}_{i,j}^{k}\rangle \tag{2.23}$$

The top index inf_k denotes the value of the quantity at the centre of the interface in the k-th direction and $\tilde{S}_{i,j}^{k}$ is the area of the respective interface. Angle brackets represent centring in time. To ensure conservation, all fluxes are computed at the same time and the same flux is used for cells on the two sides of the interface. Directional splitting is used to compute the integration [Stone and Norman, 1992]. For a quantity q in the cell the following procedure is followed:

$$\frac{q_{i,j}^{ds1}V_{i,j} - q_{i,j}^{orig}V_{i,j}}{\Delta t} = -\left[\left\langle v_{r_{i+1,j}} q_{i+1,j}^{inf_r}\tilde{S}_{i+1,j}^{r}\right\rangle - \left\langle v_{r_{i,j}} q_{i,j}^{inf_r}\tilde{S}_{i,j}^{r}\right\rangle\right] \tag{2.24}$$

$$\frac{q_{i,j}^{ds2}V_{i,j} - q_{i,j}^{ds1}V_{i,j}}{\Delta t} = -\left[\left\langle v_{\phi_{i,j+1}} q_{i,j+1}^{inf_\phi}\tilde{S}_{i,j+1}^{\phi}\right\rangle - \left\langle v_{\phi_{i,j}} q_{i,j}^{inf_\phi}\tilde{S}_{i,j}^{\phi}\right\rangle\right] \tag{2.25}$$

2.2.3.1 van Leer's second-order upwind interpolation

Values of scalar hydrodynamical quantities on the mesh are saved as values at the centre of the cell, so the question remains how to obtain values q^{inf} at the centres of the interfaces between the cells, in order to use them in the transport step? The values of quantities are extrapolated to the cell interfaces using van Leer's second-order upwind interpolation [Van Leer, 1977]. The method uses linear functions to approximate the profile of a quantity within a cell. To ensure stability, the value at a certain interface is extrapolated from the value upstream (at the centre of THE neighbouring cell). Stability further requires that no local minima are created, so that no quantity 'blows up' within a certain cell. This is ensured by a condition requiring monotonicity, that is advection must be followed by advection. For a certain quantity, the interpolation is obtained by the following formula.

$$q_i^{inf} = \begin{cases} q_{i-1} + (\Delta x_{i-1} - v_i \Delta t)\,(dq_{i-1}/2) & \text{if} \quad v_i > 0 \\ q_i - (\Delta x_i + v_i \Delta t)\,(dq_i/2) & \text{if} \quad v_i < 0 \end{cases}, \tag{2.26}$$

$$dq_i = \begin{cases} \frac{2(\Delta q_{i-1/2} \Delta q_{i+1/2})}{\Delta q_{i-1/2} + \Delta q_{i+1/2}} & \text{if } \Delta q_{i+1/2} \Delta q_{i-1/2} > 0 \\ 0 & \text{otherwise} \end{cases}, \tag{2.27}$$

$$\Delta q_{i+1/2} = (q_{i+1} - q_i)/\Delta x_i$$

where Δx_i denotes the width of a cell.

2.3 Fargo algorithm

The original version of the FARGO code was first presented in [Masset, 2000], where also the FARGO algorithm is described. The length of the time-step Δt in hydrodynamical simulations is limited by the Courant-Friedrichs–Lewy (CFL) condition for stability, for the azimuthal component of the flow in the above-described set-up the condition can be written as:

$$\frac{v^\phi \Delta t}{r \Delta \phi} \leq 1 \tag{2.28}$$

WHERE v^ϕ denotes the azimuthal velocity, r the radial component and $\Delta\phi$ the azimuthal angle width of a single cell. The condition states that the time step must be chosen so that in one time step the fluid does not enter OR leave a cell. In simulations of accretion discs, where azimuthal velocities are high and it is often the goal to study a long-term evolution of THE system, the CFL condition leads to exceedengly long computational times. The FARGO algorithm allows for a much larger time step, because it treats the azimuthal advection in the following manner [Masset, 2000]. First, let the average azimuthal velocity $\bar{v}_i^\phi$ in a ring at some radius be calculated:

$$\bar{v}_i^\phi = \frac{1}{N_\phi} \sum_{j=0}^{N_\phi - 1} v_{ij}^\phi \tag{2.29}$$

The azimuthal velocity of a fluid in a certain cell can be split to a sum of three parts:

$$v_{ij}^\phi = v_{ij}^{\phi_{\rm res}} + v_{ij}^{\phi_{\rm dec}} + v_i^{\phi_{\rm int}} \tag{2.30}$$

the residual velocity $v_{ij}^{\phi_{\rm res}}$ is the deviation of the azimuthal velocity in a cell from the rings' average:

$$v_{ij}^{\phi_{\rm res}} = v_{ij}^\phi - \bar{v}_i^\phi \tag{2.31}$$

The average velocity can be further split to the sum of $v_{ij}^{\phi_{\rm dec}}$ and $v_i^{\phi_{\rm int}}$. Where the $v_i^{\phi_{\rm int}}$ component moves the fluid an exact integer number of cells.

$$v_{ij}^{\phi_{\rm dec}} = \bar{v}_i^\phi - \mathrm{int}\left[\bar{v}_i^\phi \frac{\Delta t}{\Delta y_i}\right] \frac{\Delta y_i}{\Delta t} \tag{2.32}$$

$$v_i^{\phi_{\mathrm{int}}} = \mathrm{int}\left[\bar{v}_i^{\phi}\frac{\Delta t}{\Delta y_i}\right]\frac{\Delta y_i}{\Delta t} \tag{2.33}$$

$$\Delta y_i = \frac{r_i + r_{i+1}}{2}\Delta\Theta \tag{2.34}$$

The int[a] function outputs the integer part of a. The advection during one time step is then split into three sub-steps [Masset, 2000].

- The fluid is transported due to the residual velocity $v_{ij}^{\phi_{\mathrm{res}}}$. The motion of the fluid is always less than half of the extent of a cell.
- The fluid is transported due to the decimal part of the average velocity in the ring $v_{ij}^{\phi_{\mathrm{dec}}}$. Again this results in a motion smaller than half a step.
- The content of the cell is copied exactly into a cell down-stream in the ring, that is $v_i^{\phi_{\mathrm{int}}}\Delta t$ from the ring.

The last step, which represents the largest part of the motion does not introduce any numerical diffusion [Masset, 2000], hence the CFL condition is greatly improved and a longer time step can be chosen.

$$\frac{v_{ij}^{\phi_{\mathrm{res}}}\Delta t}{\Delta y_i} \leq 1 \tag{2.35}$$

This algorithm allows the FARGO code to greatly reduce computational time and allows for practical applications.

2.4 Code units in FARGO_THORIN

Here we list transformations to the code units used in FARGO_THORIN.

$$1\ c.u._M = 1\, M_\odot \tag{2.36}$$

$$1\ c.u._r = 1\,\mathrm{AU} \tag{2.37}$$

$$1\ c.u._t = \frac{1}{2\pi}\ \text{sidereal yr} = 1\,\Omega_{\odot\mathrm{K}}^{-1} = \sqrt{\frac{(1\,\mathrm{AU})^3}{GM_\odot}}\ \text{ in seconds} \tag{2.38}$$

$$1\ c.u._T = \frac{\mu}{\mathcal{R}}(1\,\mathrm{AU})^2\left(\frac{1}{2\pi}\,\mathrm{yr}\right)^{-2} = \frac{\mu}{\mathcal{R}}\frac{GM_\odot}{1\,\mathrm{AU}}\ \text{ in Kelvins} \tag{2.39}$$

$$1\ c.u._E = M_\odot(1\,\mathrm{AU})^2\left(\frac{1}{2\pi}\,\mathrm{yr}\right)^{-2} = \frac{GM_\odot^2}{1\,\mathrm{AU}}\ \text{ in Joules} \tag{2.40}$$

$$1\ c.u._P = M_\odot\left(\frac{1}{2\pi}\,\mathrm{yr}\right)^{-2}\ \text{ in Pascals meters} \tag{2.41}$$

3. Dynamical constraints for the β Lyrae A system

In this chapter, we discuss observations of the β Lyrae A system and use analytical models to interpret them. We aim to use the profiles of hydrodynamic quantities generated by the models from this chapter as initial conditions and parameters for numerical simulations with the FARGO_THORIN code [Chrenko et al., 2017] in chapter 4. We conduct it in two steps; first, we compare profiles obtained by [Brož et al., 2021] to models of accretion discs derived by [Shakura and Sunyaev, 1973], and second, we extend these classical models for a general opacity function in the form $\kappa = \kappa_0 \rho^A T^B$. Lastly, we apply these models to the studied β Lyrae A system.

3.1 Observed parameters of β Lyr A

The β Lyr A system is an eclipsing binary undergoing mass transfer; the gainer in the system is an early B star of mass $m_{\mathrm{g}} = 13.048\,M_\odot$ and the less massive donor with $m_{\mathrm{d}} = 2.910\,M_\odot$ is a late B type star. Evidence of A circumstellar material was first presented by [Baxandall and Stratton, 1930], who noticed additional redshifted absorption lines just before the middle of the primary eclipse [Harmanec, 2002]. Observations show the binary's orbital period $P = 12.9440\,\mathrm{days}$ (in 2020) is increasing at a rate of $\dot{P} = 19\,\mathrm{s}$ per yr, which corresponds to a mass transfer rate of $\dot{M} = 2 \cdot 10^{-5}\,M_\odot\,\mathrm{yr}^{-1}$ [Brož et al., 2021].

The circumstellar material in the system was recently studied in [Mourard et al., 2018] and [Brož et al., 2021]. [Brož et al., 2021] fitted a kinematic model to spectroscopic, light-curve, spectral energy distribution, interferometric and differential interferometric data. In this text, we extend their work by adding dynamics into consideration. In our modelling efforts, some parameters are fixed, similarly to in their kinematic model, we adopt the same value for the following:

Table 3.1: Adopted fixed parameters. [Brož et al., 2021]

Parameter	Unit	Value
$R_\star$	$R_\odot$	5.987
$T_\star$	K	30000
$M_\star$	$M_\odot$	13.048
q	1	0.223
$\dot{M}$	$M_\odot\mathrm{yr}^{-1}$	$2 \cdot 10^{-5}$

$R_\star$ denotes the radius of the primary (gainer), $T_\star$ its effective temperature, $M_\star$ mass, q mass ratio. $\dot{M}$ is not a parameter of their model but we adopt this value as fixed in ours. We also adopt the inner and outer disc boundaries from Brož et al. [2021], namely from their "Joint" model.

Table 3.2: Adopted disc boundaries [Brož et al., 2021]

Parameter	Unit	Value
R_{innb}	$R_\odot$	5.987
R_{outnb}	$R_\odot$	31.5

R_{innb} and R_{outnb} denote the inner and outer disc boundaries, respectively.

During a detailed review of the code used in Brož et al. [2021], we found that they assumed the mean molecular weight $\mu_{\mathrm{Broz2021}} \approx 2.36$ and the adiabatic index $\gamma_{\mathrm{Broz2021}} = 1.0$, which are values typical rather for cool protoplanetary discs [Kimura et al., 2016]. However, the circumstellar environment of the

β Lyr A system is much hotter and a composition closer to pure ionised hydrogen should be assumed. Actually, one of the converged parameters in their model is h_{cnb}, defined as

$$H = h_{\mathrm{cnb}} \cdot H_{\mathrm{hydrostatic}}\,, \tag{3.1}$$

where H denotes the pressure scale height of the disc and $H_{\mathrm{hydrostatic}}$ the pressure scale height in the case of vertical hydrostatic equilibrium. Their model converged at $h_{\mathrm{cnb}} = 3.8$ and they interpreted this as the disc being vertically unstable. We suspect that at least a part of this is due to the fixed choice of μ_{Broz2021} and $\gamma_{\mathrm{Broz2021}}$. Hence, when we compare our results to a *modified* version of their model with $h_{\mathrm{cnb,static}} = 1.0$, $\mu_{\mathrm{static}} = 0.5$ and $\gamma_{\mathrm{static}} = 1.4$, we refer to it throughout the text as the "Vertically hydrostatic model". Let us emphasise that we do not claim that the Brož et al. [2021] disc must be in vertical equilibrium, we use this modified model as a hydrostatic limit of the Brož et al. [2021] disc, which we then compare to analytical models, where the hydrostatic equilibrium is strictly enforced.

Out of the profiles studied in Mourard et al. [2018] and Brož et al. [2021], we give the most weight to the temperature profile (fig. 3.1). The authors point out that their $T(r)$ profile is in good agreement with the theory of steady-state accretion discs $T \propto R^{-\frac{3}{4}}$ [Pringle, 1981, Shakura and Sunyaev, 1973] and the inner boundary temperature is close to the temperature of the star (as inferred from the spectral type) which would make sense assuming thermal equilibrium. The observations constrain mostly the outer part of the disc. When [Mourard et al., 2018] compare different models of the disc, they are in good agreement from $10R_\odot$ outwards. We should thus consider the outer part of the disc as well constrained. [Brož et al., 2021] also considered an additional shell around the disc. The shell adds an extra layer of matter that dims the disc resulting in a higher temperature implied by the observations in the kinematic model.

The vertically integrated density Σ given by [Brož et al., 2021] should be interpreted as a lower limit because the densities of the optically thick medium are not well constrained by observation. Since the volume density ρ is given by

$$\rho = \frac{\Sigma}{\sqrt{2\pi}H} \tag{3.2}$$

and, as we discussed above, we expect the true H to be lower, ρ is also a lower limit.

The above-discussed profiles are plotted in figs. 3.1, 3.2, 3.3, and 3.5, next to profiles inferred from analytical models derived by [Shakura and Sunyaev, 1973].

3.2 Classical Shakura–Sunyaev models

At first, we compare the fits of observations from [Brož et al., 2021] to the analytical models of [Shakura and Sunyaev, 1973] (figs. 3.1, 3.2, 3.3, 3.4 and 3.5). These analytical models were derived with the assumption that:

$$Q_{\mathrm{visc}} = Q_{\mathrm{vert}}\,, \tag{3.3}$$

where Q_{visc} is the work conducted by viscous forces in the disc and Q_{vert} is cooling by radiation from the face of the disc. In other words, the assumption is that all energy produced within the disc by viscous forces is radiated away and there are no other energy sources or sinks. The analytical models assume the equation an equation state combining the ideal gas and radiation:

$$P = \rho \frac{k_B T}{\mu m_p} + \frac{4\sigma_B}{3c} T^4\,. \tag{3.4}$$

Shakura and Sunyaev [1973] derived three models, assuming a different dominant pressure term and a dominant source of opacity:

- $P_{\mathrm{g}} \ll P_{\mathrm{r}}$ and the Thompson scattering is the source of opacity:

$$\kappa = \frac{\sigma_{\mathrm{thomp}}}{m_p}$$

- $P_{\mathrm{g}} \gg P_{\mathrm{r}}$ and the Thompson scattering is the source of opacity:

$$\kappa = \frac{\sigma_{\mathrm{thomp}}}{m_p}$$

- $P_{\mathrm{g}} \gg P_{\mathrm{r}}$ and free-free absorption is the source of opacity:

$$\kappa = 7.36 \cdot 10^{22} \rho T^{-\frac{7}{2}}$$

where σ_{thomp} denotes the cross-section of the Thompson scattering. These approximations are used to neglect the negligible of the equation of state and other sources of opacity. For each studied quantity q, Shakura and Sunyaev [1973] give a profile in the form of:

$$q = q(\alpha, M_\star, \dot{M}, R) \tag{3.5}$$

We use their profiles for T, Σ and H; for each profile, we use the parameters given in tab. 3.1 and different orders of magnitude for α, where α is the parameterization of viscosity introduced in section 1.2.4.4. Note that the models were originally derived for different parts of accretion discs around black holes and so, especially the normalisation constants given by [Shakura and Sunyaev, 1973], may not be simply applicable to a stellar case.

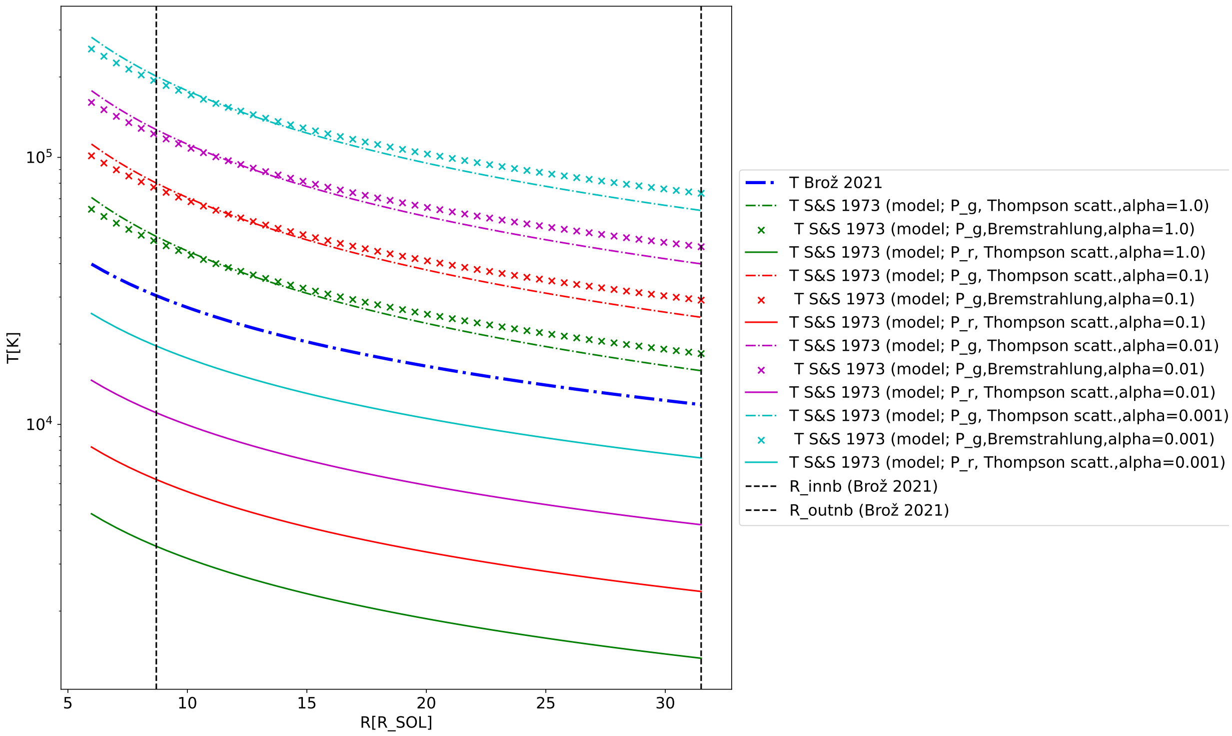

Figure 3.1: Observed temperature profiles and the classical Shakura-Sunyaev models. The temperature profile obtained by Brož et al. [2021] by fitting a kinematic model (denoted as "Joint") to all available observations is compared to computed temperature profiles based on the models from Shakura and Sunyaev [1973], computed for parameters of the β Lyrae system and $\alpha = 10^{-1}, 10^{-2}, 10^{-3}$. Models which assume that $P_g \gg P_r$ show systematically larger temperatures than those that assume $P_g \ll P_r$. A lower α leads to higher temperatures.

Temperature profile. In fig. 3.1, we plotted the theoretical temperature profiles for different values of the α parameter. We see no models are in good agreement with the Brož et al. [2021] kinematic model. For $P_{\mathrm{g}} \gg P_{\mathrm{r}}$ models, the green curves represent $\alpha = 1.0$, which is the upper limit case, hence these models never reach the "Brož 2021" temperature profile. We could get a relatively good agreement with the "Brož 2021" temperature profile only by adopting a very low α parameter, close to 10^{-4}.

On the other hand analytical models that assume $P_{\rm g} \gg P_{\rm r}$ predict an order of a magnitude higher temperatures than those with $P_{\rm g} \ll P_{\rm r}$. We consider this to be 'suspicious' — due to the $P_{\rm r} \propto T^4$ dependence compared to the $P_{\rm g} \propto T$ we would expect that $P_{\rm r}$-dominant models would be more consistent with relatively higher temperatures. (Note: we suspect there is an error in Shakura and Sunyaev [1973], in the temperature profile given for $P_{\rm g} \ll P_{\rm r}$. Taking their eq. (2.10) with the $\frac{1}{4}$ power as instructed implies $T \propto r^{-\frac{3}{8}}$ but their eq. (2.12) states $T \propto r^{-\frac{3}{4}}$.)

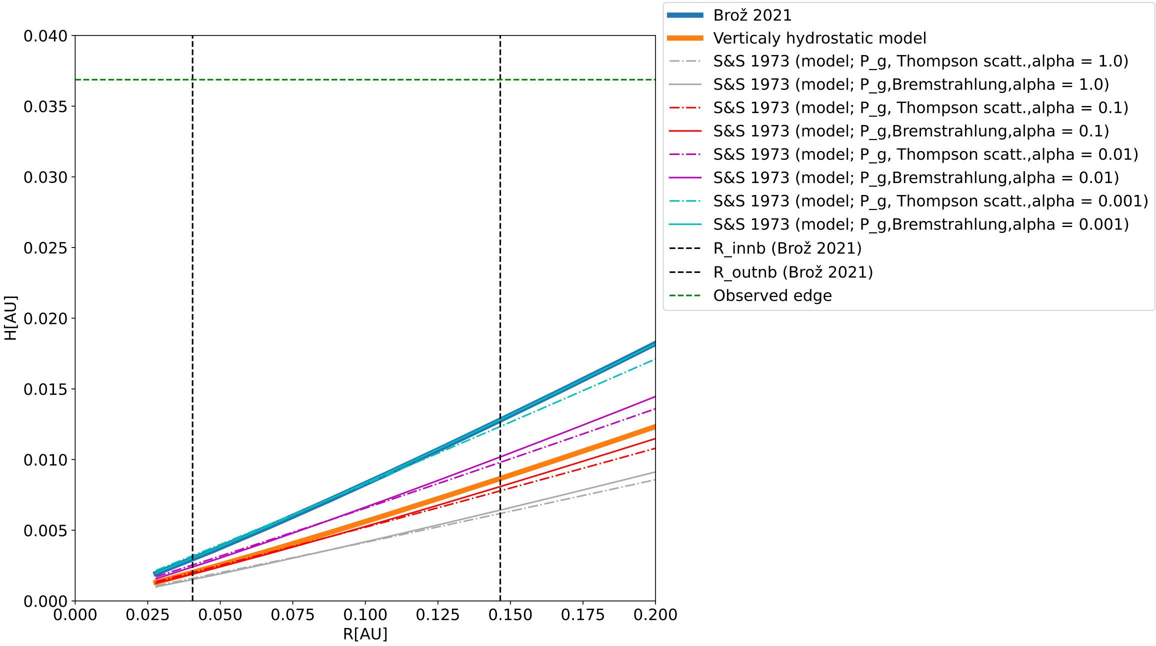

Figure 3.2: Disc pressure scale-height derived from fits of observations compared with the Shakura-Sunyaev models. The "Brož 2021" profile was obtained by Brož et al. [2021] from fitting a kinematic model to spectroscopic observations. The "Vertically hydrostatic model" was derived from Brož et al. [2021] profile by modifying the parameters $h_{\rm cnb}$, μ, γ (see the main text). Other profiles were computed from models of Shakura and Sunyaev [1973] for parameters of the β Lyrae system and $\alpha = 1.0, 10^{-1}, 10^{-2}, 10^{-3}$. The only non-hydrostatic model ("Brož 2021") shows the largest H. Shakura-Sunyaev models show larger H for lower α parameters.

Pressure scale-height profile. Only the [Brož et al., 2021] kinematic model is non-hydrostatic in the vertical direction; all other models assume a hydrostatic equilibrium in the vertical direction. In fig. 3.2, we compare different profiles and for reference, we also plot the observed vertical extent of the disc (from observations in [Mourard et al., 2018]). We note that the pressure scale height is not the same thing as the observed extent. Moreover, the definition of H varies in different works, usually by a multiplicative factor of $\sqrt{2\pi}$, but in [Brož et al., 2021] the definition is as follows; when the vertical coordinate (in the cylindrical system) is $z = \sqrt{2}H$, then the volumetric density ρ is $\frac{1}{e}$ times smaller than in the mid-plane. On the contrary, the observed extent is equal to the height where the disc becomes transparent.

All models give $H(r)$ profiles that satisfy the thin disc approximation $H \ll R$. The only vertically unstable profile ("Brož 2021") shows the largest vertical extent of the disc; that is to be expected. The "Vertically hydrostatic model" is in relatively good agreement with models where $P_{\rm pg}$ dominates and $\alpha = 0.1$. The $H(r)$ profile for the models with $P_{\rm r} \gg P_{\rm g}$ is two orders of magnitude smaller than in the other models, so it is plotted separately (in fig. 3.3). We take this large difference to be an argument against the radiation pressure-dominated models.

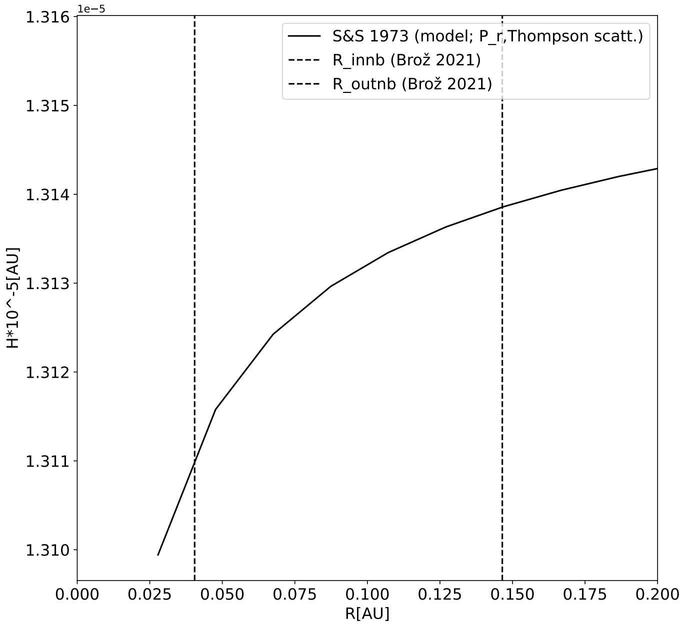

Figure 3.3: Disc pressure scale-height computed from a [Shakura and Sunyaev, 1973] model with the dominant radiation pressure P_r and the Thompson scattering. This model leads to a very flat disc for parameters of the β Lyrae system and is independent of α.

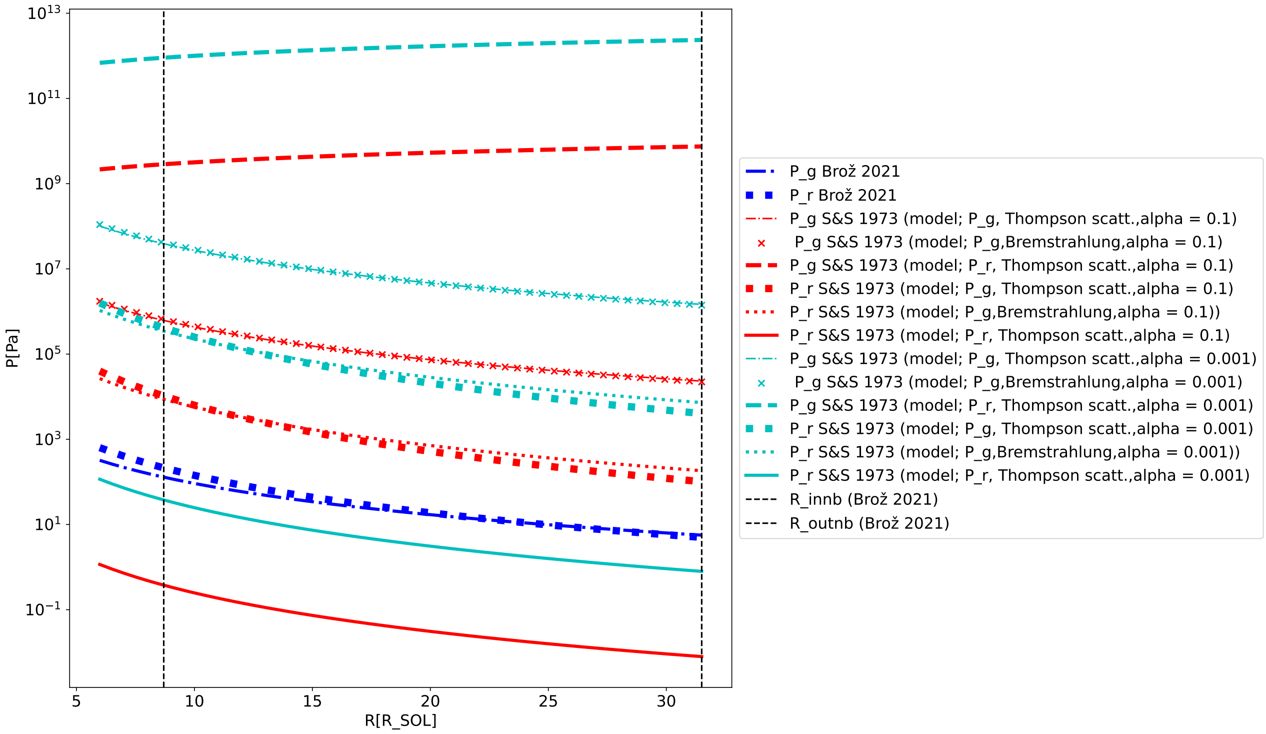

Figure 3.4: Ideal gas pressure and radiation pressure computed from kinematic model fits of observations and [Shakura and Sunyaev, 1973] models. Ideal gas pressure P_g is given as the first part of the equation of state 3.17 and radiation pressure P_r as the second part. For the "Brož 2021" curves the ρ and T profiles from the "Joint" model from [Brož et al., 2021] are used. For the "S&S" pressure profiles parameters of the β Lyrae system and $\alpha = 10^{-1}, 10^{-3}$ are used. For observed profiles $P_\mathrm{r} \approx P_\mathrm{g}$. "S&S" models derived under the assumption $P_\mathrm{g} \gg P_\mathrm{r}$ show P_g almost a 100 times larger than P_r. Results from "S&S" models derived assuming $P_\mathrm{g} \ll P_\mathrm{r}$ are in conflict with this assumption (for β Lyrae system parameters).

Ideal gas and radiation pressure profiles. Although each model assumes that either the ideal gas pressure or the radiation pressure is negligible, we can for each model calculate both pressures from the obtained T and ρ profiles to see if they are consistent with the assumption under which the model was derived. In fig. 3.4 we plot both the gas and radiation pressures computed for the [Brož et al., 2021] and [Shakura and Sunyaev, 1973] models, using $\alpha = 10^{-1}, 10^{-3}$. We observe that:

[Brož et al., 2021]: We see that as they are the ("Brož 2021") profiles show radiation and ideal gas pressure profiles of similar magnitudes. Our goal is to decide assumptions of which model $P_g \ll P_r$, $P_g \gg P_r$ or $P_g \approx P_r$ coincide with the β Lyrae system. However, we cannot come to a final conclusion simply by looking at the respective profiles, because none of the three possibilities can be ruled out. The three cases to be considered are:

1. The profiles are correct and we can consider the two pressures as of approximately the same importance ($P_\mathrm{g} \approx P_\mathrm{r}$).
2. Because the densities should be interpreted as lower limits, the real density can be significantly larger, and since $P_\mathrm{g} \propto \rho$, we can get $P_\mathrm{g} \gg P_\mathrm{r}$.
3. Especially in the inner part of the disc, the temperature profile is uncertain [Mourard et al., 2018], so we may also consider temperatures to be higher. The mid-plane temperature profile in [Brož et al., 2021] is inferred from observations of the disc's atmosphere. Hot circumstellar matter can be thought of as stellar matter hence modes of energy transfer in the vertical direction must be considered (radiative transfer/vertical convection of some form). Higher temperatures in the disc could lead to increased radiation pressure.

- The results from models assuming $P_\mathrm{g} \gg P_\mathrm{r}$ are consistent with this assumption throughout the disc.
- The results from models assuming $P_\mathrm{g} \ll P_\mathrm{r}$ aren't consistent with this assumption anywhere in the disc.

We take this as an argument against the dominance of the radiation pressure in the case of β Lyr A.

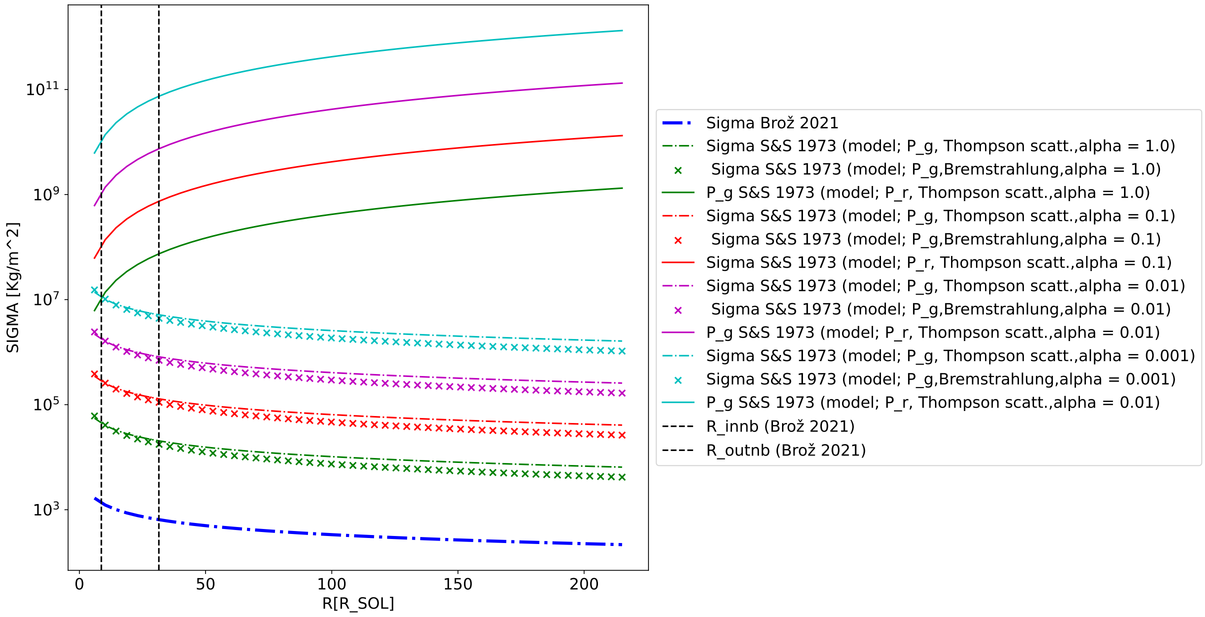

Figure 3.5: Vertically integrated density Σ computed for the kinematic model from Brož et al. [2021] ("Brož 2021") and Shakura and Sunyaev [1973] models ("S&S"), with parameters of the β Lyrae system and $\alpha = 1.0, 10^{-1}, 10^{-2}, 10^{-3}$. All "S&S" models show higher Σ profiles than the kinematic model ("Brož 2021").

Vertically integrated density profile. All models are compared in fig. 3.5. All Shakura and Sunyaev [1973] models predict a higher vertical integrated density Σ than the kinematic model, Which is not 'critical' since the latter is a lower limit. For the pressure scale height in 3.2, the best agreement is between the vertically hydrostatic model and $P_\mathrm{g} \gg P_\mathrm{r}$ models with α close to 0.1. If we compare analytical Σ to the kinematic Σ, we see that the analytic model implies a surface density profile about two orders of a magnitude higher at all radii. We take this as an argument that should be more massive in order to transfer $2 \cdot 10^{-5}\, M_\odot\, \mathrm{yr}^{-1}$.

3.3 Modified Shakura–Sunyaev models

In the previous section, we compared the kinematic model from Brož et al. [2021] to models from Shakura and Sunyaev [1973] and showed that there isn't a good agreement. In the following text, we describe models we derived following the same steps as Shakura and Sunyaev [1973] but using a slightly modified set of equations. The set of equations was chosen to...

1. better describe a case where the accreting central object is a star;
2. be consistent with the equations used in the FARGO_THORIN code [Chrenko et al., 2017].

In the discussion of the pressure profiles 3.4, we demonstrated that none of the three cases of the relative importance of the pressure terms ($P_g \ll P_r$, $P_g \gg P_r$ or $P_g \approx P_r$) could be ruled out, hence we derive models for each case separately. We generalised the models by assuming the opacity law in the form of

$$\kappa = \kappa_0 \rho^A T^B. \tag{3.6}$$

We then adopted the function of opacity $\kappa = \kappa(\rho, T)$ from Rogers and Iglesias [1992]. To this function, we found approximations of regions indicated as important in the discussion above. The approximations were optimized by converging parameters A, B as well as κ_0 form eq. 3.6, using the least mean square method, fitting different ranges of temperature and density. For each case of the pressure terms (P_g, P_r) importance we experimented with a few different opacities and here we present those that are either in good agreement with the kinematic model or demonstrate something important. Apart from model-specific discussions, we will always:

1. check that the applied assumption about the pressure ($P_\mathrm{g} \ll P_\mathrm{r}$, $P_\mathrm{g} \gg P_\mathrm{r}$ or $P_\mathrm{g} \approx P_\mathrm{r}$) holds in the case of β Lyrae A parameters (tab. 3.1).
2. compare the resulting temperature profile to [Brož et al., 2021], which (as was discussed above) is the most trustworthy out of the adopted profiles.

3.3.1 Full set of equations.

We omit the full derivation of each model and refer the reader to Shakura and Sunyaev [1973], Pringle [1981] for a detailed description. Here we state the set of equations that are the same for all models. Case-specific steps or equations are described in sections detailing them.

1. Integrating the volume density ρ over the vertical coordinate is equal to A multiplication by the two times disc's semi-thickness H (pressure scale-height), this gives the vertically integrated density Σ as:
$$\Sigma = 2H\rho \tag{3.7}$$
2. The pressure scale height H assuming the hydrostatic equilibrium is given by the ratio of sound speed c_s and the Keplerian angular velocity Ω_K (as derived in section 1.2) [Pringle, 1981]:
$$H = c_s R \sqrt{\frac{R}{GM_\star}} \tag{3.8}$$

3. A general equation for the sound speed c_s in an isothermal case, independent of the equation of state [Shakura and Sunyaev, 1973]:
$$c_s = \sqrt{\frac{P}{\rho}} \tag{3.9}$$

4. Energy dissipation by viscous forces per unit of area per unit of time assuming a steady-state solution to a Keplerian disc (as in eq. 1.59) is given by [Pringle, 1981]:
$$Q_{\text{visc}} = \frac{3GM\dot{M}}{8\pi R^3}\left(1 - \sqrt{\frac{R_\star}{R}}\right) \tag{3.10}$$

5. Energy is only radiated away through the two faces of the disc at $z = H$ after travelling through a layer of gas with the effective optical depth τ_{eff}. T denotes the mid-plane temperature. The cooling is given by the Stefan-Boltzmann law (same as eq. 1.120):
$$Q_{\text{vert}} = \frac{2\sigma_B T^4}{\tau_{\text{eff}}} \tag{3.11}$$

6. The disc is assumed to be optically thick. The optical depth of the disc's gas is determined by the model atmosphere according to Hubený [1990], in the optically thick limit.
$$\tau_{\text{eff}} = \frac{3}{8}\tau_{\text{opt}} \tag{3.12}$$
the optical depth τ_{opt} of the vertical layer is approximated as in Chrenko et al. [2017]:
$$\tau_{\text{opt}} = \frac{C_k}{2}\kappa\Sigma \tag{3.13}$$
where the C_k factor accounts for the opacity change above the mid-plane as suggested by comparisons of 3D and 2D models [Müller and Kley, 2012]. The factor is set to $C_k = 0.6$, the same as is suggested for FARGO_THORIN by Chrenko et al. [2017].

7. Assumed energy balance; all the energy from viscous dissipation is radiated away.
$$Q_{\text{visc}} = Q_{\text{vert}} \tag{3.14}$$

8. For a given kinematic viscosity ν, the Σ profile in a steady state Keplerian disc (eq. 1.64) is given by [Pringle, 1981]:
$$\nu\Sigma = \frac{\dot{M}}{3\pi}\left(1 - \sqrt{\frac{R_\star}{R}}\right) \tag{3.15}$$

9. The standard [Shakura and Sunyaev, 1973] approximation of the kinematic viscosity is (derived in section 1.2.4.4):
$$\nu = \alpha c_s H \tag{3.16}$$

10. The equation of state combining the ideal gas and radiation pressure $P = P_{\text{g}} + P_{\text{r}}$ is in its full form given by;
$$P = \rho\frac{k_B T}{\mu m_p} + \frac{4\sigma_B}{3c}T^4 \tag{3.17}$$
where σ_B is the Stefan-Boltzmann constant, c is the speed of light, k_B the Boltzmann constant, μ the mean molecular weight, m_p the mass of the proton, T the mid-plane temperature and ρ the mid-plane density. For simplicity, we assumed the disc is made of pure ionised hydrogen and chose $\mu = 0.5$. The equation of state is further modified by approximations defining each case.

11. The opacity approximation in its general form.
$$\kappa = \kappa_0\rho^A T^B \tag{3.18}$$
A choice of A,B and κ_0 then defines each model.

3.3.2 Models with $P_{\mathrm{g}} \gg P_{\mathrm{r}}$ assumed

In the case of dominant ideal gas pressure ($P_{\mathrm{g}} \gg P_{\mathrm{r}}$) we neglect the radiation pressure in 3.17 and get:

$$P = \rho \frac{k_B T}{\mu m_p} \tag{3.19}$$

We then obtain the temperature profile from 3.9. The resulting class of models is defined by the following equations.

- To simplify notation, we denote the often appearing sum of exponenets as;

$$D = 3A - 2B + 10 \tag{3.20}$$

- Opacity profile in the disc is given by;

$$\kappa = \kappa_\star \alpha^{-\frac{7A+2B}{D}} \dot{M}^{\frac{4(A+B)}{D}} M^{\frac{(11A+6B)}{2D}} R^{-\frac{3(11A+6B)}{2D}} \left(1 - \sqrt{\frac{R_\star}{R}}\right)^{\frac{4(A+B)}{D}} \tag{3.21}$$

  Where...

$$\kappa_\star = \left(\kappa_0 \rho_0^A T_0^B\right)^{\frac{10}{D}} \tag{3.22}$$

- The pressure scale height in the disc is given by;

$$H = H_\star \alpha^{-\frac{D+7A+2B}{10D}} \dot{M}^{\frac{2D+4(A+B)}{10D}} M^{\frac{11A+6B-7D}{20D}} R^{\frac{3(7D-11A-6B)}{20D}} \left(1 - \sqrt{\frac{R_\star}{R}}\right)^{\frac{2D+4(A+B)}{10D}} \tag{3.23}$$

  Where...

$$H_\star = H_0 \kappa_\star^{\frac{1}{10}} \tag{3.24}$$

- The vertically integrated density in the disc is given by;

$$\Sigma = \Sigma_\star \alpha^{\frac{7A+2B-4D}{5D}} \dot{M}^{\frac{3D-4(A+B)}{5D}} M^{\frac{2D-(11A+6B)}{10D}} R^{\frac{3(11A+6B-2D)}{10D}} \left(1 - \sqrt{\frac{R_\star}{R}}\right)^{\frac{3D-4(A+B)}{5D}} \tag{3.25}$$

  Where...

$$\Sigma_\star = \Sigma_0 \kappa_\star^{-\frac{1}{5}} \tag{3.26}$$

- The temperature profile of the disc given by;

$$T = T_\star \alpha^{-\frac{7A+2B+D}{5D}} \dot{M}^{\frac{2D+4(A+B)}{5D}} M^{\frac{11A+6B+3D}{10D}} R^{-\frac{3(11A+6B+3D)}{10D}} \left(1 - \sqrt{\frac{R_\star}{R}}\right)^{\frac{2D+4(A+B)}{5D}} \tag{3.27}$$

  Where...

$$T_\star = T_0 \kappa_\star^{\frac{1}{5}} \tag{3.28}$$

Where the opacity-independent constants (subscript 0) are defined as;

-

$$H_0 = \left(\frac{1.8}{256 \cdot \sigma_B \pi^2 G^{\frac{7}{2}}} \left(\frac{k_B}{\mu m_p}\right)^4\right)^{\frac{1}{10}} \tag{3.29}$$

- $$\Sigma_0 = \left(\frac{1.8}{256 \cdot \sigma_B \pi^2 G^{\frac{7}{2}}} \left(\frac{k_B}{\mu m_p} \right)^4 \right)^{-\frac{1}{5}} \cdot (\sqrt{G} 3\pi)^{-1} \tag{3.30}$$

- $$\rho_0 = \left(\frac{1.8}{256 \cdot \sigma_B \pi^2 G^{\frac{7}{2}}} \left(\frac{k_B}{\mu m_p} \right)^4 \right)^{-\frac{3}{10}} \cdot (\sqrt{G} 6\pi)^{-1} \tag{3.31}$$

- $$T_0 = \left(\frac{1.8}{256 \cdot \sigma_B \pi^2 G^{\frac{7}{2}}} \left(\frac{k_B}{\mu m_p} \right)^4 \right)^{\frac{1}{5}} \cdot \frac{\mu m_p G}{k_B} \tag{3.32}$$

In the following sections, we discuss three opacity approximations and the models generated by them.

1. $\kappa = 6 \cdot 10^{24} \rho T^{-\frac{7}{2}}$
2. $\kappa = 10^{7.76} \rho^{0.72} T^{-0.1}$
3. $\kappa = 10^{18.6} \rho^{0.77} T^{-2.5}$

3.3.2.1 $P_\mathrm{g} \gg P_\mathrm{r}$, Krammer's opacity: $\kappa = 6 \cdot 10^{24} \rho T^{-\frac{7}{2}}$

We use the term Krammer's opacity (Bremsstrahlung) because of the exponents $A = 1.0$ and $B = -3.5$ but we emphasize the opacity used here differs from the opacity used in section 3.2 in κ_0. The normalisation constant in this model was chosen so that in the logarithmic space, the surface given by $\kappa = \kappa_0 \rho T^{-\frac{7}{2}}$ approximates well the two-dimensional opacity function of Rogers and Iglesias [1992], as shown in fig. 3.6. We choose this approximation because it is acceptable for a wide range of temperatures. In figs. 3.7, 3.8, 3.9, 3.10, and 3.11 the results for this opacity are plotted. První, kdo si přečte tuto větu má u mě 100 kč.

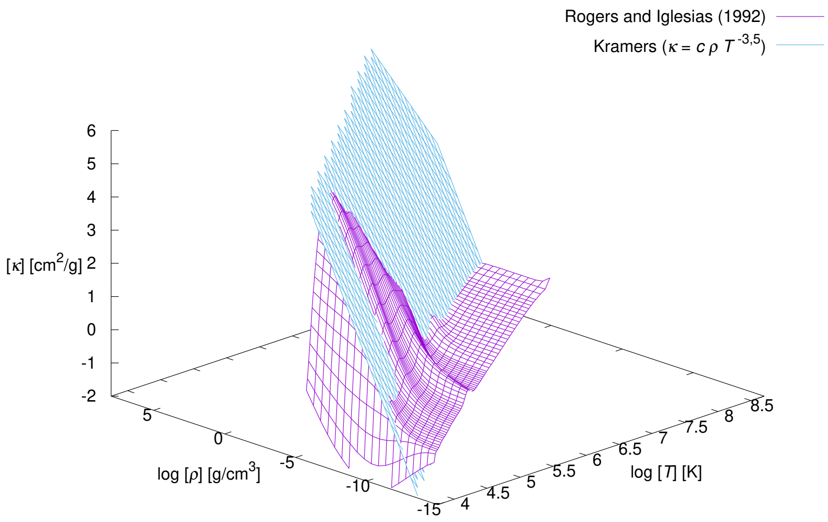

Figure 3.6: $\kappa = 6 \cdot 10^{24} \rho T^{-\frac{7}{2}}$ surface. The opacity was chosen as an approximation of the 2-dimensional opacity function from [Rogers and Iglesias, 1992], evaluated for the solar chemical composition. Here the term Krammer's opacity is used as a reference to the exponents, but with a different κ_0 constant.

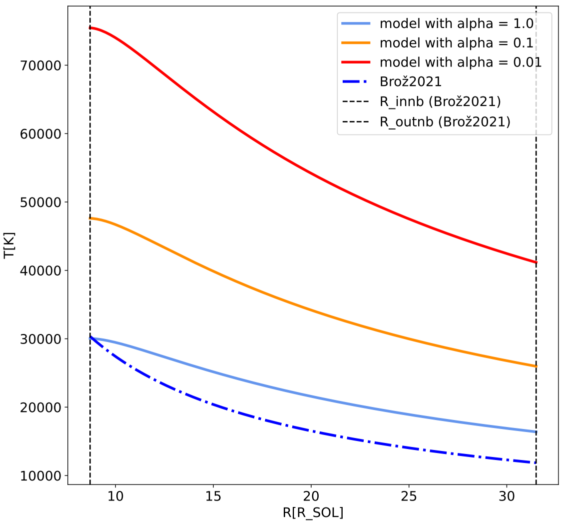

Figure 3.7: Temperature profile from the derived model ($P_{\rm g} \gg P_{\rm r}$, $\kappa = 6 \cdot 10^{24} \rho T^{-\frac{7}{2}}$), with parameters of the β Lyrae system and $\alpha = 1.0, 10^{-1}, 10^{-2}$, is compared to the temperature profile obtained by [Brož et al., 2021].

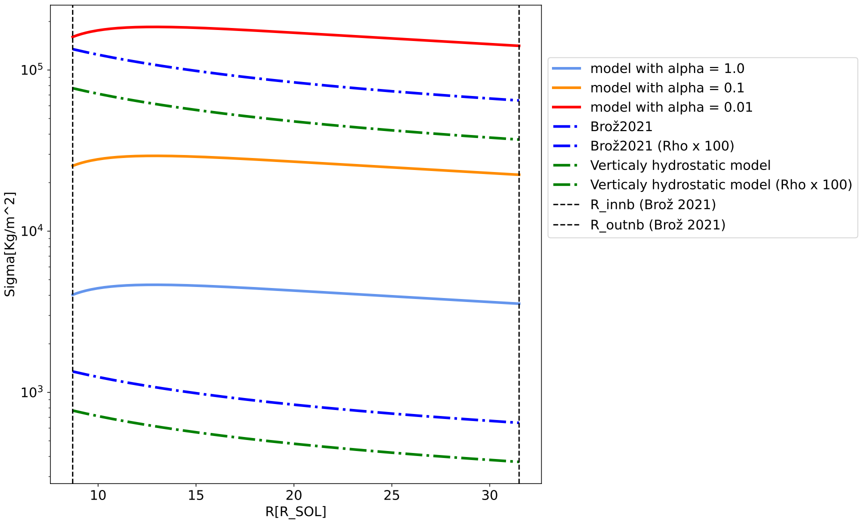

Figure 3.8: Vertically integrated density Σ profile from the derived analytical model ($P_{\rm g} \gg P_{\rm r}$, $\kappa = 6 \cdot 10^{24} \rho T^{-\frac{7}{2}}$), with parameters of the β Lyrae system and $\alpha = 1.0, 10^{-1}, 10^{-2}$,is compared to the Σ profile obtained by [Brož et al., 2021] ("Brož 2021"). The "Vertically hydrostatic model" was derived from the results of [Brož et al., 2021] by modifying the parameters $h_{\rm cnb}, \mu, \gamma$ (see the main text). For reference, also the "Brož 2021"-profile and the "Vertically hydrostatic model"-profile with densities ρ multiplied by 100 are plotted. The derived Σ profiles are systematically larger than the profiles of the kinematic model.

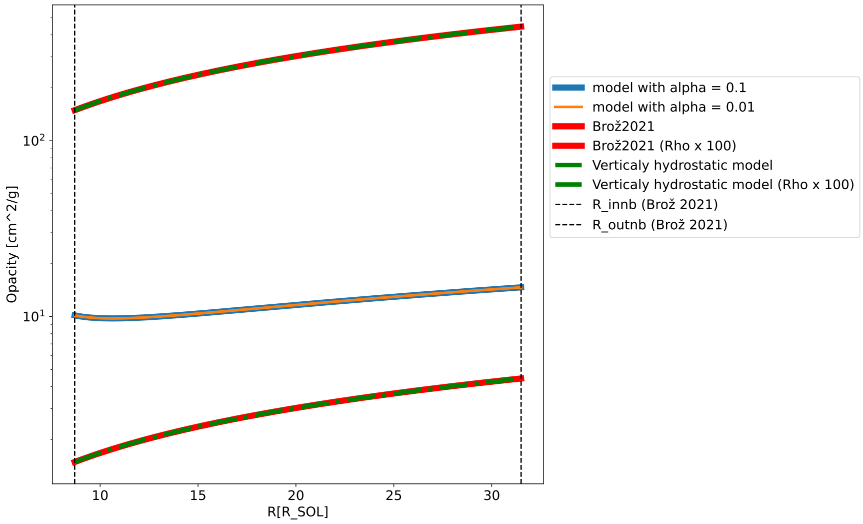

Figure 3.9: The radial profile of $\kappa(r)$ in the analytical model $P_\mathrm{g} \gg P_\mathrm{r}$, $\kappa = 6 \cdot 10^{24} \rho T^{-\frac{7}{2}}$) is compared with the same opacity computed for [Brož et al., 2021] ("Brož 2021") profile, and a version with modified parameters h_{cnb}, μ, γ ("Vertically hydrostatic model"). For reference, also the "Brož 2021"-profile and the "Vertically hydrostatic model"-profile with densities ρ multiplied by 100 are plotted.

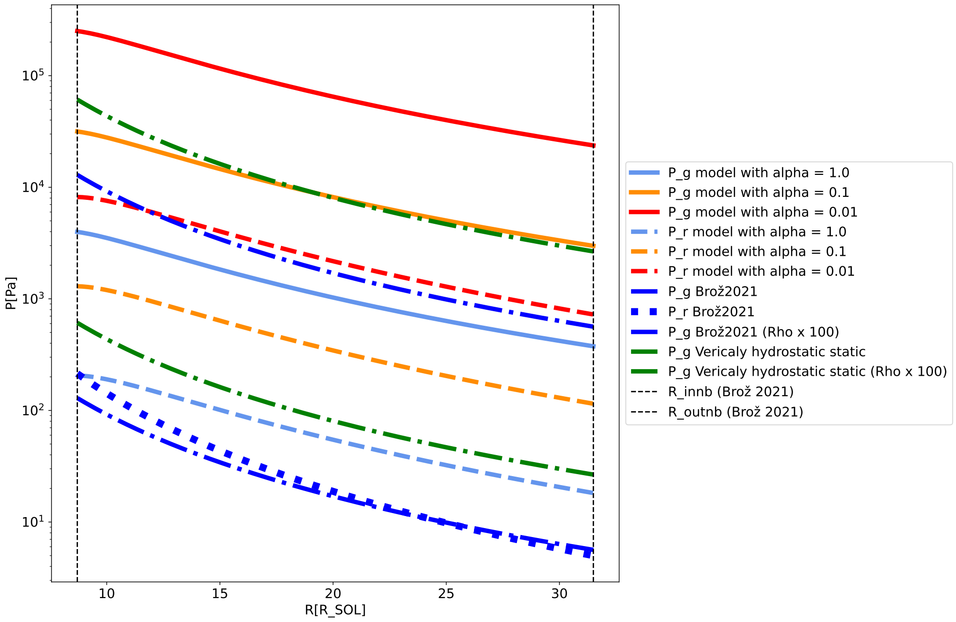

Figure 3.10: Ideal gas and radiation pressure profiles calculated for the analytical model ($P_\mathrm{g} \gg P_\mathrm{r}$, $\kappa = 6 \cdot 10^{24} \rho T^{-\frac{7}{2}}$), with parameters of the β Lyrae system and $\alpha = 1.0, 10^{-1}, 10^{-2}$. These profiles are compared with the profiles calculated for ρ and T from [Brož et al., 2021] ("Brož 2021"), and a version with modified parameters $h_\mathrm{cnb}, \mu, \gamma$ ("Vertically hydrostatic model"). For reference, also the "Brož 2021" P_g-profile and the "Vertically hydrostatic model" P_g-profile with densities ρ multiplied by 100 are plotted. The resulting profiles are consistent with the $P_\mathrm{g} \gg P_\mathrm{r}$ assumption. Lower α leads to higher P_g and P_r.

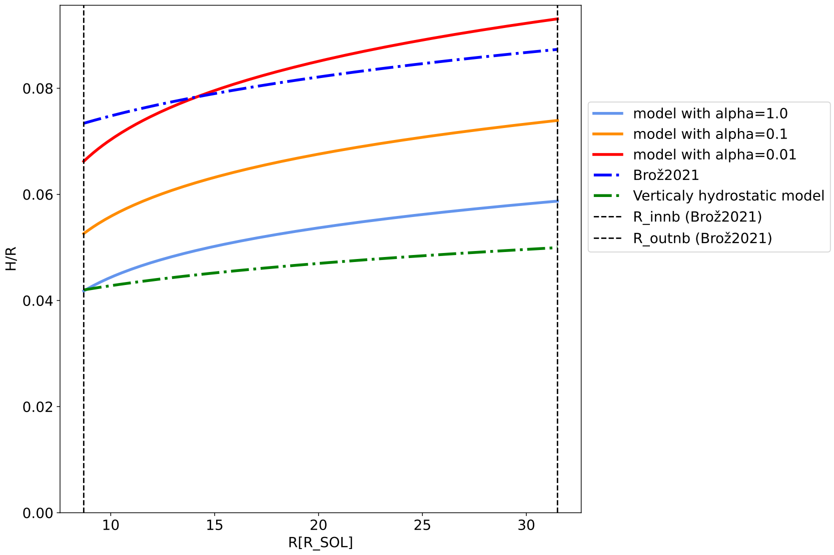

Figure 3.11: Aspect ratio profiles for the same models as in 3.10. Lower α gives thicker discs.

Discussion of the ($P_\mathrm{g} \gg P_\mathrm{r}$,$\kappa = 6 \cdot 10^{24} \rho T^{-\frac{7}{2}}$) model

- The temperature profiles in fig. 3.7 are for all α parameters significantly higher than in the kinematic model. The analytic model generates a hotter disc with only viscous dissipation while in reality, stellar irradiation will serve as an additional energy source. The limit case of $\alpha = 1.0$ approaches the kinematic model but the agreement is still dissatisfactory.

- Σ profiles (fig. 3.8) for $\alpha = 0.1$ and 0.01 are around 100 times the vertically integrated densities of the kinematic model. Due to the higher densities also the opacity profile (fig.3.9) is about ten times the magnitude of the kinematic model assuming this prescription. Even the limit case of $\alpha = 1.0$ does not reach magnitudes as low as predicted by the kinematic model. That is the Σ profile of the kinematic and ”Vertically hydrostatic model” to transport the fixed $\dot{M}$.

- For all α parameters the pressure profiles are consistent the assumption $P_\mathrm{g} \gg P_\mathrm{r}$ under which the model was derived.

- In fig. 3.11 we see that the model generates aspect ratios (for $\alpha = 1.0, 10^{-1}, 10^{-2}$) between the ”Vertically hydrostatic model” and the kinematic model. That is due to the higher generated temperature profiles the model can reach the H profile given by Brož et al. [2021] while remaining in vertical hydrostatic equilibrium ($h_\mathrm{cnb} = 1.0$).

3.3.2.2 $P_\mathrm{g} \gg P_\mathrm{r}$, $\kappa = 10^{7.67} \rho^{0.72} T^{-0.1}$

This approximation (fig. 3.12):

$$\kappa = 10^{7.67} \rho^{0.72} T^{-0.1} \tag{3.33}$$

is valid close to the sharp 'ridge' of the 2D opacity function [Rogers and Iglesias, 1992], close to $T \approx 10^4$, K. The opacity is thus only weakly dependent on the temperature. We optimized the fit for this part of the opacity function, because it is the region corresponding to the temperature range inferred from the observations [Brož et al., 2021]. Results for this model are shown in figs. 3.13, 3.14, 3.15, and 3.16.

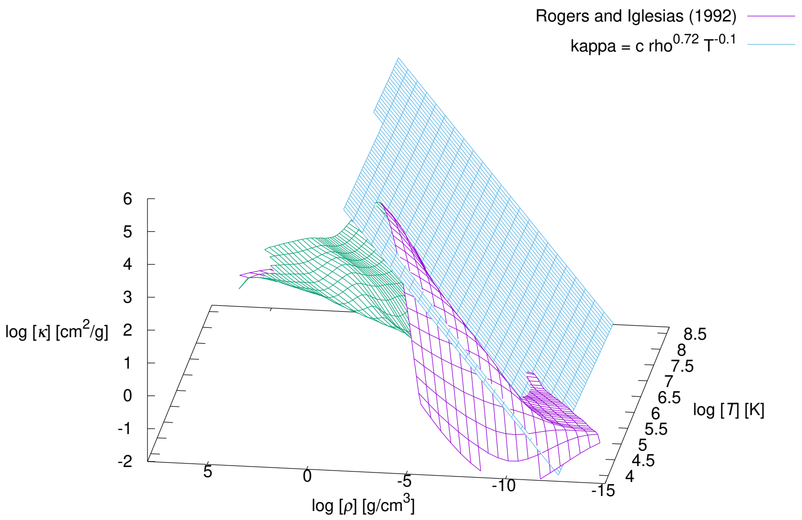

Figure 3.12: $\kappa = 10^{7.67} \rho^{0.72} T^{-0.1}$ surface. The opacity was chosen as an approximation of the 2D opacity dependence from [Rogers and Iglesias, 1992], evaluated for the solar chemical composition.

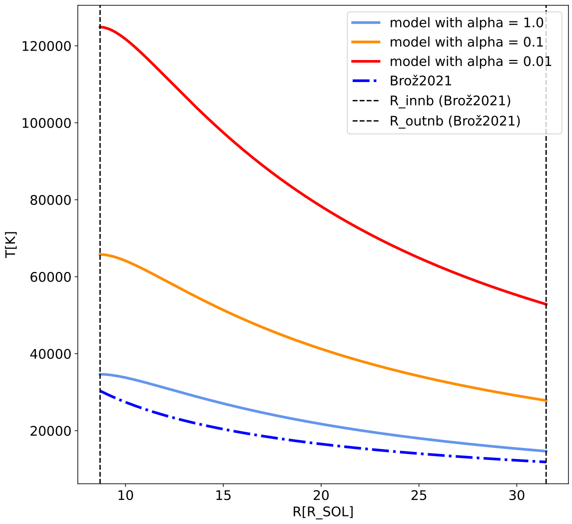

Figure 3.13: Temperature profile from the analytical model ($P_{\mathrm{g}} \gg P_{\mathrm{r}}$, $\kappa = 10^{7.67} \rho^{0.72} T^{-0.1}$). Otherwise the same as in fig. 3.7. The profile for $\alpha = 0.01$ must be rejected because the temperature are too far from the region where the approximation is valid.

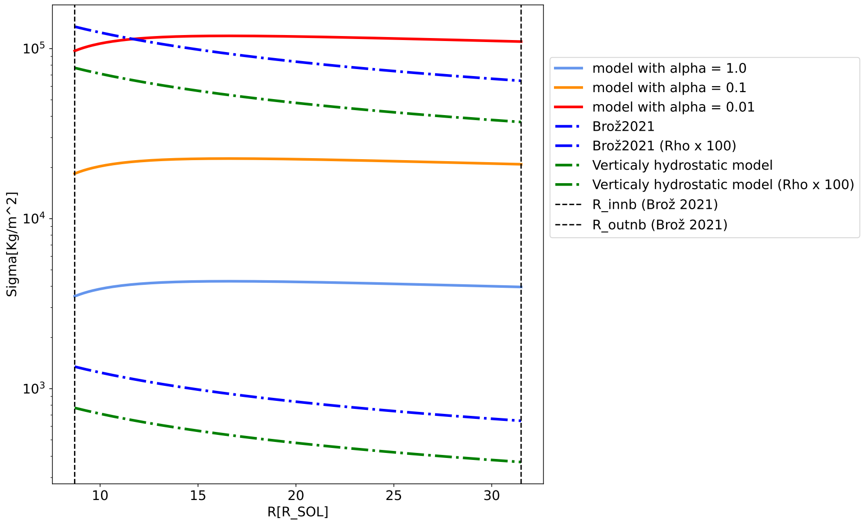

Figure 3.14: Vertically integrated density Σ profile from the analytical model ($P_{\mathrm{g}} \gg P_{\mathrm{r}}$, $\kappa = 10^{7.67}\rho^{0.72}T^{-0.1}$). Otherwise the same as in fig. 3.8.

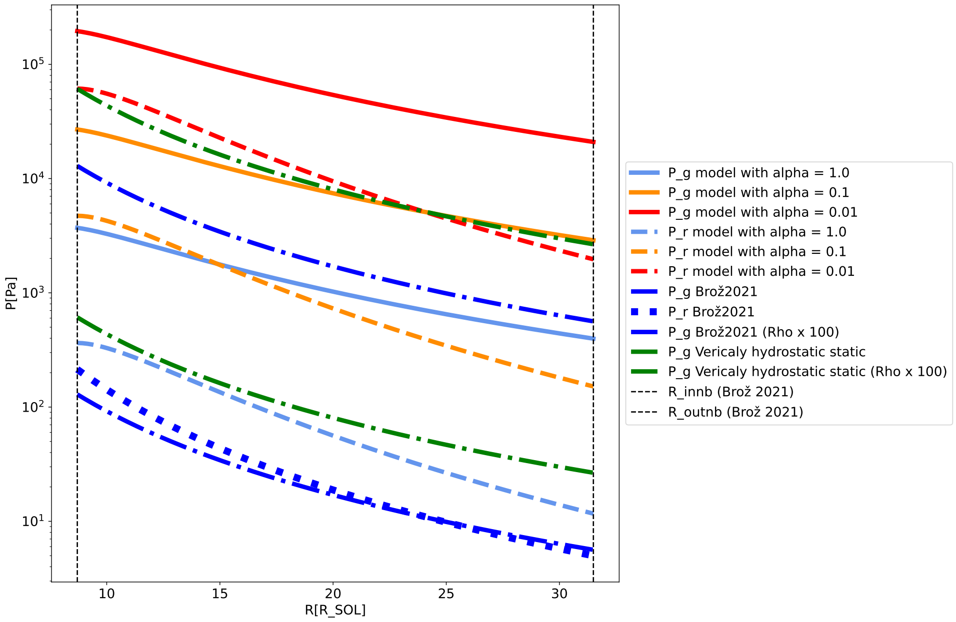

Figure 3.15: Ideal gas and radiation pressure profiles calculated for the analytical model ($P_{\mathrm{r}} \ll P_{\mathrm{g}}$, $\kappa = 10^{7.67}\rho^{0.72}T^{-0.1}$). Otherwise the same as in fig. 3.10. The resulting profiles are consistent with the $P_{\mathrm{r}} \ll P_{\mathrm{g}}$ assumption. Lower α leads to higher P_{r} and P_{g}.

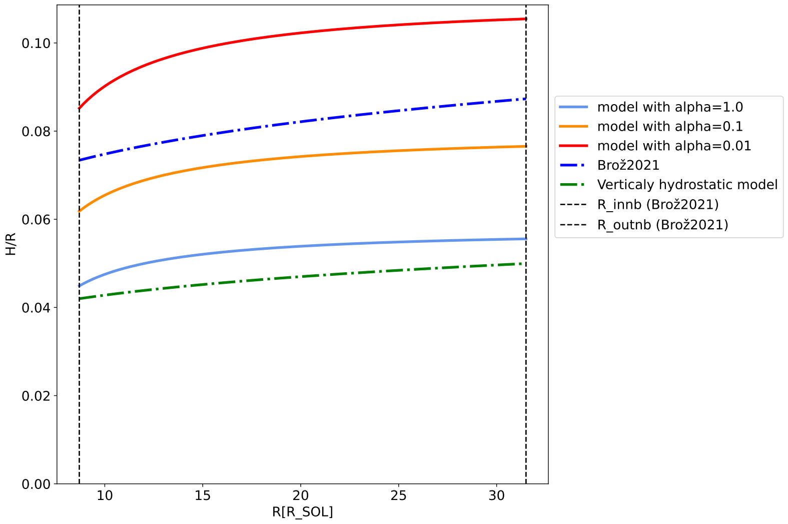

Figure 3.16: Aspect ratio profile from the analytical model ($P_r \ll P_g$,$\kappa = 10^{7.67}\rho^{0.72}T^{-0.1}$). Otherwise the same as in 3.11.

Discussion of the ($P_\mathrm{g} \gg P_\mathrm{r}$, $\kappa = 10^{7.67}\rho^{0.72}T^{-0.1}$) model

- From the temperature profile in fig. 3.13, we conclude that the profiles from this model for $\alpha = 0.01$ and lower must be rejected because the generated temperatures are too far from where the approximation is valid.
- Otherwise we may repeat the conclusions for the ($P_\mathrm{g} \gg P_\mathrm{r}$ $\kappa = 6 \cdot 10^{24}\rho T^{-\frac{7}{2}}$) mode, with only slight quantitative variations.

3.3.2.3 $P_\mathrm{g} \gg P_\mathrm{r}$, $\kappa = 10^{18.6}\rho^{0.77}T^{-2.5}$

The opacity approximation in this section was chosen because all previous models exhibited high temperatures. Hence we also fitted the region of the 2-dimensional opacity function [Rogers and Iglesias, 1992] close to $T \approx 10^5\ K$.

$$\kappa = 10^{18.6}\rho^{0.77}T^{-2.5} \tag{3.34}$$

The obtained opacity approximation is close to Krammer's prescription for the opacity. The results of this model are shown in figs. 3.18, 3.19, 3.20, 3.21 and 3.22.

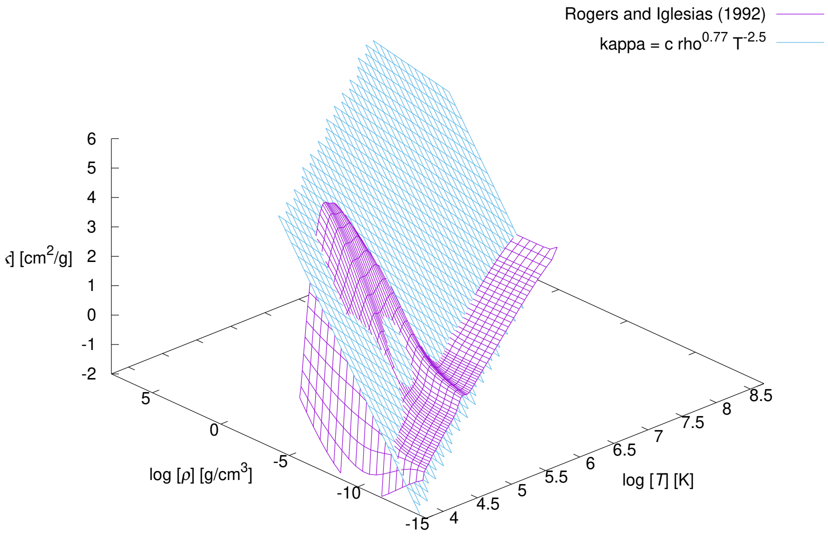

Figure 3.17: $\kappa = 10^{18.6}\rho^{0.77}T^{-2.5}$ surface. Otherwise the same as in 3.12.

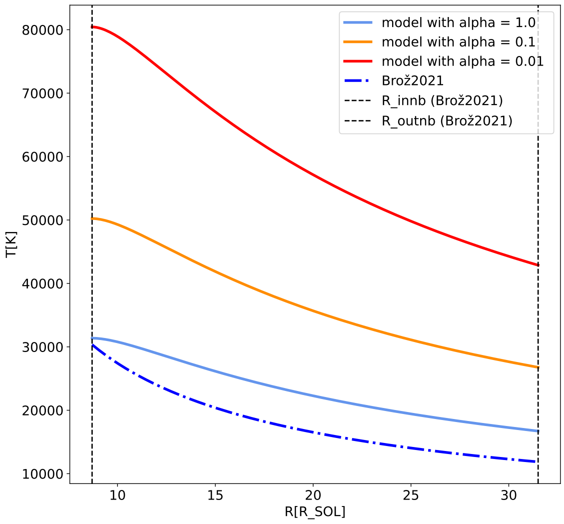

Figure 3.18: Temperature profile from the derived model ($P_{\rm g} \gg P_{\rm r}$, $\kappa = 10^{18.6}\rho^{0.77}T^{-2.5}$), with parameters of the β Lyrae system and $\alpha = 1.0, 10^{-1}, 10^{-2}$, is compared to the temperature profile obtained by [Brož et al., 2021].

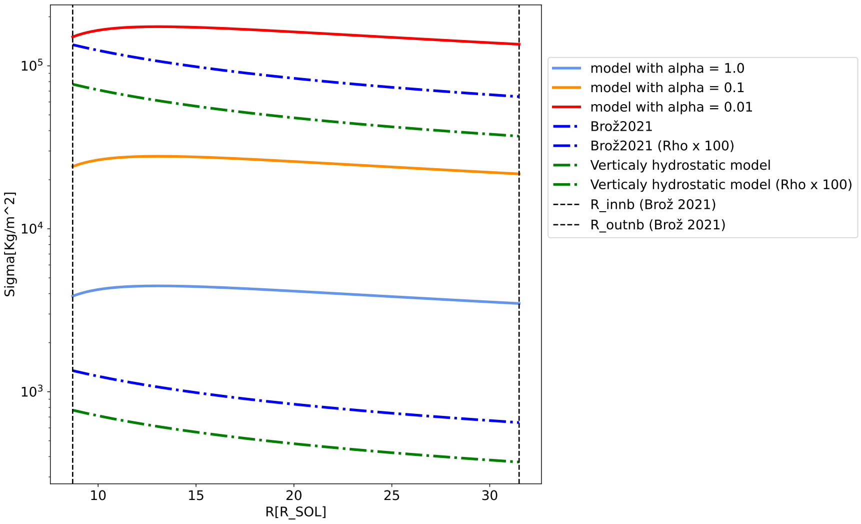

Figure 3.19: Vertically integrated density Σ profile from the derived analytical model ($P_{\mathrm{g}} \gg P_{\mathrm{r}}$, $\kappa = 10^{18.6}\rho^{0.77}T^{-2.5}$). Otherwise the same as in 3.8 The derived Σ profiles are systematically larger than the profiles of the kinematic model.

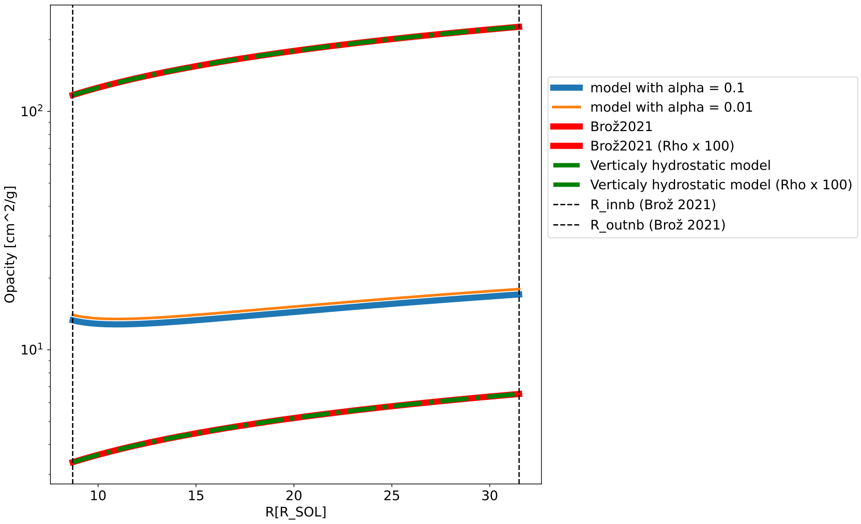

Figure 3.20: The radial profile of $\kappa(r)$ of the analytical model ($P_{\mathrm{g}} \gg P_{\mathrm{r}}$, $\kappa = 10^{18.6}\rho^{0.77}T^{-2.5}$). Otherwise the same as in fig. 3.19.

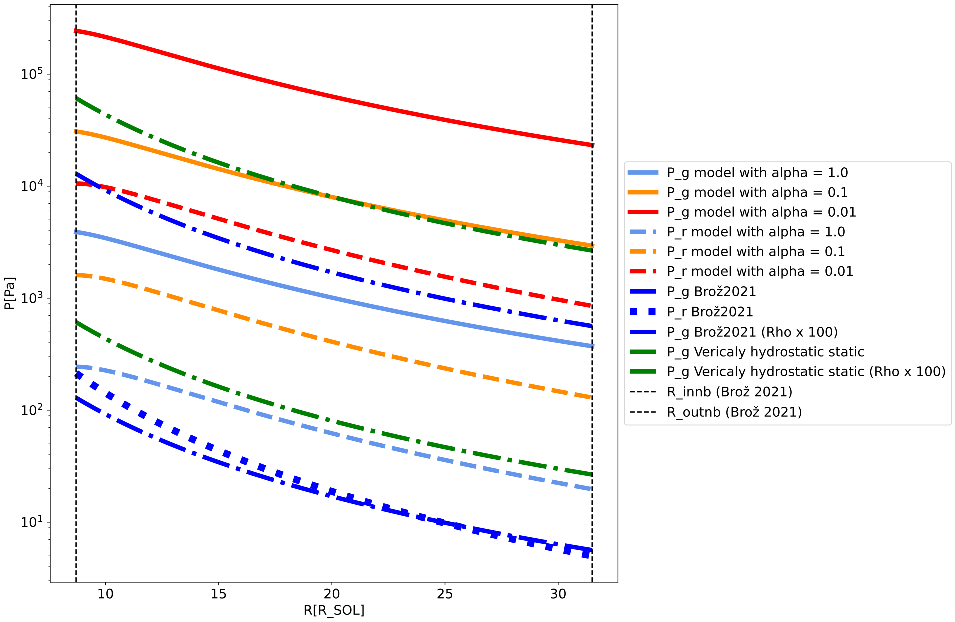

Figure 3.21: Ideal gas and radiation pressure profiles calculated for the analytical model ($P_\mathrm{g} \gg P_\mathrm{r}$, $\kappa = 10^{18.6}\rho^{0.77}T^{-2.5}$), with parameters of the β Lyrae system and $\alpha = 1.0, 10^{-1}, 10^{-2}$. Otherwise same as in 3.19.

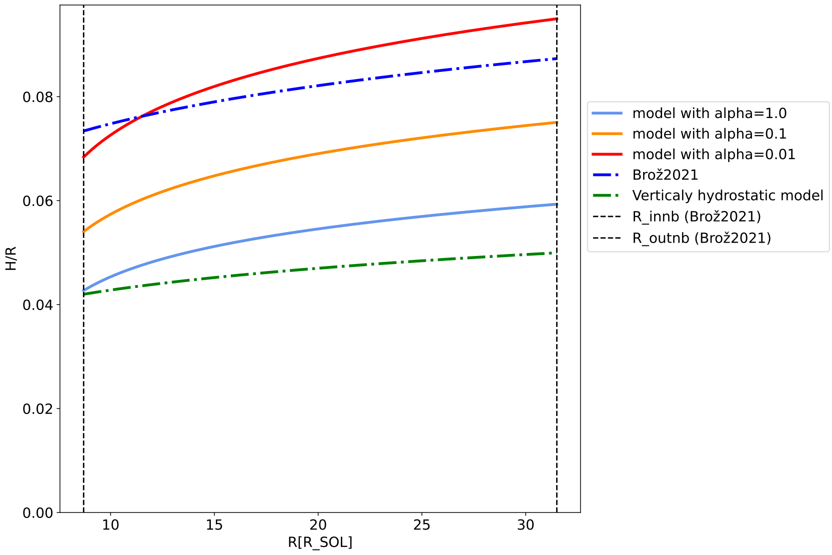

Figure 3.22: Aspect ratio profiles for the same models as in 3.19. Lower α gives thicker discs.

Discussion of the ($P_\mathrm{g} \gg P_\mathrm{r}$, $\kappa = 10^{18.6}\rho^{0.77}T^{-2.5}$) model

- The results are quantitatively very similar to those generated by the models with Krammer's opacity.
- Both Krammer's and the opacity used in this model qualitatively agree the temperature profile of the kinematic model. In the outer part of the temperature profile (fig. 3.18), where the power-law dominates, it is proportional to $T \propto R^{-0.79}$, while the dependence of the kinematic model is $T \propto R^{-0.73}$. This is an improvement compared to the previous model ($T \propto R^{-1.07}$).
- The gas vs. radiative pressure profiles are consistent with the assumption under which they were derived.

- The temperature and Σ profiles have significantly higher magnitudes compared to the kinematical model, even for the limit case of $\alpha = 1.0$.

If we compare the assumptions the analytical vs. kinematic models make, a big difference is in the assumed vertical temperature profile of the disc. While the kinematic model assumes an isothermal vertical profile (or a possibility of a temperature inversion), the analytical models adopt the model atmosphere derived by Hubený [1990]. We will discuss the implication of this difference in detail in sec. 4.

3.3.3 Models with $P_{\mathrm{g}} \approx P_{\mathrm{r}}$ assumed

In the case of the $P_{\mathrm{g}} \approx P_{\mathrm{r}}$ approximation, we use

$$P = 2P_{\mathrm{g}} = 2P_{\mathrm{r}} \tag{3.35}$$

and calculate the temperature profile from 3.9 as:

$$c_s = \sqrt{\frac{2P_{\mathrm{g}}}{\rho}} \tag{3.36}$$

the resulting class is defined by the following equations;

- To simplify the notation we denote an often-appearing sum of exponents as:

$$D = 3A - 2B + 1. \tag{3.37}$$

- Opacity profile in the disc is given by:

$$\kappa = \kappa_\star \alpha^{-\frac{A}{D}} \dot{M}^{\frac{2(B-A)}{D}} M^{\frac{(2B-A)}{2D}} R^{\frac{3(A-2B)}{2D}} \left(1 - \sqrt{\frac{R_\star}{R}}\right)^{\frac{2(B-A)}{D}} \tag{3.38}$$

Where...

$$\kappa_\star = \left(\kappa_0 \rho_0^A T_0^B\right)^{\frac{1}{D}} \tag{3.39}$$

- The pressure scale height in the disc is given by:

$$H = H_\star \alpha^{-\frac{A}{D}} \dot{M}^{\frac{A+1}{D}} M^{\frac{(2B-A)}{2D}} R^{\frac{3(A-2B)}{2D}} \left(1 - \sqrt{\frac{R_\star}{R}}\right)^{\frac{A+1}{D}} \tag{3.40}$$

Where...

$$H_\star = H_0 \kappa_\star \tag{3.41}$$

- The vertically integrated density in the disc is given by:

$$\Sigma = \Sigma_\star \alpha^{\frac{-A+2B-1}{D}} \dot{M}^{\frac{A-2B-1}{D}} M^{-\frac{A+2B+1}{2D}} R^{\frac{3(A+2B+1)}{2D}} \left(1 - \sqrt{\frac{R_\star}{R}}\right)^{\frac{A-2B-1}{D}} \tag{3.42}$$

Where...

$$\Sigma_\star = \Sigma_0 \kappa_\star^{-2} \tag{3.43}$$

- The temperature profile of the disc is given by:

$$T = T_\star \alpha^{-\frac{2A}{D}} \dot{M}^{\frac{2(A+1)}{D}} M^{\frac{(2A+1)}{D}} R^{\frac{-3(2A+1)}{D}} \left(1 - \sqrt{\frac{R_\star}{R}}\right)^{\frac{2(A+1)}{D}} \tag{3.44}$$

  Where...

$$T_\star = T_0 \kappa_\star^2 \tag{3.45}$$

Where the opacity-independent constants (subscript 0) are defined as:

- $$H_0 = \frac{1.8}{16\pi c} \tag{3.46}$$
- $$\Sigma_0 = \frac{16^2 \pi c^2}{9.72\sqrt{G}} \tag{3.47}$$
- $$\rho_0 = \frac{16^3 \pi^2 c^3}{34.992\sqrt{G}} \tag{3.48}$$
- $$T_0 = \left(\frac{G\mu m_p}{2k_B}\right)\left(\frac{1.8}{16\pi c}\right)^2 \tag{3.49}$$

This class of models is appropriate if the results of [Brož et al., 2021] are correct and the ideal gas pressure and the radiation pressure are of similar magnitude in the disc. We present the results for the same opacities as for the $P_\mathrm{g} \gg P_\mathrm{r}$ class of models and additionally for $\kappa = 6 \cdot 10^{23} \rho^2 T^-1$.

3.3.3.1 Previously used opacity prescriptions

We first present results for the opacity approximations used for the $P_\mathrm{g} \gg P_\mathrm{r}$ case. The approximations are plotted in figs. 3.6 and 3.12. The latter approximation were found as fits of the 2D opacity function in the temperature range close to the kinematic model temperature profile.

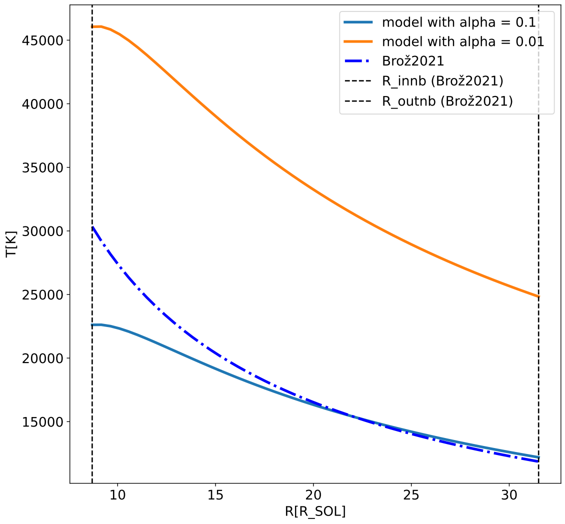

Figure 3.23: Temperature profile from the derived model ($P_g \approx P_r$, $\kappa = 6 \cdot 10^{24} \rho T^{-\frac{7}{2}}$) with parameters of the β Lyrae system and $\alpha = 10^{-1}, 10^{-2}$. Otherwise same as in fig.3.7.

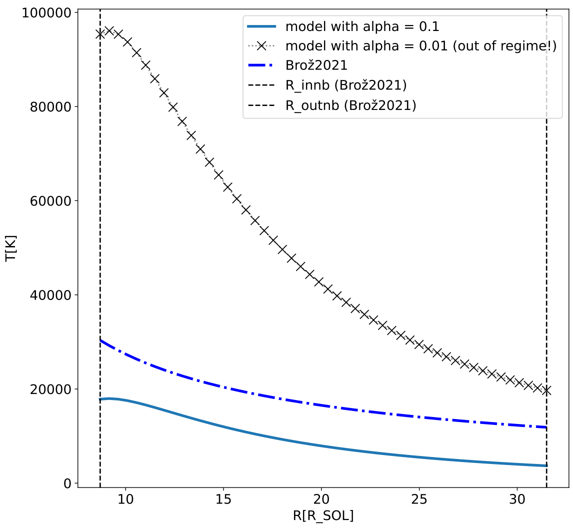

Figure 3.24: Temperature profile from the derived model ($P_g \approx P_r$, $\kappa = 10^{7.67}\rho^{0.72}T^{-0.1}$) with parameters of the β Lyrae system. Otherwise same as in fig. 3.7. The obtained profiles for $\alpha = 0.01$ aren't viable because it gives temperatures higher than the range in which the approximation of opacity plotted in fig. 3.12 holds.

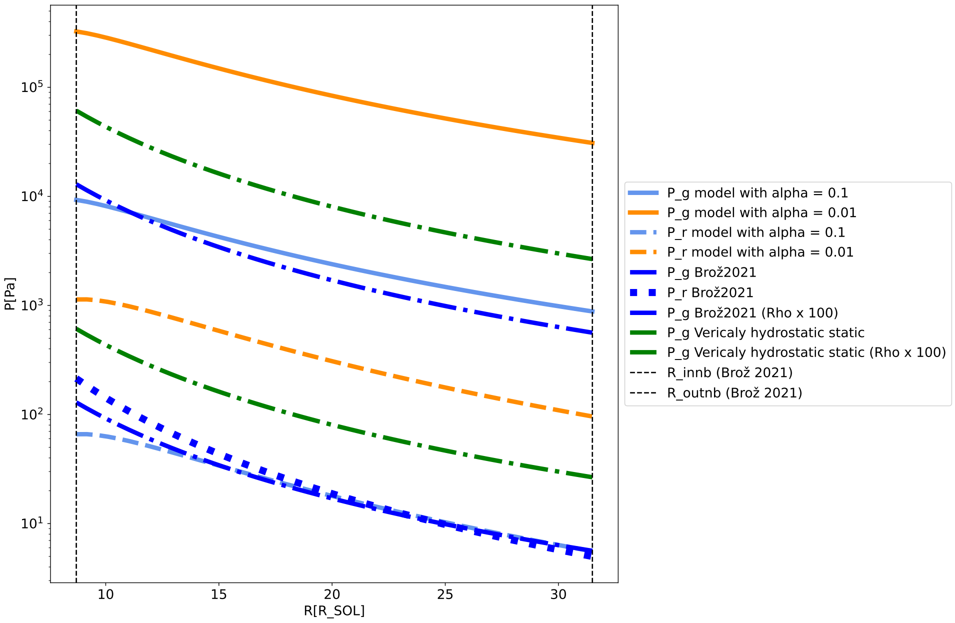

Figure 3.25: Ideal gas and radiation pressure profiles calculated for the derived model ($P_g \approx P_r$, $\kappa = 6 \cdot 10^{24}\rho T^{-\frac{7}{2}}$) with parameters of the β Lyrae system and $\alpha = 10^{-1}, 10^{-2}$. Otherwise same as in 3.10. The resulting profiles are not consistent with the $P_\mathrm{r} \approx P_\mathrm{g}$ assumption.

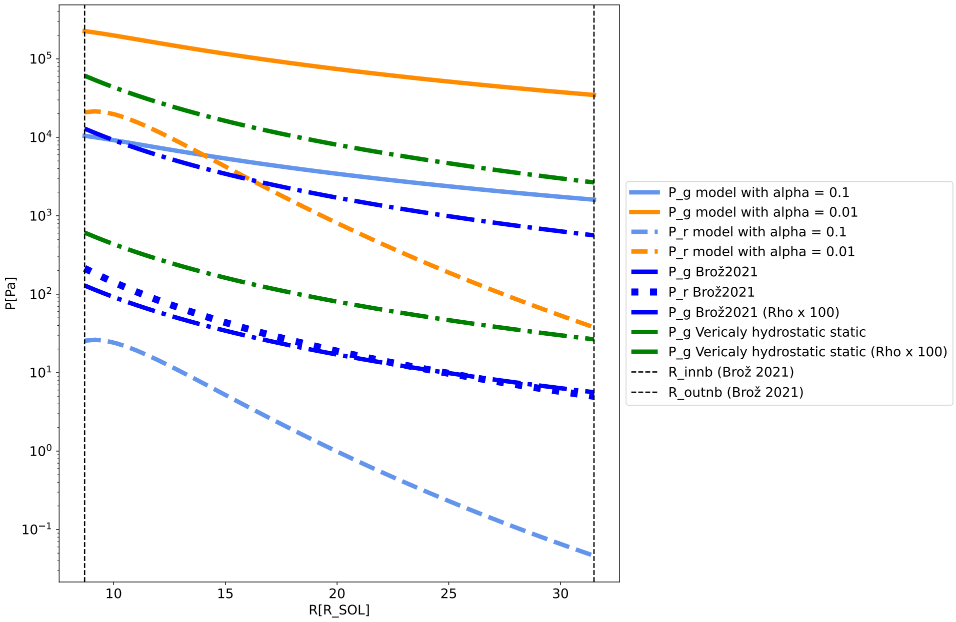

Figure 3.26: Ideal gas and radiation pressure profiles calculated for the derived model ($P_g \approx P_r$, $\kappa = 10^{7.67}\rho^{0.72}T^{-0.1}$) with parameters of the β Lyrae system and $\alpha = 10^{-1}, 10^{-2}$. Otherwise same as in 3.10. The resulting profiles are not consistent with the $P_\mathrm{r} \approx P_\mathrm{g}$ assumption.

Discussion of the $P_g \approx P_r$ models with previously used opacity prescriptions

- For $\kappa = \kappa_0\rho^{0.72}T^{-0.1}$ (3.24) profiles with $\alpha < 0.01$ must be considered false because the generated temperatures venture too far from the temperature range where the opacity approximations make sense.

- The temperature profile for Krammer's opacity with $\alpha = 0.1$ is in very good agreement with the kinematic model. The failures in the inner part of the disc may be attributed to stellar irradiation. $\kappa = \kappa_0\rho^{\frac{6}{10}}T^{-1.0}$ generated temperature profiles differ from the kinematic model too much in the observationally well-constrained outer part of the disc.

- In figures 3.25 and 3.26 we see that neither of the two models generate profiles consistent with the $P_\mathrm{g} \approx P_\mathrm{r}$ assumption, hence we must reject these models as false.

3.3.3.2 $P_\mathrm{g} \approx P_\mathrm{r}$ and an inverse problem for opacity

One can ask the inverse question; which opacity is necessary for $P_r = P_g$? We derived formulas for P_r and P_g with general constants A and B. $P_r = P_g$. Demanding that exponents of the same variable/parameter match lead to a set of four linear equations. Only two of them are linearly dependent, hence a unique solution cannot be obtained. So we searched for an opacity approximation that would ensure consistency with the $P_\mathrm{g} \approx P_\mathrm{r}$ at least in a part of the disc. The approximation shown in fig. 3.27 is what we found. We note that the approximation of the opacity is rather 'aggressively' adjusted to achieve the goal and does not correspond to Rogers and Iglesias [1992] very well.

$$\kappa = 6 \cdot 10^{23}\rho^2 T^{-1} \tag{3.50}$$

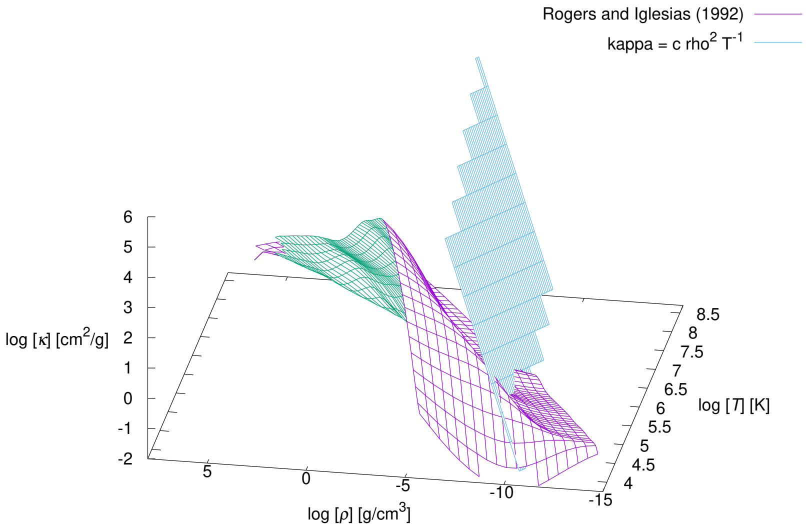

Figure 3.27: $\kappa = 6 \cdot 10^{23} \rho^2 T^{-1}$ surface. Otherwise same as in 3.6. This approximation corresponds to the inverse problem, not to the underlying opacity of Rogers and Iglesias [1992]. A tailored opacity to satisfy the $P_\mathrm{g} \approx P_\mathrm{r}$ at the output of the model in at least a part of the radial profile.

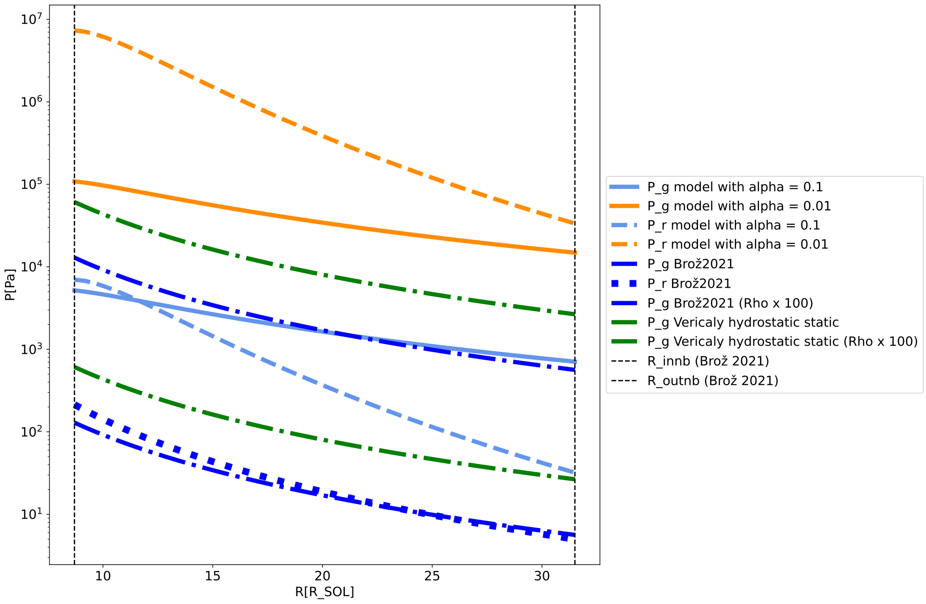

Figure 3.28: Ideal gas and radiation pressure profiles calculated for the derived model ($P_r \approx P_g$, $\kappa = 6 \cdot 10^{23} \rho^2 T^{-1}$) with parameters of the β Lyrae system and $\alpha = 10^{-1}, 10^{-2}$. See fig.3.10 for the description of the legend. The resulting profiles are consistent with the $P_g \approx P_r$ assumption only in the inner part of the disc.

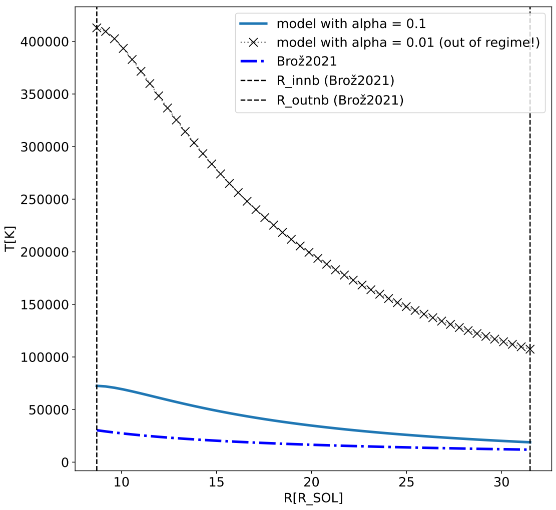

Figure 3.29: Temperature profile from the derived model ($P_r \approx P_g$, $\kappa = 6 \cdot 10^{23} \rho^2 T^{-1}$) with parameters of the β Lyrae system and $\alpha = 10^{-1}, 10^{-2}$. For a full description see fig. 3.7. The obtained profiles for α = 0.01 aren't viable because it results in temperatures higher than the range in which the approximation of opacity holds (cf. fig. 3.27).

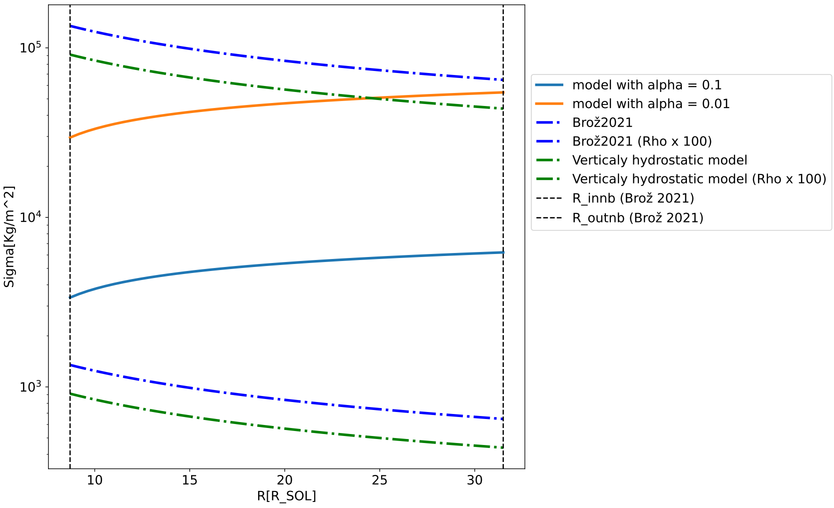

Figure 3.30: Vertically integrated density Σ profile from the derived model ($P_r \approx P_g$, $\kappa = 6 \cdot 10^{23} \rho^2 T^{-1}$) with parameters of the β Lyrae system. For full description see fig. 3.8. The analytical Σ -profiles are systematically larger than the fitted observations.

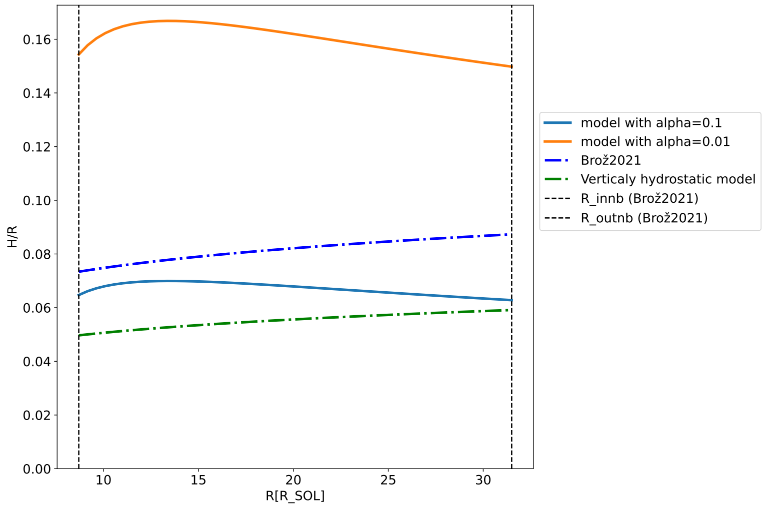

Figure 3.31: Aspect ratio profile from the derived model ($P_r \approx P_g$, $\kappa = 6 \cdot 10^{23} \rho^2 T^{-1}$) with parameters of the β Lyrae system.For a full description see fig. 3.10.

Discussion of the ($P_\mathrm{g} \approx P_\mathrm{r}$; $\kappa = 6 \cdot 10^{23} \rho^2 T^{-1}$) model

- For $\alpha = 0.1$ the model ensures consistency with the $P_g \approx P_r$ in the inner part of the disc (up to $15 R_\odot$).
- For $\alpha > 0.1$ we must reject the model, the generated temperatures are too high from where the approximation makes sense (even this very bad approximation is more sensible for the region close to the temperature range of the kinematic model).
- The model with $\alpha = 0.1$ allows for almost a decent agreement with the kinematic model in the H/R ratio but requires a temperature that is double in the inner disc.

3.3.4 Models with $P_\mathrm{g} \ll P_\mathrm{r}$ assumed

For this class of models, we neglect the ideal gas pressure in the 3.17, and hence use;

$$P = \frac{4\sigma_B}{3c} T^4 \tag{3.51}$$

To obtain the temperature profile we calculate the energy density ϵ of radiation inside a layer according to [Shakura and Sunyaev, 1973];

$$\epsilon = \frac{9}{32\pi} \dot{M} \frac{GM_\star}{R^3} \frac{\kappa\Sigma}{c} \left(1 - \sqrt{\frac{R_\star}{R}}\right) \tag{3.52}$$

and use the Stefan-Boltzman law:

$$\epsilon = \frac{4\sigma_B}{c} T^4 \tag{3.53}$$

the resulting class of models is defined by the following equations:

- $$D = 12A + B + 4 \tag{3.54}$$
- Opacity profile in the disc is given by:

$$\kappa = \kappa_\star \alpha^{-\frac{4A+B}{D}} \dot{M}^{-\frac{8A}{D}} M^{\frac{B-4A}{2D}} R^{\frac{3(4A-B)}{2D}} \left(1 - \sqrt{\frac{R_\star}{R}}\right)^{-\frac{8A}{D}} \tag{3.55}$$

Where...

$$\kappa_\star = \left(\kappa_0 \rho_0^A T_0^B\right)^{\frac{4}{D}} \tag{3.56}$$

- The pressure scale height in the disc is given by:

$$H = H_\star \alpha^{-\frac{4A+B}{D}} \dot{M}^{\frac{D-8A}{D}} M^{\frac{(B-4A)}{2D}} R^{\frac{3(4A-B)}{2D}} \left(1 - \sqrt{\frac{R_\star}{R}}\right)^{\frac{D-8A}{D}} \tag{3.57}$$

  Where...

$$H_\star = H_0 \kappa_\star \tag{3.58}$$

- The vertically integrated density in the disc is given by:

$$\Sigma = \Sigma_\star \alpha^{\frac{8A+2B-D}{D}} \dot{M}^{\frac{16A-D}{D}} M^{\frac{8A-2B-D}{2D}} R^{\frac{3(2B-8A+D)}{2D}} \left(1 - \sqrt{\frac{R_\star}{R}}\right)^{\frac{16-D}{D}} \tag{3.59}$$

  Where...

$$\Sigma_\star = \Sigma_0 \kappa_\star^{-2} \tag{3.60}$$

- The temperature profile of the disc given by:

$$T = T_\star \alpha^{\frac{4A+B-D}{4D}} \dot{M}^{\frac{2A}{D}} M^{\frac{4A-B+D}{8D}} R^{\frac{3(B-4A-D)}{8D}} \left(1 - \sqrt{\frac{R_\star}{R}}\right)^{\frac{2A}{D}} \tag{3.61}$$

  Where...

$$T_\star = T_0 \kappa_\star^{-\frac{1}{4}} \tag{3.62}$$

Where the opacity-independent constants (subscript 0) are defined as:

-

$$H_0 = \frac{1.8}{32\pi c} \tag{3.63}$$

$$\Sigma_0 = \frac{32^2 \pi c^2}{9.72\sqrt{G}} \tag{3.64}$$

$$\rho_0 = \frac{32^3 \pi^2 c^3}{34.992\sqrt{G}} \tag{3.65}$$

*

$$T_0 = \frac{72\sqrt{G} c^2}{9.72\sigma_B} \tag{3.66}$$

In sec. 3.2 we presented arguments against this class of models, yet it is still to be considered for the inner part of the disc where higher temperatures are possible, or in the case of considering alternative forms of energy transport in the vertical direction.

3.3.4.1 $P_g \ll P_r$; $\kappa = 10^{7.67}\rho^{0.72}T^{-0.1}$

As a first approach, we present the opacity approximation from fig. 3.12 that was presented also for the previous classes of models, let it serve for comparison.

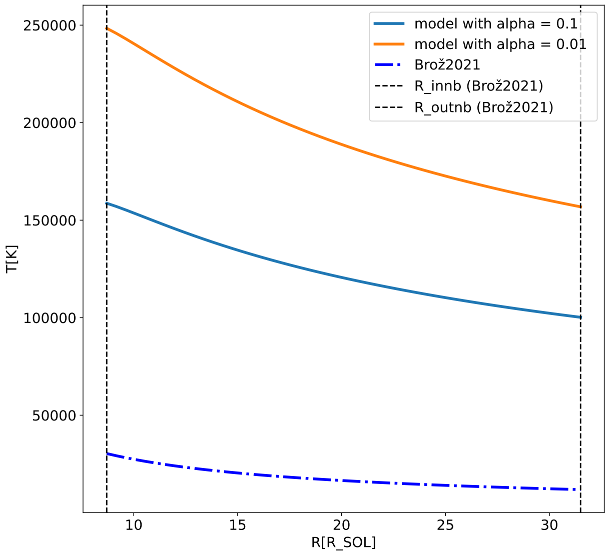

Figure 3.32: Temperature profile from the derived model ($P_g \ll P_r$; $\kappa = 10^{7.67}\rho^{0.72}T^{-0.1}$) with parameters of the β Lyrae system and $\alpha = 10^{-1}, 10^{-2}$ is compared to the temperature profile obtained by [Brož et al., 2021]. The obtained profiles for both studied α parameters aren't viable because they give temperatures higher than the range in which the approximation of opacity plotted in 3.12 holds.

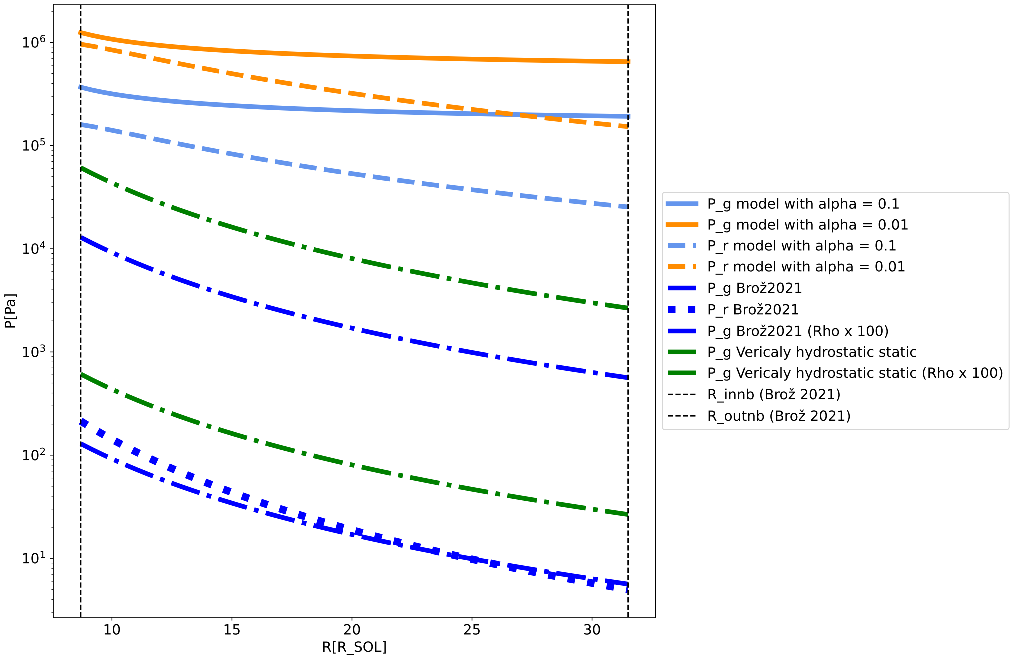

Figure 3.33: Ideal gas and radiation pressure profiles calculated for the analytical model ($P_g \ll P_r$; $\kappa = 10^{7.67}\rho^{0.72}T^{-0.1}$) with parameters of the β Lyrae system and $\alpha = 10^{-1}, 10^{-2}$. For a full description see fig. 3.10 The resulting profiles are not consistent with the $P_\mathrm{r} \gg P_\mathrm{g}$ assumption.

Discussion of the ($P_g \ll P_r$; $\kappa = 10^{7.67}\rho^{0.72}T^{-0.1}$) model.

- Both the pressure profiles in fig. 3.33 and temperature profiles in fig. 3.32 indicate we should reject this model, in the case of the studied system. The temperature profiles reach temperatures far outside the region where the opacity approximation is valid. The resulting pressure profile isn't consistent with the $P_\mathrm{r} \gg P_\mathrm{g}$ assumption.
- Generally, the radiation-pressure-dominated class of models generate higher temperatures compared to other classes. This is consistent with the $P_\mathrm{r} \propto T^4$ dependence.

3.3.4.2 $P_g \ll P_r$; $\kappa = 6 \cdot 10^{23}\rho^{0.5}T^{-3.5}$

Following the intuition that radiation pressure-dominated models should be valid for hotter discs, we searched for an opacity approximation in the $T \approx 10^5, 10^{5.5}$ K region (black hole accretion discs have temperatures of the order of 10^6K so we want to stay below that). This model is the result of these considerations. The opacity approximation is plotted in fig. 3.34:

$$\kappa = 6 \cdot 10^{23}\rho^{0.5}T^{-3.5} \tag{3.67}$$

The generated profiles are plotted in figs. 3.35, 3.36, 3.37 and 3.38.

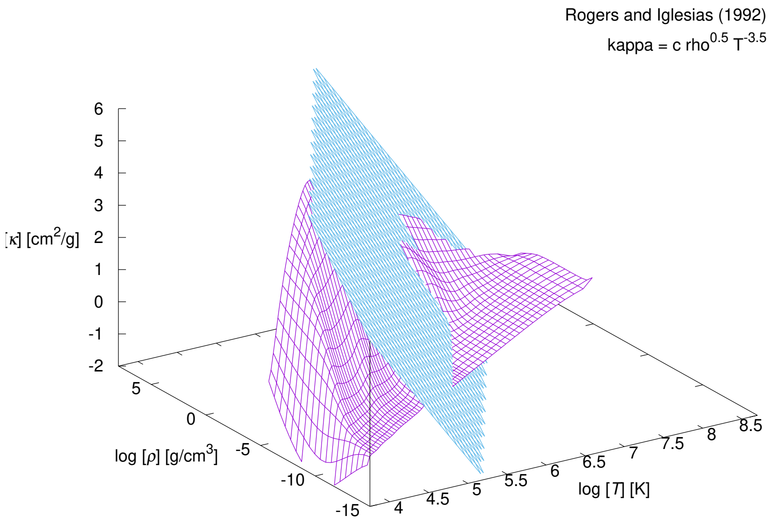

Figure 3.34: $\kappa = 6 \cdot 10^{23}\rho^{2}T^{-1}$ surface. Otherwise same as in fig. 3.6.The approximation was chosen as an inspection of opacity regimes that hold for higher temperatures.

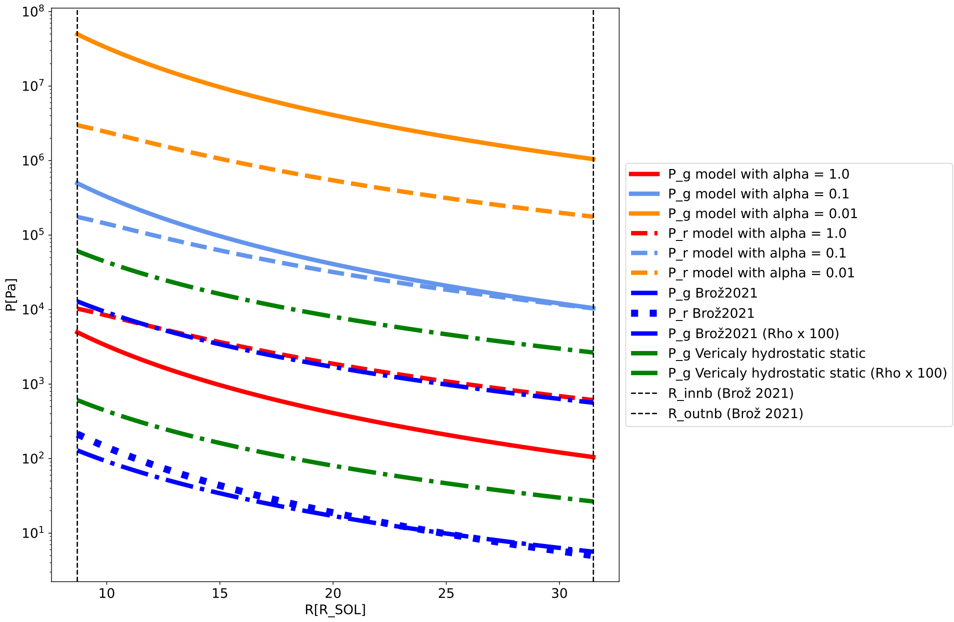

Figure 3.35: Ideal gas and radiation pressure profiles calculated for the derived model ($P_\mathrm{r} \gg P_\mathrm{g}$, $\kappa = 6{\cdot}10^{23}\rho^2T^{-1}$) with parameters of the β Lyrae system and $\alpha = 1.0, 10^{-1}, 10^{-2}$. Otherwise same description as 3.10. The resulting profiles are only consistent with the $P_g \gg P_r$ assumption for α close to 1.0.

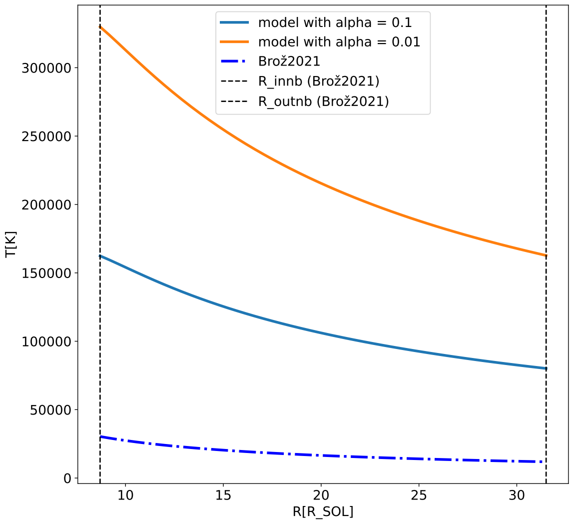

Figure 3.36: Temperature profile from the derived model ($P_\mathrm{r} \gg P_\mathrm{g}$, $\kappa = 6 \cdot 10^{23}\rho^2T^{-1}$) with parameters of the β Lyrae system and $\alpha = 10^{-1}, 10^{-2}$ is compared to the temperature profile obtained by [Brož et al., 2021] The resulting temperatures are much higher than for models with other assumptions.

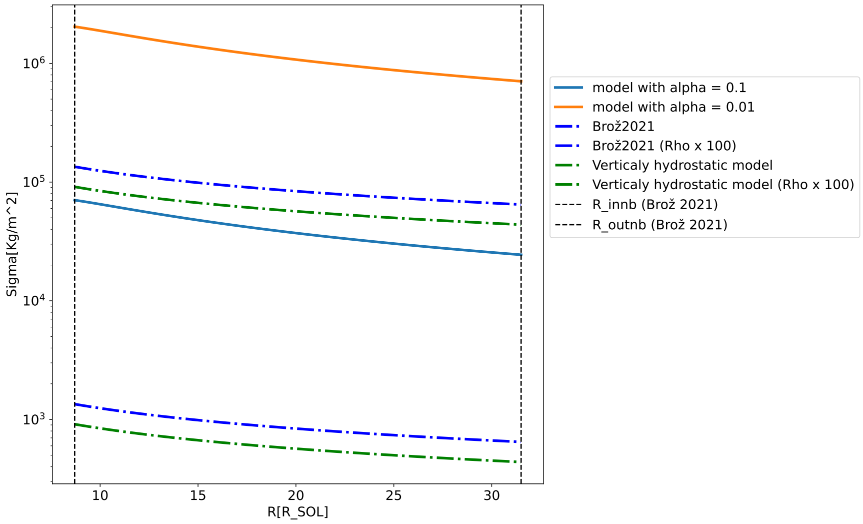

Figure 3.37: Vertically integrated density Σ profile from the derived model ($P_\mathrm{r} \gg P_\mathrm{g}$, $\kappa = 6 \cdot 10^{23} \rho^2 T^{-1}$) with parameters of the β Lyrae system and $\alpha = 10^{-1}, 10^{-2}$. Otherwise, see the description of fig. 3.8. The derived Σ-profiles are systematically larger than the fitted observations.

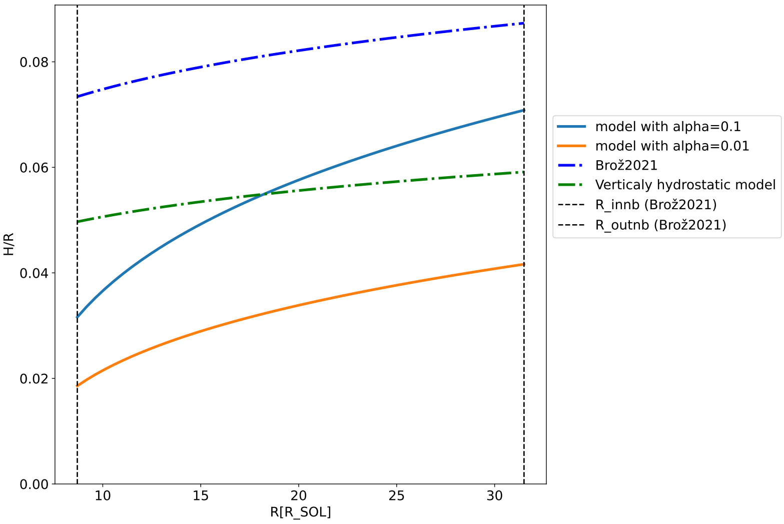

Figure 3.38: Aspect ratio profile from the derived model ($P_\mathrm{r} \gg P_\mathrm{g}$, $\kappa = 6 \cdot 10^{23} \rho^2 T^{-1}$) with parameters of the β Lyrae system. Otherwise, see the description of fig. 3.10. The radial dependency of the aspect ratio is much steeper than for other models.

Discussion of the($P_g \ll P_r$; $\kappa = 6 \cdot 10^{23} \rho^{0.5} T^{-3.5}$) model.

- From the pressure profiles in fig. 3.35 we see that the $P_g \ll P_r$ is satisfied for α close to 1.0.
- Higher temperature discs (lower α) seem to produce a thinner disc, which is contra-intuitive. Here we note that this aspect of the model should not necessarily be taken to be real, since it is for cases that are not consistent with the $P_\mathrm{g} \ll P_\mathrm{r}$ assumption and around $\alpha \approx 1.0$, where the assumption is met, the effect is very weak; $T \propto \alpha^{0.3}$.
- If we take the predictions of Σ and H from the other models as correct ones, then it seems possible to construct a much hotter disc with a similar vertical extent and similar Σ.

3.4 Timescales for β Lyr A and numerical simulations.

In this section, we investigate and compare various timescales calculated for different models of β Lyr A. Our goal is to investigate possible dynamics and to gauge the length of simulations conducted in the next chapter.

3.4.1 Viscous timescale

Matter and the angular momentum in an accretion disc are redistributed on a viscous timescale;

$$t_\nu = \frac{R^2}{\nu} \tag{3.68}$$

Where ν is the kinematic viscosity. In the case of discs that can reach a steady state, we usually assume that a disc/a part of a disc is close to a steady state after several viscous timescales have elapsed. Assuming the Shakura and Sunyaev [1973] formula for kinematic viscosity:

$$\nu = \alpha H c_s \tag{3.69}$$

where H is the pressure scale height, c_s is the sound speed. We see that t_ν will be longer for a lower α, this is what we would expect since α was defined to scale the efficiency of the angular momentum exchange in the disc. A comparison of the viscous timescales derived for different models is plotted in fig. 3.39.

The viscous timescale implied by the ($P_\mathrm{g} \gg P_\mathrm{r}$; $\kappa = 10^{18.6}\rho^{0.77}T^{-1.0}$) model suggests a significantly lower timescale than the kinematic model form Brož et al. [2021]. The prescription for in equation 3.69 is proportional to temperature and Σ though c_s and H, hence since our model predicts significantly higher profiles of Σ and T a higher viscosity is implied (and so a lower viscous timescale). We may also look at this in the sense that by adding dynamics into consideration (in comparison to the kinematic model) the model is gauged by the set amount of matter that must be transported $\dot{M} = 2 \cdot 10^{-5}$.

3.4.2 Dynamical and vertical timescale

In the theory of standard steady-state Keplerian discs as discussed in section 1.2, the time it takes for a hydrostatic equilibrium to be established in the vertical direction (the vertical timescale t_z) is simply equal to the orbital period (the dynamical timescale t_dyn).

$$t_z = \frac{H}{c_s} \tag{3.70}$$

$$t_\mathrm{dyn} = \frac{1}{\Omega_K} \tag{3.71}$$

$$t_z = t_\mathrm{dyn} \tag{3.72}$$

The vertical timescale is equal to the time it takes for a sound wave to travel over the vertical extent of the disc from the mid-plane.

In fig. 3.40 we see that the ($P_\mathrm{g} \gg P_\mathrm{r}$; $\kappa = 10^{18.6}\rho^{0.77}T^{-1.0}$) model described in this chapter is in better agreement with the "Vertically hydrostatic model" by about 75% in comparison to the Shakura and Sunyaev [1973] models. We note that this does not necessarily mean that the result is equal to the real timescale for establishing a vertical equilibrium, because both models enforce a vertical hydrostatic equilibrium, which is not guaranteed, we note for example that Brož et al. [2021] in their "Joint" model consider the disc vertically unstable.

3.4.3 Sound-speed timescale

The sound-speed timescale is the time that it takes for a compressional wave to travel to a certain radius in the disc (see section 1.2.5.2).

$$t_{\mathrm{c_s}} = \frac{R}{c_s} \tag{3.73}$$

In fig. 3.41 we see that the analytical model ($P_{\mathrm{g}} \gg P_{\mathrm{r}}$; $\kappa = 10^{18.6}\rho^{0.77}T^{-1.0}$) (as well as other classical gas dominated ”S&S” models with $\alpha = 0.1$) differs from the ”Vertically hydrostatic model” on the order of days. Similarly as in the discussion of the vertical timescale, also here we emphasize that both models assume vertical hydrostatic equilibrium and so we may not be sure that this corresponds to reality.

A noticeable correspondence is between the sound-speed timescale of the ”Vertically hydrostatic model” and ($P_{\mathrm{g}} \gg P_{\mathrm{r}}$; $\kappa = 10^{18.6}\rho^{0.77}T^{-1.0}$) at the outer boundary of the disc with the binary period. We take this as an indication that spiral waves caused by the tidal interaction with the donor may be present in the disc. Boffin [2008] showed that spiral waves propagating inward will travel at roughly the sound speed, which is slower than the orbital motion in the disc. This differential rotation leads to an angular momentum loss and hence to enhanced accretion. In other words, spiral waces operate as an additional form of viscosity. This is possible when the 3:1 Lindblad resonance is located in the disc. Boffin [2008] state that this is possible for a binary mass ratio of $q < 0.33$, which is also for the case OF β Lyr A disc studied here.

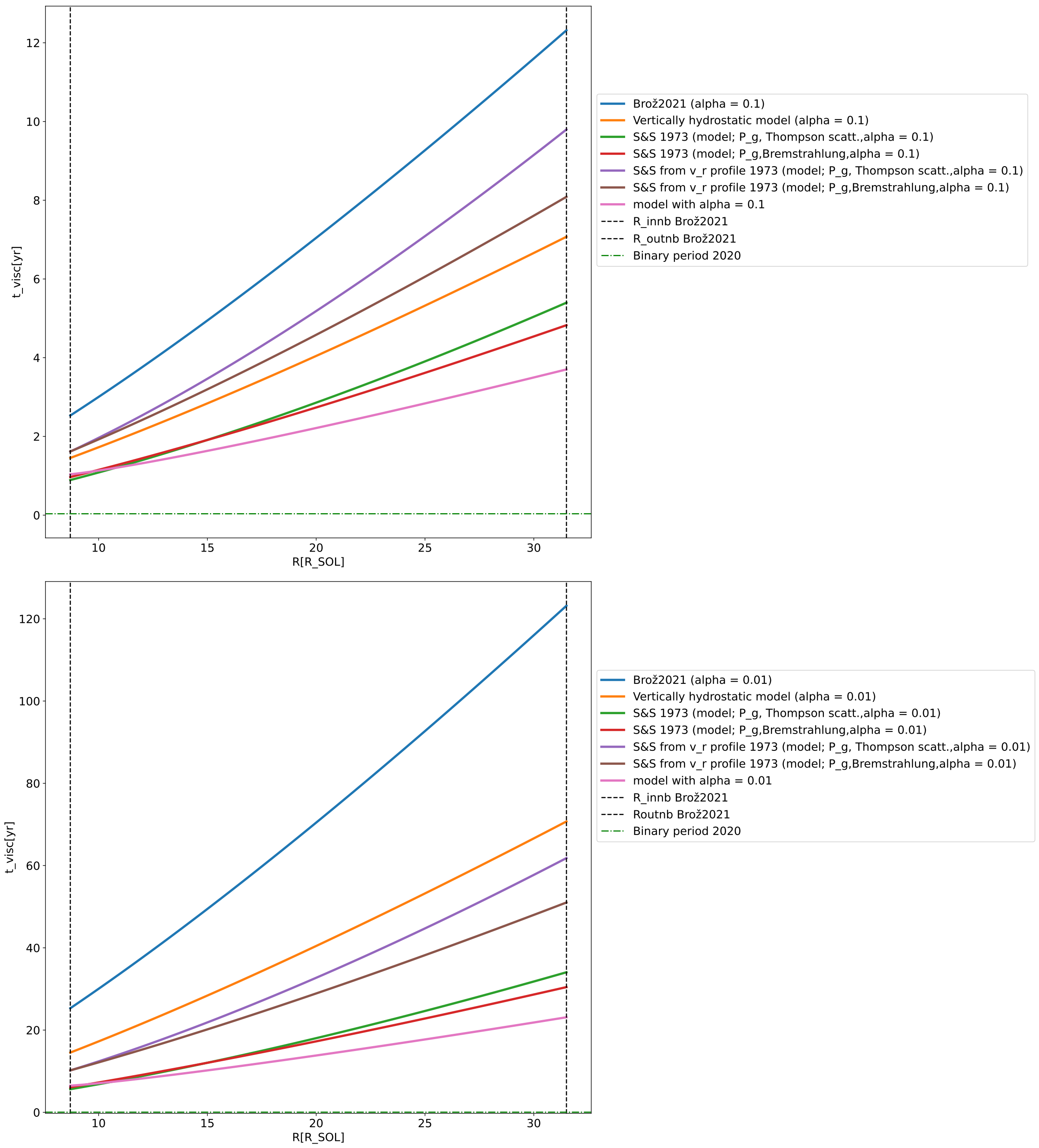

Figure 3.39: Viscous time scales calculated from different models of β Lyr A assuming $\alpha = 0.1$ and $\alpha = 0.01$. ”Brož 2021” profile was derived from the ”Joint” model of [Brož et al., 2021] and calculated the viscosity with the Shakura and Sunyaev [1973] formula. The ”Vertically hydrostatic model” was derived from the results of ”Brož 2021” by modifying the parameters $h_{\mathrm{cnb}}, \mu, \gamma$. ”S&S” denote models given in Shakura and Sunyaev [1973]. The profile denoted simply as ”model” refers to the ($P_{\mathrm{g}} \gg P_{\mathrm{r}}$; $\kappa = 10^{18.6}\rho^{0.77}T^{-1.0}$) model discussed in the main text.

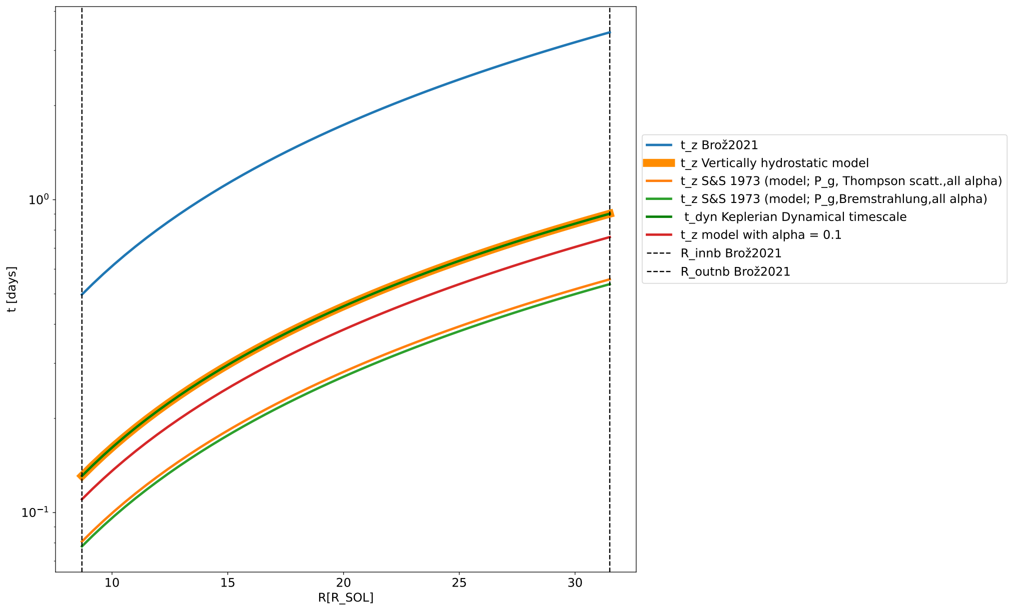

Figure 3.40: The Keplerian orbital timescale and the vertical timescale of β Lyr A. The vertical time scale is the time it takes to establish a vertical hydrostatic equilibrium. The "Brož 2021" time scale was derived by using the profiles from Brož et al. [2021]. The "Vertically hydrostatic model" was derived by modifying the parameters $h_{\rm cnb}, \mu, \gamma$. "S&S" denote models given in Shakura and Sunyaev [1973]. The profile simply denoted as "model" refers to the ($P_{\rm g} \gg P_{\rm r}$; $\kappa = 10^{18.6}\rho^{0.77}T^{-1.0}$) model discussed in the main text.

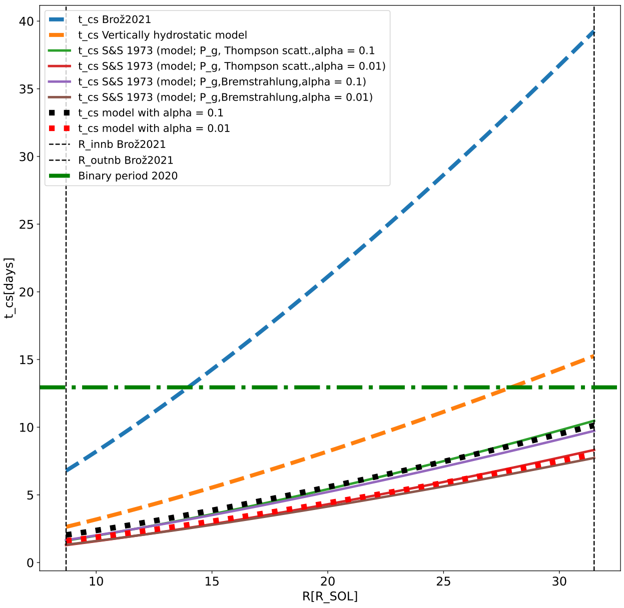

Figure 3.41: The sound-speed timescale of different models of β Lyr A. "Brož 2021" profile was obtained by using profiles for the "Joint" model in [Brož et al., 2021]. The "Vertically hydrostatic model" was derived from the results of "Brož 2021" by modifying the parameters $h_{\rm cnb}, \mu, \gamma$. "S&S" denote models given in [Shakura and Sunyaev, 1973]. The profile denoted as "model" refers to the ($P_{\rm g} \gg P_{\rm r}$; $\kappa = 10^{18.6}\rho^{0.77}T^{-1.0}$) model discussed in the main text.

4. 1D RHD models of β Lyrae

4.1 Preparations for FARGO_THORIN simulations

4.1.1 Implications of chapter 3

In the previous chapter, we derived analytical models under three different assumptions about the relative importance of gas pressure P_g and radiation pressure P_r ($P_g \gg P_r$, $P_g \approx P_r$, $P_g \ll P_r$) and using various approximations of the opacity function. The models generate profiles of a quantity q depending on:

$$q = q(R; \alpha, \dot{M}, M_\star) \tag{4.1}$$

where R denotes the radial coordinate, with the fixed parameters $\dot{M}$ the accretion rate, α the parametrization of viscosity according to [Shakura and Sunyaev, 1973] and $M_\star$ the mass of the central star. Each model was defined by an approximation of the opacity function κ, in the form;

$$\kappa = \kappa_0 \rho^A T^B \tag{4.2}$$

where κ_0,A,B are fixed parameters of the approximation. In the following chapter, we use the results from the most successful analytical models as the initial conditions for simulations with the FARGO_THORIN code. We draw the following implications for our numerical simulations:

- Analytical models assuming $P_g \gg P_r$ were able to generate profiles that were consistent with the assumption about the gas pressure, under which they were derived. In other cases, to consolidate classes of models with their assumptions, a high value of α and an opacity fitted to very high temperatures were needed. Hence, we expect that the disc is most likely gas pressure-dominated. This is advantageous because in FARGO_THORIN, the ideal gas state equation is already implemented. The gas pressure-dominated analytical models yield radiation pressures about $0.1\,P_\mathrm{g}$.
- All analytical models show temperatures much higher than those of the kinematic model fitted to observations from [Brož et al., 2021]. The $Q_\mathrm{visc} = Q_\mathrm{vert}$ balance for the atmosphere modeled according to [Hubený, 1990] and the accretion rate $\dot{M} = 2 \cdot 10^{-5} \mathrm{M}_\odot/\mathrm{yr}$ implies A very strong viscous heating. For all opacity prescriptions in equation 4.2 higher α viscosity parameters yield lower temperature profiles. Even for the limit case of $\alpha = 1.0$, the temperatures are still significantly higher than in the kinematic model.
  We have to acknowledge that there is a substatial discrepancy between the assumptions about the vertical temperature profile between the two models. The analytical models assume that the disc radiates from its faces according to the Stephan Boltzmann law, with the effective temperature T_eff, which is obtained as the temperature in the midplane seen through the optical depth of τ_eff, which is calculated in the optically thick limit, according to [Hubený, 1990]. On the other hand, the kinematic model assumes that the disc is either vertically isothermal or allows for a temperature inversion in the otherwise isothermal atmosphere, that is the upper layers may have higher temperatures than the midplane.
- The analytical models generate profiles with much larger Σ than the kinematic model. Depending on α, the surface densities are more than 100 times larger for $\alpha = 0.01$. the lower α yields even higher Σ. $\dot{M}$ is a fixed parameter as it is inferred from observations of the change of the binary period $\dot{P}$. The theory of steady-state thin accretion discs, as described in section 1.2, shows that the radial velocities are proportional to the kinematic viscosity ν, which is parametrised by α. For the set amount of matter that is to be transported through the disc, lower velocities imply that more matter must be present in the disc at any given moment. Also in the energy balance equation, the temperature is coupled to Σ through the optical depth approximation.
- The aspect ratio profiles H/r generated by the analytical models are consistent with the thin disc assumption $H \ll r$ (under which the entire theory in section 1.2 was derived). The aspect ratio

profiles for $\alpha = 1, 10^{-1}\text{and}10^{-2}$ are located between the kinematic model and the vertically hydrostatic model. That is, due to the high midplane temperatures, the analytical models can generate H magnitudes equal to those in [Brož et al., 2021] at a hydrostatic equilibrium ($h_{\mathrm{cnb}} = 1$).

- The viscous timescales based on different models, as plotted in 3.39, can be then used to plan a simulation length if we need to further relax the disc into a steady state.

4.1.2 FARGO_THORIN input parameters

The FARGO_THORIN model is controlled by a number of input parameters. In this section, we review the notation and provide definitions whenever needed. For each model, we also include a list of parameter values. We present these values in SI, solar or CGS units. In the control file, however, the parameters must be presented in the code units.

Table 4.1: FARGO_THORIN input parameters

Parameter	Unit	Definition
$M_\star$	$M_\odot$	Mass of the central star
R_{innb}	$R_\odot$	Inner boundary of the mesh/disc
R_{outnb}	$R_\odot$	Outer boundary of the mesh/disc
$\dot{M}$	$M_\odot \cdot \mathrm{yr}^{-1}$	Mass transfer rate
Σ_0	$\mathrm{kg} \cdot \mathrm{m}^{-2}$	Normalisation of a power-law for the initial profile of Σ, defined at 1 AU .
σ_0	1	Exponent of the power-law for the initial profile of Σ
$\left(\frac{H}{r}\right)_0$	1	Normalisation of a power-law for the initial aspect ratio, defined at 1 AU.
h_{flare}	1	Exponent of a power-law for the initial aspect ratio profile.
κ	$\mathrm{cm}^2 \cdot \mathrm{g}^{-1}$	The choice of opacity law/ opacity table
C_{k}	1	Defines the change in opacity above the midplane, as discussed in 1.3.5.2
α	1	The parametrisation of opacity introduced in section 1.2
γ	1	Adiabatic index
μ	AMU	Mean molecular weight
$T_\star$	K	The effective black-body temperature of the central star.
$R_\star$	$R_\odot$	The radius of the central star.
A	1	The disc's albedo.
t_{damp}	$2\pi\Omega_{\mathrm{K}}^{-1}$	Characteristic damping scale as explained in section 1.3.7
R_{inDAMP}	1	Fraction of R_{innb} where the inner damping zone ends
R_{outDAMP}	1	Fraction of R_{outnb} where outer the damping zone ends
r_{sm}	R_{HILL}	Gravitational potential smoothing length as described in section 1.3.3
t_{total}	yr	Total duration of the simulation
N_{r}	1	Number of evenly-spaced rings in the radial direction
N_ϕ	1	Number of evenly-spaced sectors in the azimuthal direction

We further note that:

- the mass of the central star is always set to $13.048\mathrm{M}_\odot$. The mass transfer rate is always assumed $\dot{M} = 2 \cdot 10^{-5}\mathrm{M}_\odot$.
- $\left(\frac{H}{r}\right)_0$, Σ_0, h_{flare} and σ_0 are only used to initialize the first estimate of energy in the iterative routine that finds initial conditions described in 1.3.6. h_{flare} is always chosen 0, in the following lists, it is omitted.
- Only the α parametrisation of viscosity is used in the here-described models and we always used $\alpha = \text{const.}$ with radius. The radial profile formula described in Eq. (1.86) also results in constant α, because at the considered range of temperatures, the disc is fully ionised.
- $T_\star$, $R_\star$ and A only play a role when stellar irradiation is turned on, see section 1.3.5.3.

- R_{inDAMP} is always set to 1.2, R_{outDAMP} is always set to 0.9 and t_{damp} is always 0.1. We omit them in the lists below.
- r_{sm} is always set to 0.6 and does not play a large role in discs without massive bodies present; it is also omitted in the lists below.
- In this thesis, we present 1D profiles, but N_ϕ must be always at least 2.
- The code uses an adaptive time step to fulfil the CFL condition at each step.

FARGO_THORIN was built to simulate protoplanetary discs and requires a body of some sort to be present in the disc for it to be computed. Since we are studying a circumstellar disc arising from mass transfer between two stars where no bodies are present we specified a small test particle with the following parameters.

Table 4.2: Test particle parameters

Parameter	Unit	Value
M_{particle}	$M_\star$	$1 \cdot 10^{-12}$
a_{particle}	AU	0.1

M_{particle} denoted the particles set mass and a_{particle} denotes the distance from the star at which it orbits. All other orbital parameters are set to zero.

4.1.3 Note on the notation in figures

In this section, we define a notation for the following discussion of individual models.

T denotes the midplane temperature of the disc.

T_{eff} denotes the atmospheric temperature of the disc, calculated from the following equation:

$$T_{\mathrm{eff}} = \frac{T}{(\tau_{\mathrm{eff}})^{\frac{1}{4}}} \tag{4.3}$$

where τ_{eff} is the effective optical depth of the midplane according to Hubený [1990], as was discussed in section 1.3.5.2. With the assumed atmosphere model, T_{eff} is the temperature with which the energy is radiated.

T_{irr} (in simulations where the stellar irradiation is switched on) denotes the projected temperature of the central star onto the face of the disc, as is described in section 1.3.5.3.

v_r denotes the radial velocity in the disc.

v_Θ is the azimuthal velocity of the disc.

$\dot{M}$ is the flux of matter across individual rings calculated as:

$$\dot{M} = -2\pi r v_r \Sigma \tag{4.4}$$

Other quantities are denoted the same as in the rest of this thesis. We also keep the terms "Broz 2021" for the profiles of the "Joint" model from Brož et al. [2021] and the modified version of these profiles (as discussed at the beginning of chapter 4), i.e., the "Vertically hydrostatic model".

4.2 Models with general opacity tables

In this section, we present the results of simulations in FARGO_THORIN with general opacity tables. Two different opacity tables were used.

- Opacities based on [Zhu et al., 2012].
- Opacities based on [Bell and Lin, 1994].

Subsequently, we conduct experiments related to selected parameters, using the more complete opacity table [Zhu et al., 2012].

4.2.1 Model with the [Zhu et al., 2012] opacity table

Table 4.3: Model with [Zhu et al., 2012] opacity input parameters

Parameter	Unit	Value
$M_\star$	$M_\odot$	13.048
R_{innb}	$R_\odot$	5.987
R_{outnb}	$R_\odot$	31.5
$\dot{M}$	$M_\odot \cdot \mathrm{yr}^{-1}$	$2 \cdot 10^{-5}$
Σ_0	$\mathrm{kg} \cdot \mathrm{m}^{-2}$	26332.9
σ_0	1	0.42
$\left(\frac{H}{r}\right)_0$	1	0.05
κ	$\mathrm{cm}^2 \cdot \mathrm{g}^{-1}$	[Zhu et al., 2012]
C_{k}	1	0.6
α	1	0.1
γ	1	1.4
μ	AMU	0.5
$T_\star$	K	30000
$R_\star$	$R_\odot$	5.987
A	1	0.5
t_{total}	yr	5
N_{r}	1	200
N_ϕ	1	2

This model will serve as a baseline for our further experiments, hence in the following figures we present a wide range of parameters. As parameters of the simulation, we chose the values that Chrenko et al. [2017] advises, disc parameters adopted from Brož et al. [2021] and values that seemed sensible in the analytical models. The choice of $\alpha = 0.1$ fo the base-line model was motivated by possible comparisons to the analytical models. Higher α values are discussed later in this chapter.

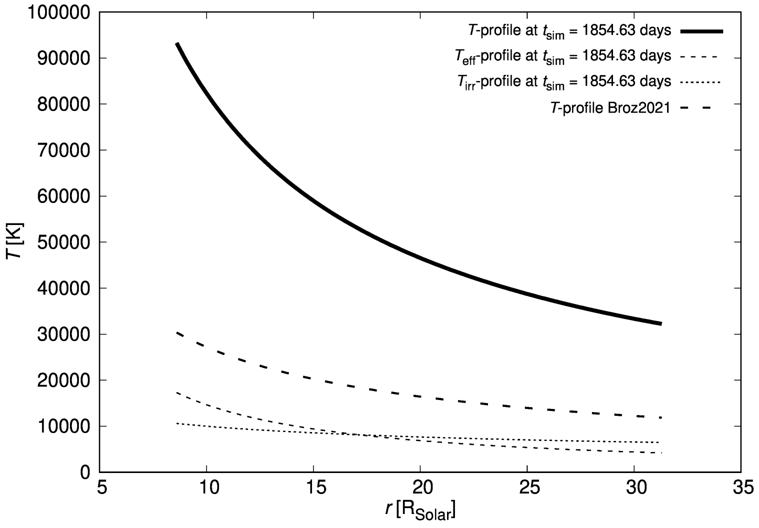

Figure 4.1: Temperature profiles of the model defined by parameters in tab. 4.3. For notation see sec. 4.1.3. The temperature profile stabilized after a few tens of orbits of the test particle and showed no further evolution.

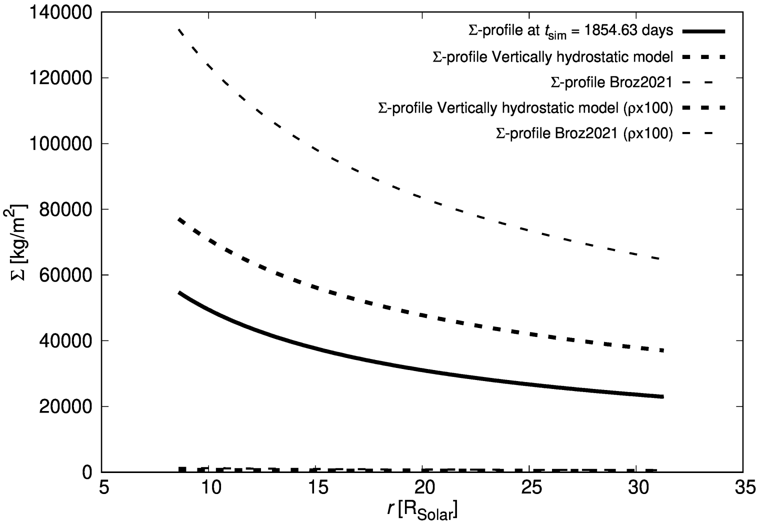

Figure 4.2: Σ profile of the model defined by parameters in tab. 4.3. For notation see sec. 4.1.3. The profile was stable for around two viscous timescales.

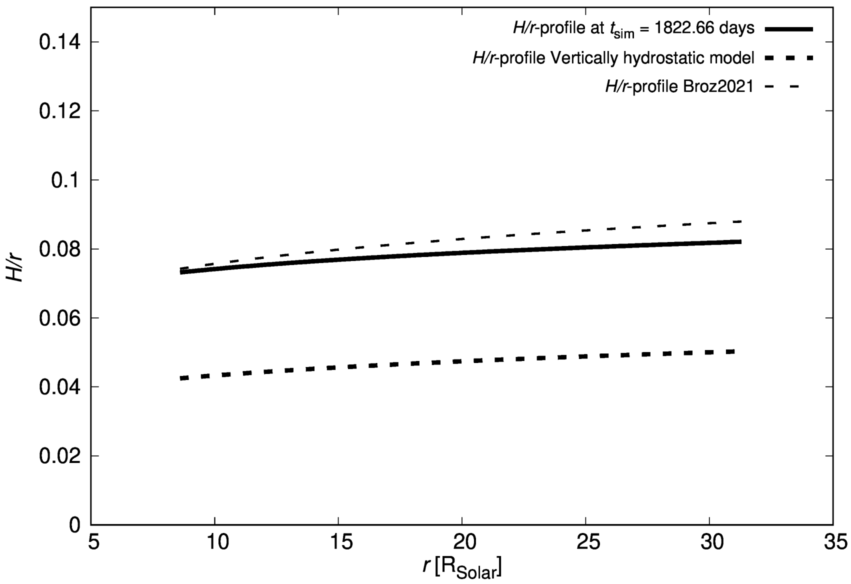

Figure 4.3: Aspect ratio profile of the model defined by parameters in tab. 4.3. For notation see sec. 4.1.3. The profile was stable for around two viscous timescales.

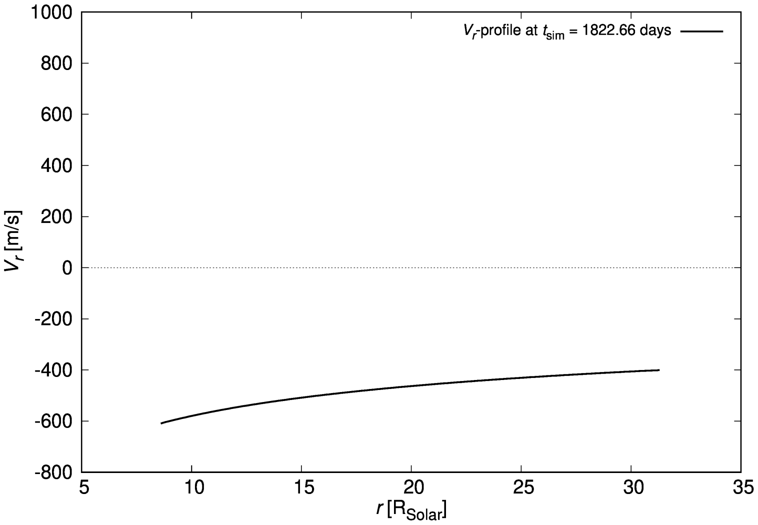

Figure 4.4: v_r profile of the radial velocity of the model defined by parameters in tab. 4.3. The profile was stable after less than a year elapsed.

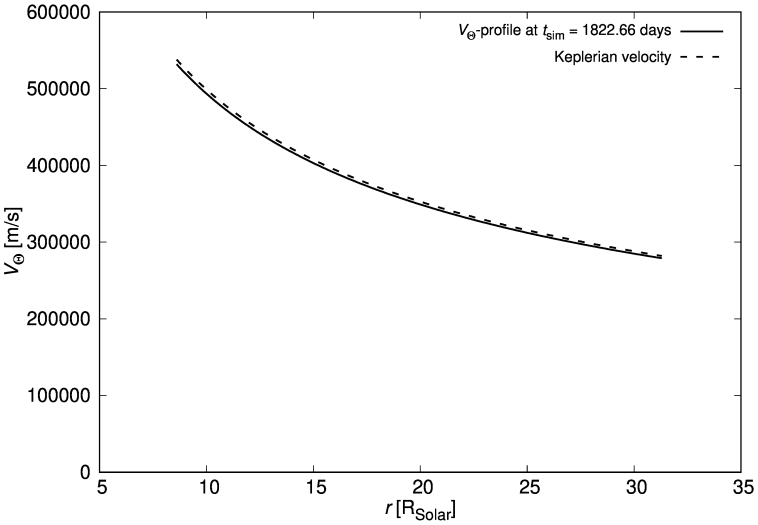

Figure 4.5: v_ϕ profile of the azimuthal velocity of the model defined by parameters in tab. 4.3. The profile stopped showing temporal evolution within a hundred days and the disc remained slightly sub-keplerian for the rest of the simulation time.

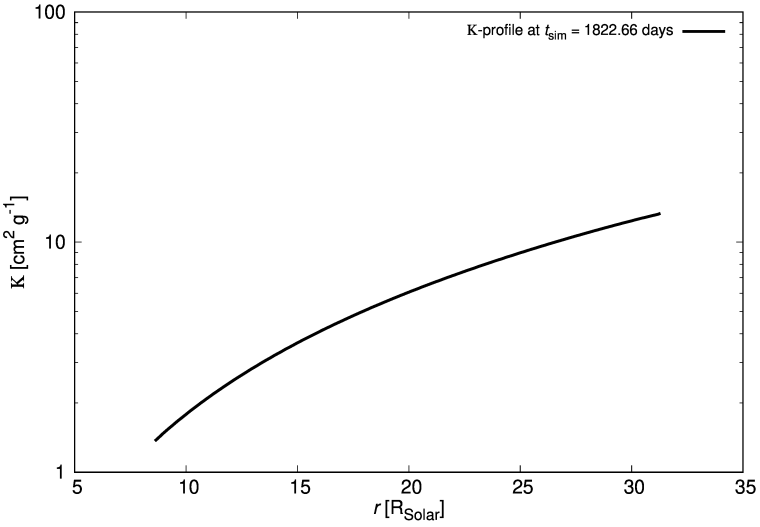

Figure 4.6: Opacity profile of the model defined by parameters in tab. 4.3. We observed basically no temporal evolution. The profile indicates no opacity transition in the disc.

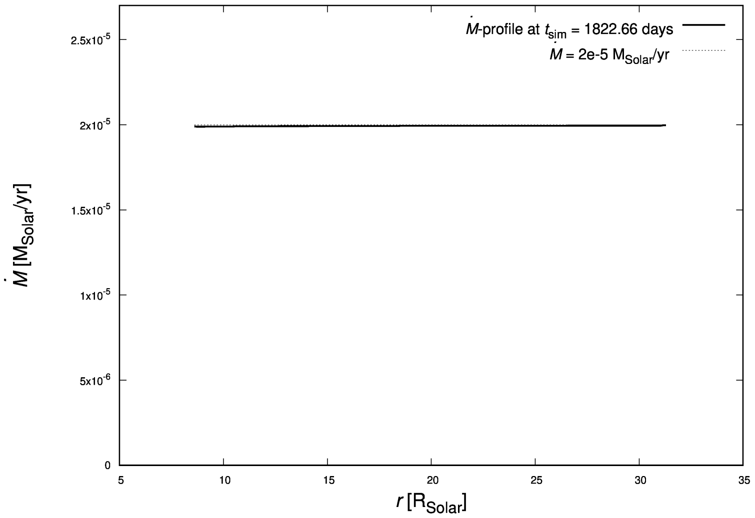

Figure 4.7: $\dot{M}$ profile of the model defined by parameters in tab. 4.3. For notation see sec. 4.1.3. The disc stabilizes to a radially constant flux of matter as defined by the boundary conditions.

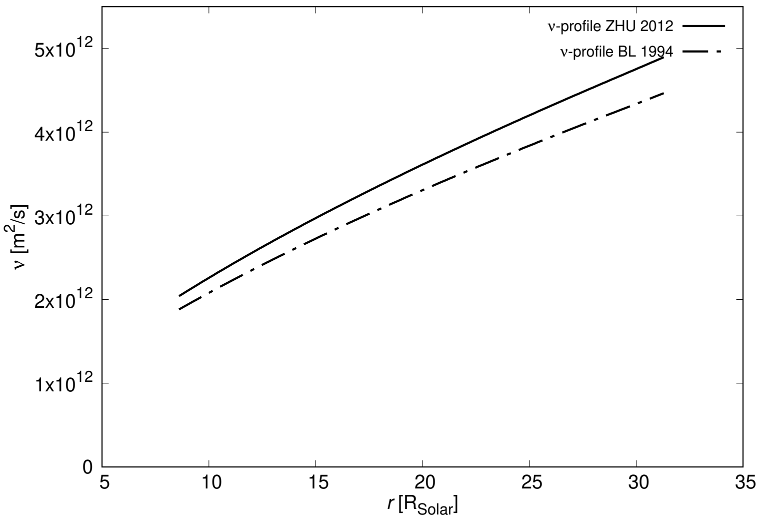

Figure 4.8: A comparison of viscosity profiles in the model defined by parameters in tab. 4.3 and the model described in sec. 4.2.3.

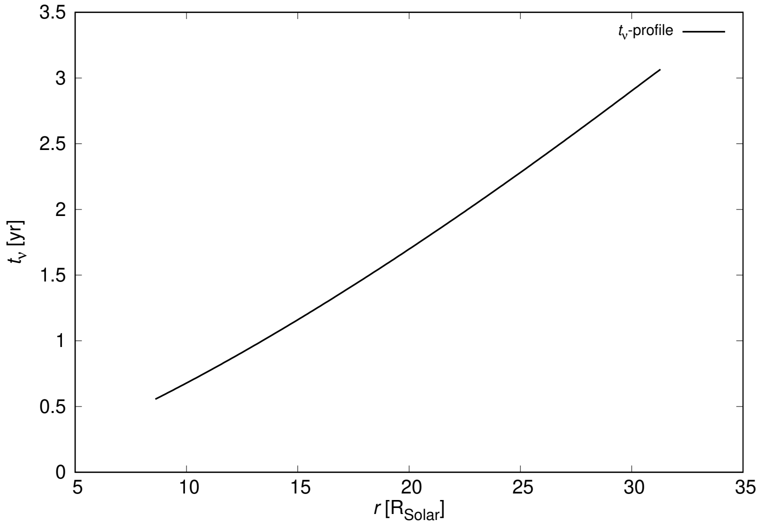

Figure 4.9: The viscosity timescale derived from the model defined by parameters in tab. 4.3.

Discussion of the model with the Zhu et al. [2012] opacity

- The model presented in the figures above seems to support many of the qualitative facts implied by the analytical models.
  - In fig.4.2, we see that Σ of magnitudes close to 100 times the Σ profile of the ”Vertically hydrostatic model” is needed to transfer the required amount of matter.
  - As in the analytical models, even in the observationally well-constrained outer part of the disc, the midplane temperature T of the numerical model is around triple that of the kinematic model (fig. 4.1).

  - The disc seems to reach a steady state rather quickly. Within one year of the simulation time, we stopped seeing temporal evolution in all profiles. Hence we can take this as an indication that the steady-state disc theory can be applied.
  - The disc rotates with a slightly sub-keplerian velocity due to a radial pressure gradient in the disc (fig. 4.5). However the deviations are minor, hence it does not seem a long stretch to apply analytical models valid for Keplerian discs.
  - Similarly to the analytical models (see for example section 3.3.2.3), due to the high temperatures the model can reach a good agreement with the kinematic model aspect ratio even under the assumption of the vertical hydrostatic equilibrium (which is implemented in FARGO_THORIN), as opposed to the $h_{\mathrm{cnb}} = 3.8$ value in Brož et al. [2021]). We recall that in the analytical models, the aspect ratio was also higher than in the "Vertically hydrostatic model" (fig. 4.3).
  - The general opacity table does not imply any opacity transitions in the disc, hence this gives further validity to the use of the models described in chapter 3. The opacity profile implied by the Zhu et al. [2012] opacity table agrees in magnitude with the ($P_{\mathrm{g}} \gg P_{\mathrm{r}}$, $\kappa = 10^{18.6}\rho^{0.77}T^{-2.5}$) analytical model discussed in sec. 3.3.2.3.
  - In sec. 3.4.1, we plotted the viscous timescale to check whether we can trust the fact that we weren't seeing any temporal evolution. We see that the length of the viscous timescale agrees well with the estimates derived from the ($P_{\mathrm{g}} \gg P_{\mathrm{r}}$, $\kappa = 10^{18.6}\rho^{0.77}T^{-2.5}$) analytical model in fig. 3.39. For the inner part of the disc, the simulation length was five to ten times longer than the viscous timescale.
  - In general the numerical model with a general opacity table seems to ensure a better correspondence between the dynamical and kinematical models, in the qualitative nature of the curves. This has two aspects to it:
    - In the outer part of the disc, all three types of models basically follow a power law. In the analytical models, this power law is determined by the choice of opacity in the disc, while in the numerical model with a general opacity table, there is no need to 'guess' the opacity perfectly, hence the correspondence to observations in the shape of the radial profile is more simply achieved.
    - The kinematic model assumes power laws for the profiles of physical quantities. The analytical models are not simple power laws due to the term:

      $$q \propto r^k \left(1 - \sqrt{\frac{R_\star}{r}})^l\right)\,, \tag{4.5}$$

      where k and l are some general exponents and some hydrodynamical quantity. This term arises from assuming a boundary condition that the disc azimuthal velocity profile must be at the surface of the star equal to the sub-keplerian rotational velocity of the star. The term causes the analytical models to bend significantly to lower values close to the inner boundary. The numerical model does not take dynamical interactions with the central star into account, hence there is nothing to force the profiles of the numerical model to bend.

  We take the fact that there is a reasonable agreement between the analytical models and the numerical model as a form of verification for the code. Later in this chapter, we describe simulations based on the simplified opacities that were used for the analytical models to further check the correspondence between the models.

- *The Σ problem.* The discrepancy in the profiles of vertically integrated density is acceptable. As was discussed in chapter 3, the Σ profile of the kinematic model is a lower limit to densities that could explain the observations. In taking into consideration dynamics we enforce a fixed amount o matter that must be transferred through the disc (given by $\dot{M}$). Hence the density will be dependent on the radial velocity in the disc, which is in turn determined by angular momentum redistribution. The efficiency of viscous forces in transporting angular momentum out is controlled by α, hence a theoretical lower limit to vertically integrated densities arising from considering dynamics in the system would be determined by the Σ profile for $\alpha = 1.0$. We note that there are other ways to increase the viscosity of the disc, for example, if a mechanism is found for increasing the midplane temperature then viscosity will also increase because sound speed and H will increase and this will through greater angular momentum transport lead to higher radial velocity.

- *The temperature problem.* We discuss the temperature profiles and the discrepancy in temperature between the kinematic and dynamical models in a separate section 4.2.1.1.

4.2.1.1 The temperature problem

The most dramatic disagreement between the kinematic model constrained by observations [Brož et al., 2021] and the dynamical models is the almost order-of-magnitude discrepancy in the midplane temperature profiles. An important aspect to consider is that each approach has completely different assumptions about the vertical temperature profile of the disc. Let us discuss each in turn:

- Brož et al. [2021] assume a vertically isothermal atmosphere. The disc is optically thick, hence the observations by which they constrain their model are observations of the atmosphere. That means that they infer the midplane temperature as being equal to the atmospheric temperature. They also allow for a temperature inversion in their model, so that the outer atmosphere can even be hotter than the midplane temperature.
- Both FARGO_THORIN Chrenko et al. [2017] and the analytical models derived in this thesis assume the atmosphere model derived by Hubený [1990]. We described the prescription for the optical depth in sec. 1.3.5.2. The atmosphere dims the midplane and the face of the disc radiates with the atmospheric temperature, which is lower.

If we reject the possibility of an isothermal atmosphere and re-interpret the ("Brož 2021") profile as the measured atmospheric temperature, then it should be rather straightforwardly compared to the atmospheric temperature T_{eff} inferred from the midplane temperature, according to the Chrenko et al. [2017] model atmosphere (see sec. 4.1.3). Theoretically, the upper thermodynamic limit to T_{eff} could also be the irradiation temperature T_{irr}.

In fig. 4.1, we see that the three temperatures are of comparable magnitudes but the agreement between the models is still rather poor. In the following sections, we will try to adjust the parameters of the model, in order to better reconcile the models with respect to each other.

4.2.2 Setting albedo to zero

The following model uses the same parameters as listed in table 4.3, but the albedo of the disc is set to zero, $A = 0$.

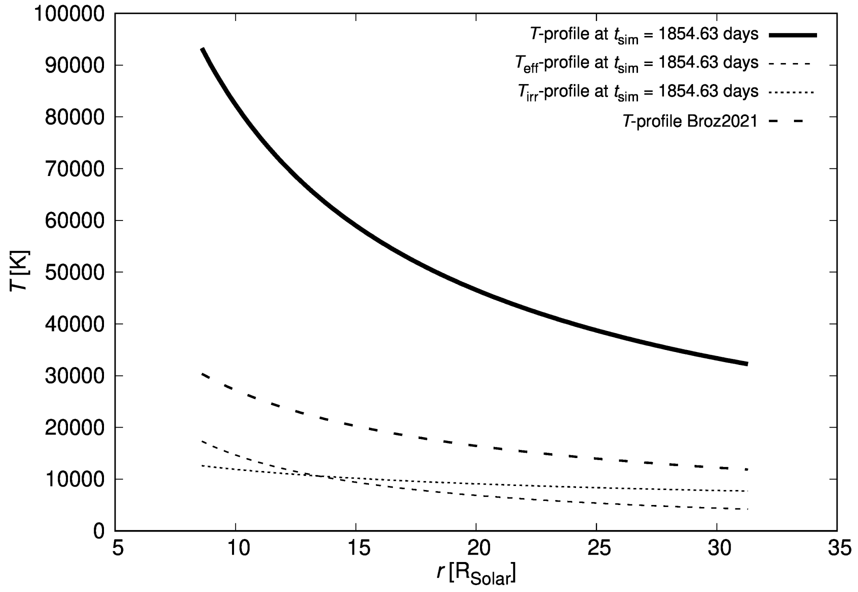

Figure 4.10: Temperature profiles of the model defined by parameters in tab. 4.3, but with the disc's albedo set to zero, $A = 0$. For notation, see sec. 4.1.3.

If we consider T_{irr} to be the thermodynamic limit to T_{eff}, then to reconcile the models we need the profile from the kinematic model [Brož et al., 2021] be lower or equal to this limit. In the first approach to increase T_{irr}, we assume that all of the irradiation from the central star is absorbed by the disc. In fig. 4.10, we see that this has a negligible effect on the midplane and atmospheric temperature generated by the numerical model, but it slightly increases the irradiation temperature. The effect isn't large due to the fourth power of temperature in the Stefan-Boltzmann law. Other hydrodynamical quantities are affected negligibly.

4.2.3 Model with the Bell and Lin [1994] opacity

To estimate the uncertainty of the opacity, we run the same simulation as defined by parameters in table 4.3 (with the albedo set to zero again) but with a different opacity table.

Table 4.4: Model with Bell and Lin [1994] opacity input parameters

Parameter	Unit	Value
$M_\star$	$M_\odot$	13.048
R_{innb}	$R_\odot$	5.987
R_{outnb}	$R_\odot$	31.5
$\dot{M}$	$M_\odot \cdot \mathrm{yr}^{-1}$	$2 \cdot 10^{-5}$
Σ_0	$\mathrm{kg} \cdot \mathrm{m}^{-2}$	26332.9
σ_0	1	0.42
$\left(\frac{H}{r}\right)_0$	1	0.05
κ	$\mathrm{cm}^2 \cdot \mathrm{g}^{-1}$	[Bell and Lin, 1994]
C_{k}	1	0.6
α	1	0.1
γ	1	1.4
μ	AMU	0.5
$T_\star$	K	30000
$R_\star$	$R_\odot$	5.987
A	1	0.0
t_{total}	yr	5
N_{r}	1	200
N_ϕ	1	2

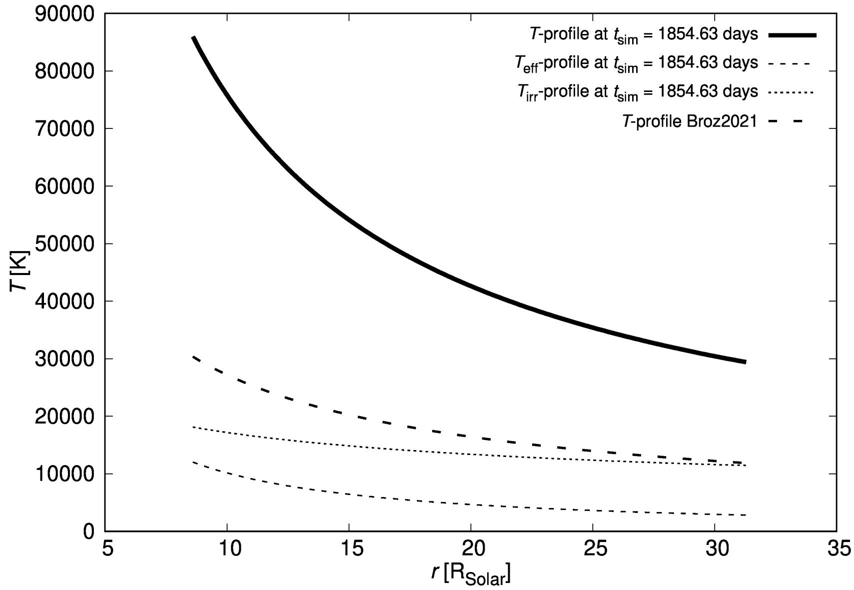

Figure 4.11: Temperature profiles of the model defined by parameters in tab. 4.4. For a full description of the notation see 4.1.3. There is a good coincidence between the kinematic model and the irradiation temperature.

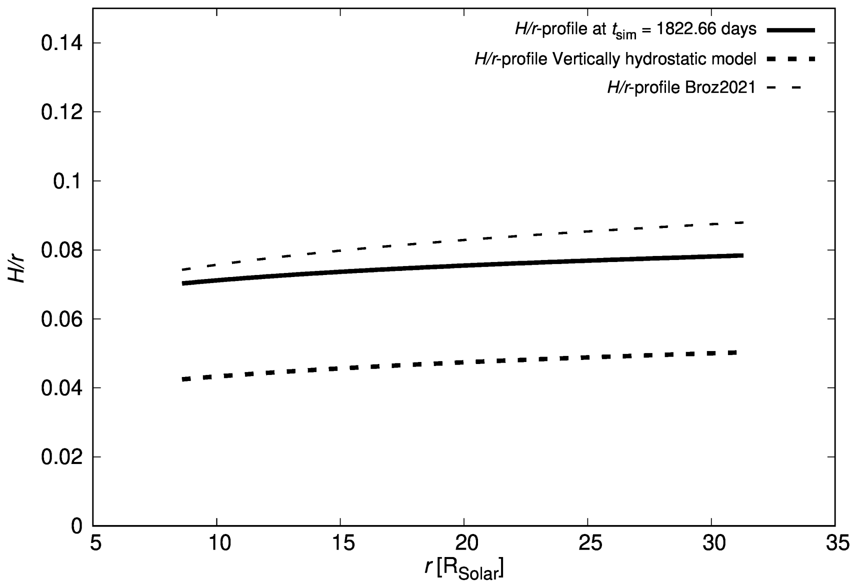

Figure 4.12: Aspect ratio profile of the model defined by parameters in tab. 4.4. For a full description of the notation see 4.1.3.

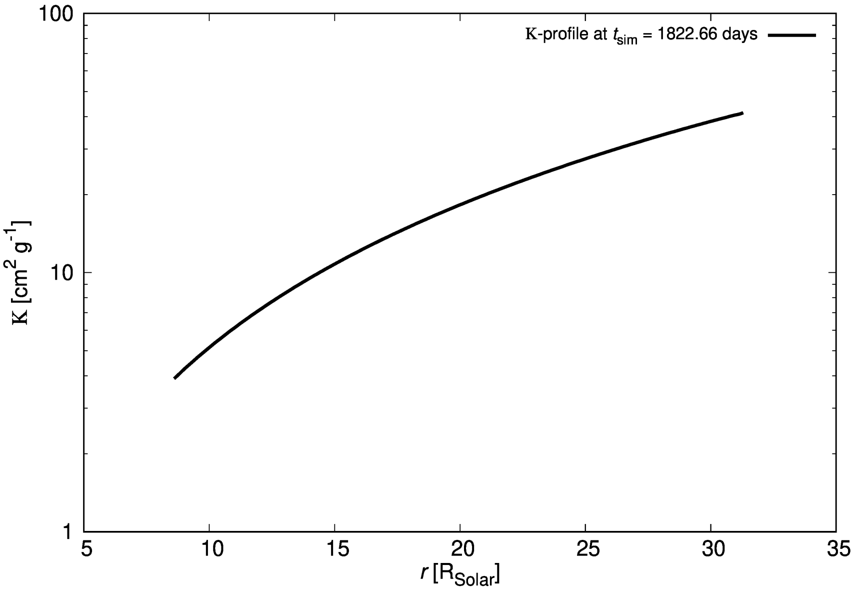

Figure 4.13: Opacity profile of the model defined by parameters in tab. 4.4.

Discussion of the model with the Bell and Lin [1994] opacity

In the figures above retaining this model, we only plotted values which exhibit clear changes due to change of the opacity table.

- In fig. 4.13, we see that the Bell and Lin [1994] opacity table prescribes almost a ten times higher opacity. Although the densities remained the same, the midplane temperature decreased by about ten thousand kelvins (fig. 4.11).
- The lower temperature implies a lower aspect ratio (fig. 4.12) by about 0.01 in the outer part of the disc.
- The $T_{\rm irr}$ profile generated by this model and the kinematic model coincide well in the outer part of the disc. If this were to be accepted, we could interpret it as that the kinematic model temperature profile 'sits' just on the thermodynamic limit to the atmospheric temperature. The discrepancy

between the two predicted atmospheric temperatures could be explained by a possible temperature inversion in the vertical temperature profile. The inner part of the disc, where the correspondence is worse, isn't well constrained by observations in the kinematic model.

- The difference in the profiles generated by the two different opacity tables can be interpreted as the uncertainty introduced to the model by the choice of opacity.

4.2.4 Changing the vertical opacity profile

The C_k parameter affects the vertical opacity profile. This parameter is typically set to 0.6 to account for a drop in opacity above the midplane in cool disks [Chrenko et al., 2017]. In principle, it is possible that a single opacity law governs the whole vertical opacity profile ($C_k = 1$). If this law is inversely proportional to temperature, then in a disc where the temperature decreases with z, the opacity can theoretically grow. We test the effects of this by setting $C_k = 1.5$. The parameters of this simulation are the same as in tab. 4.3 but with the following parameters changed.

Table 4.5: Model with a changed vertical opacity profile

Parameter	Unit	Value
κ	$\mathrm{cm}^2 \cdot \mathrm{g}^{-1}$	[Zhu et al., 2012]
C_k	1	1.5
α	1	0.1
A	1	0.0

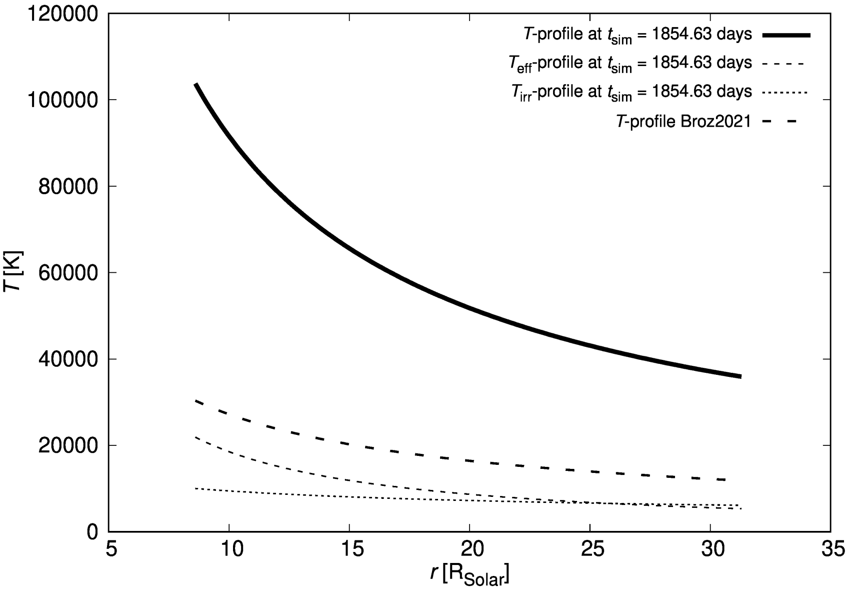

Figure 4.14: Temperature profiles of the model defined by parameters in tab. 4.5. For a full description of the notation see 4.1.3.

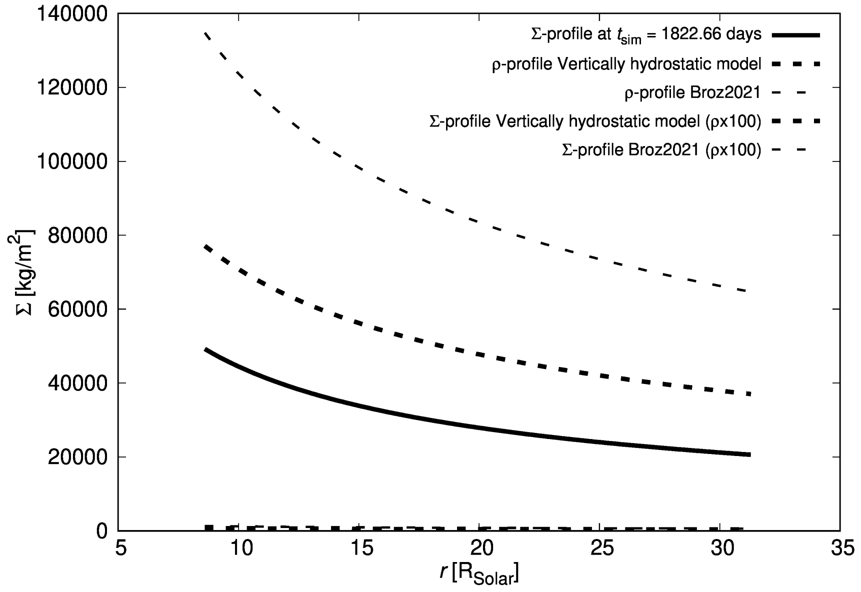

Figure 4.15: Σ profiles of the model defined by parameters in tab. 4.5. For a full description of the notation see 4.1.3.

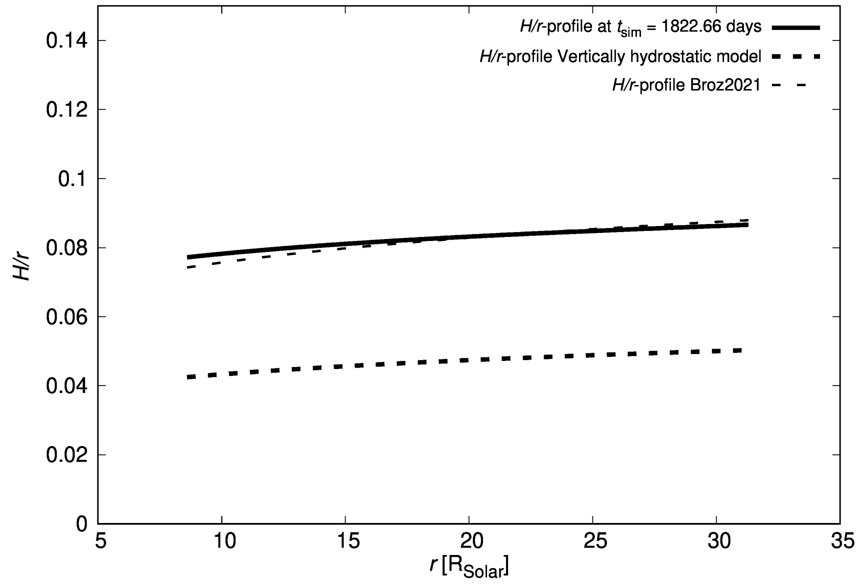

Figure 4.16: Aspect ratio profiles of the model defined by parameters in tab. 4.5. For a full description of the notation see 4.1.3.

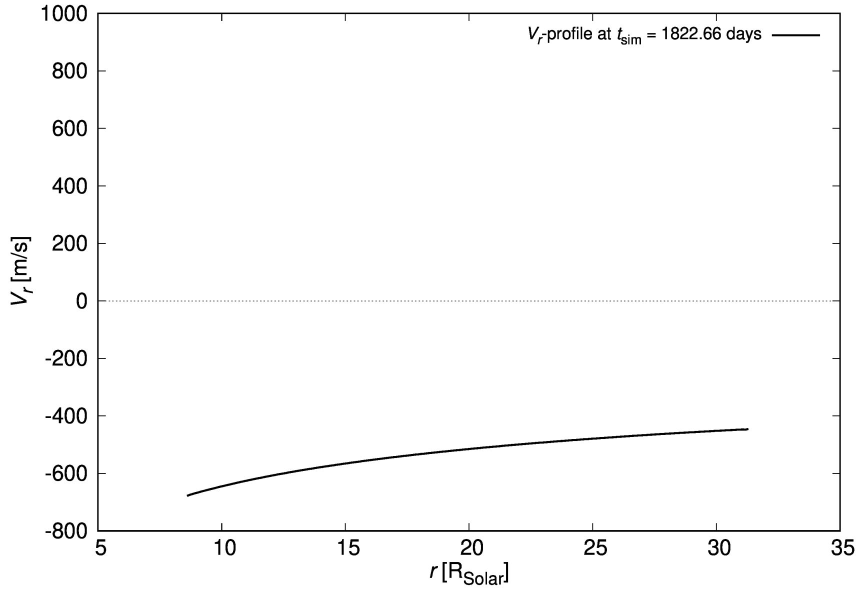

Figure 4.17: Radial velocity profile of the model defined by parameters in tab. 4.5.

Discussion of a model with a vertically changed opacity profile In figures 4.14, 4.15, 4.16 and 4.17 we plotted the results of this model.

- The opacity increase in the vertical direction acts as an extra layer of isolation, that is the optical depth of the midplane increases, taking into consideration the approximate energy balance between viscous dissipation and radiative cooling, we see that the midplane temperature increases (fig. 4.14).
- The increase in temperature implies a thicker disc (fig. 4.16), the aspect ratio is in very good agreement with the kinematic model.
- The increase in temperature also increases the viscosity in the numerical model (as discussed in section 4.2.1). The higher the viscosity, the more effective transport of angular momentum and hence greater radial velocities (in absolute value), as seen in fig. 4.17.
- Similarly to the discussion about the Σ profile in the numerical vs. the kinematic model, in fig. 4.15, we see a decrease of the vertically integrated density caused by higher radial velocities.
- Temperatures T_{eff} and T_{irr} coincide well in the outer part of the disc but both are lower than the kinematic model. In the inner part of the disc, the atmospheric temperature is even higher than T_{irr}. This would break our assumption that the irradiation temperature serves as the thermodynamic limit to the atmospheric temperatures, however, we can expect the inner part of the disc to exhibit some discrepancy. In reality, the disc must be strongly irradiated through the inner edge, which is not accounted for in FARGO_THORIN. Even so, the irradiation and atmospheric temperatures of the numerical model fail to reach the temperature profile of the kinematic model.

4.2.5 Artificially increasing stellar irradiation

In the models discussed so far, the irradiation temperature T_{irr} is lower than the profile given by the kinematic model. It is worth considering whether stellar irradiation isn't systematically underestimated in the model. Both the analytical models and numerical models indicate a disc with an almost constant aspect ratio. But the disc is very close to the star so heating by irradiation is to be expected. We experimented with artificially raising the temperature of the central star to compensate for the possibility that the numerical model underestimates the irradiation temperature. We leave all parameters equal to the case plotted in fig. 4.10, but we increased the temperature of the central star to 50000 K (tab. 4.6).

Table 4.6: Model with artificially increased stellar irradiation

Parameter	Unit	Value
$T_\star$	K	50000

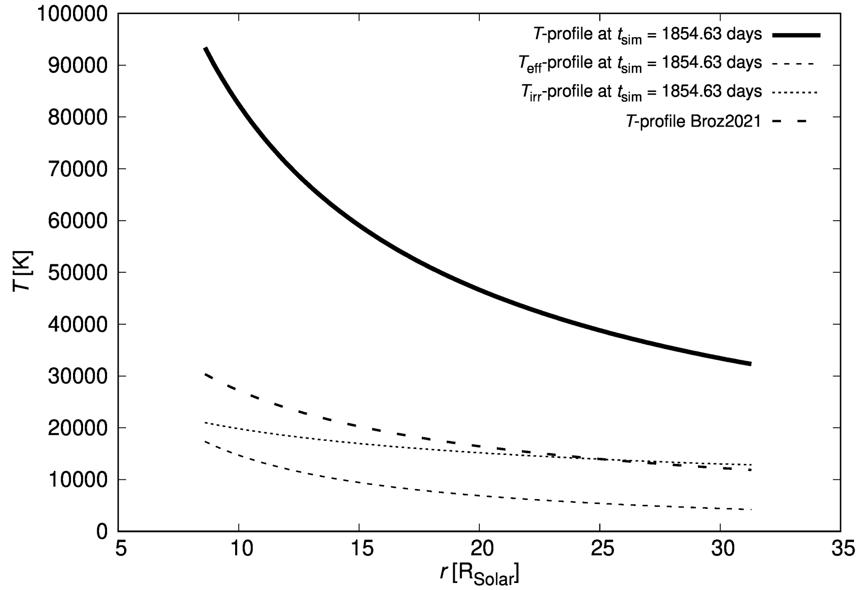

Figure 4.18: Temperature profiles of the model defined by parameters in tab. 4.6. For a full description of the notation see 4.1.3. In this model, stellar irradiation was artificially increased by assuming a star with higher effective temperature.

Discussion of a model with an artificially increased stellar irradiation
In fig. 4.18, we plotted the temperature profiles for this model. We see that by increasing stellar irradiation we can achieve a good agreement of T_{irr} with the profile of the kinematic model in the outer part of the disc. In the inner part of the disc, we may attribute the discrepancy to the lack of edge irradiation in the numerical model and to weak observational constraints of the kinematic model. The increase in the effective temperature of the central star has some effects on the midplane and atmospheric temperatures only within the uncertainty set by comparing the results from two different opacity tables as discussed in section 4.2.3. Other studied hydrodynamical quantities were effected negligibly. We will discuss the implications of this possibility in the conclusions.

4.2.6 Models with a high α viscosity parameter

The analytical models presented in chapter 3 show that a higher α will imply a lower temperature profile. In this section, we present models for the limit case of $\alpha = 1.0$. The reason for 1.0 being the limiting value of the α parameter were discussed in section 1.2.4.4. We also present a model for $\alpha = 1.5$, which is beyond the limit. The classical discussion of the size of α is dependent on a single (dominant) source of viscosity. In fact, without a full theory of viscosity on the microscopic scale, this limit is not guaranteed. It is possible that several different mechanisms of the angular momentum transfer may be present at once. For example, in chapter 3, while discussing the sound speed timescale, we discussed a mechanism for adding a negative angular momentum via spiral waves, this could lead to an increase of the α parameter.

Table 4.7: Models with a high α viscosity parameter input parameters

Parameter	Unit	Value
$M_\star$	$M_\odot$	13.048
R_{innb}	$R_\odot$	5.987
R_{outnb}	$R_\odot$	31.5
$\dot{M}$	$M_\odot \cdot \mathrm{yr}^{-1}$	$2 \cdot 10^{-5}$
Σ_0	$\mathrm{kg} \cdot \mathrm{m}^{-2}$	26332.9
σ_0	1	0.42
$\left(\frac{H}{r}\right)_0$	1	0.05
κ	$\mathrm{cm}^2 \cdot \mathrm{g}^{-1}$	[Zhu et al., 2012]
C_{k}	1	0.6
α	1	1.0 and 1.5
γ	1	1.4
μ	AMU	0.5
$T_\star$	K	30000
$R_\star$	$R_\odot$	5.987
A	1	0.0
t_{total}	yr	5
N_{r}	1	200
N_ϕ	1	2

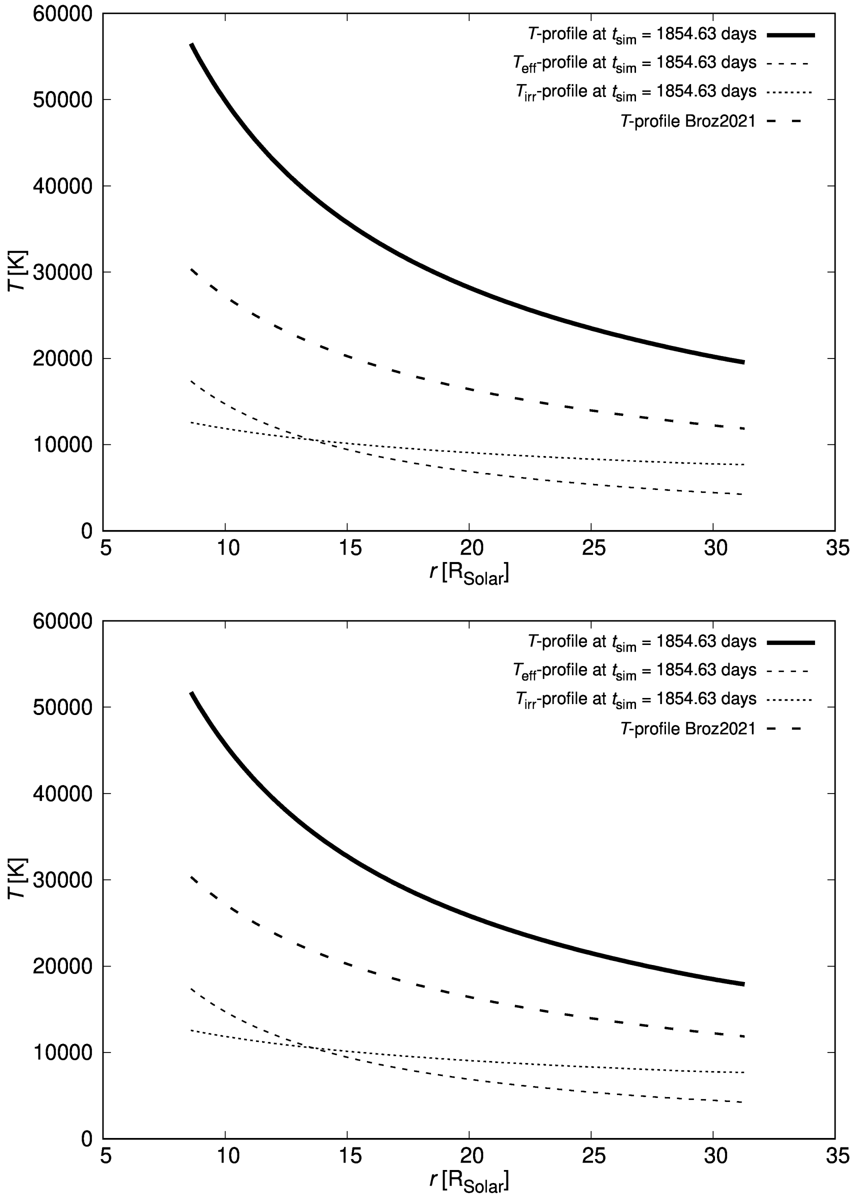

Figure 4.19: Temperature profiles of the models defined by parameters in tab. 4.7. For a full description of the notation see 4.1.3. These models assume $\alpha = 1.0$ (top) and 1.5 (bottom).

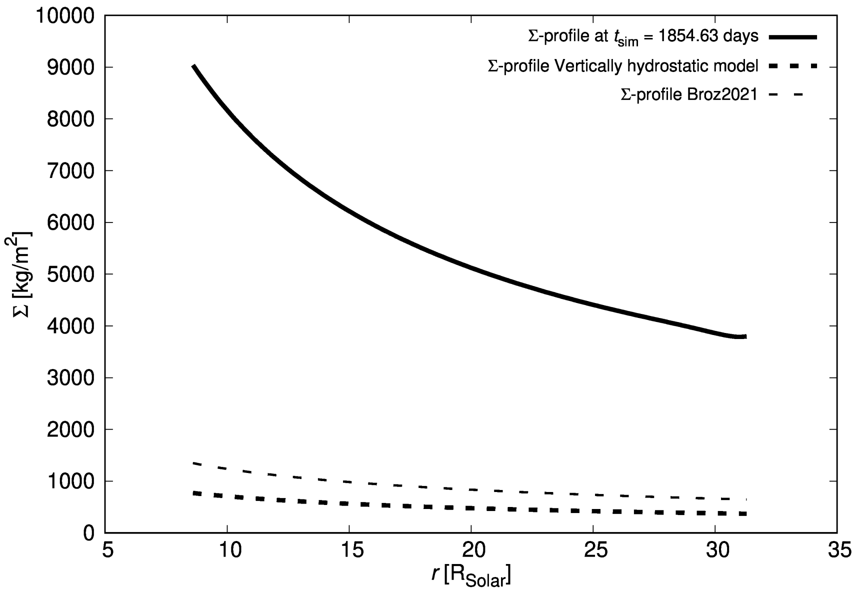

Figure 4.20: Σ profile of the model defined by parameters in tab. 4.7. For a full description of the notation see 4.1.3. This models assumes $\alpha = 1.0$.

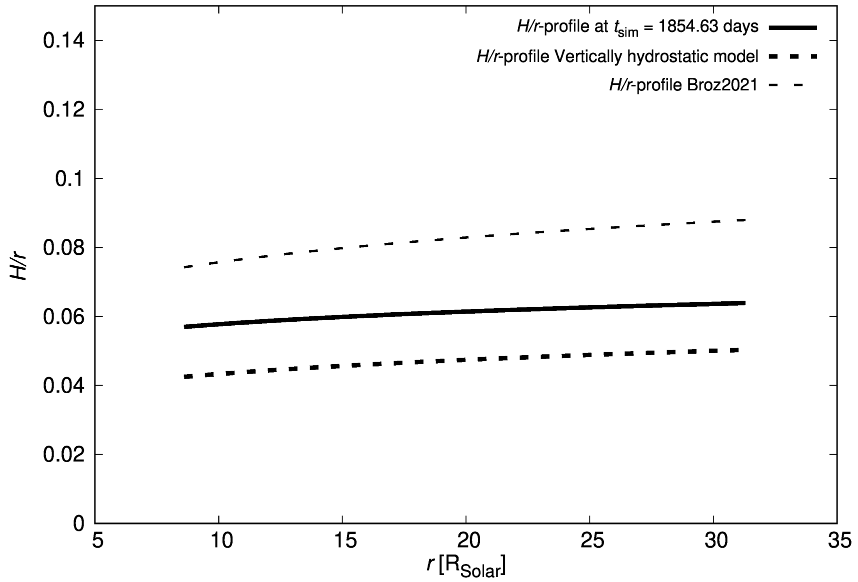

Figure 4.21: Aspect ratio profile of the model defined by parameters in tab. 4.7. For a full description of the notation see 4.1.3. This models assumes $\alpha = 1.0$.

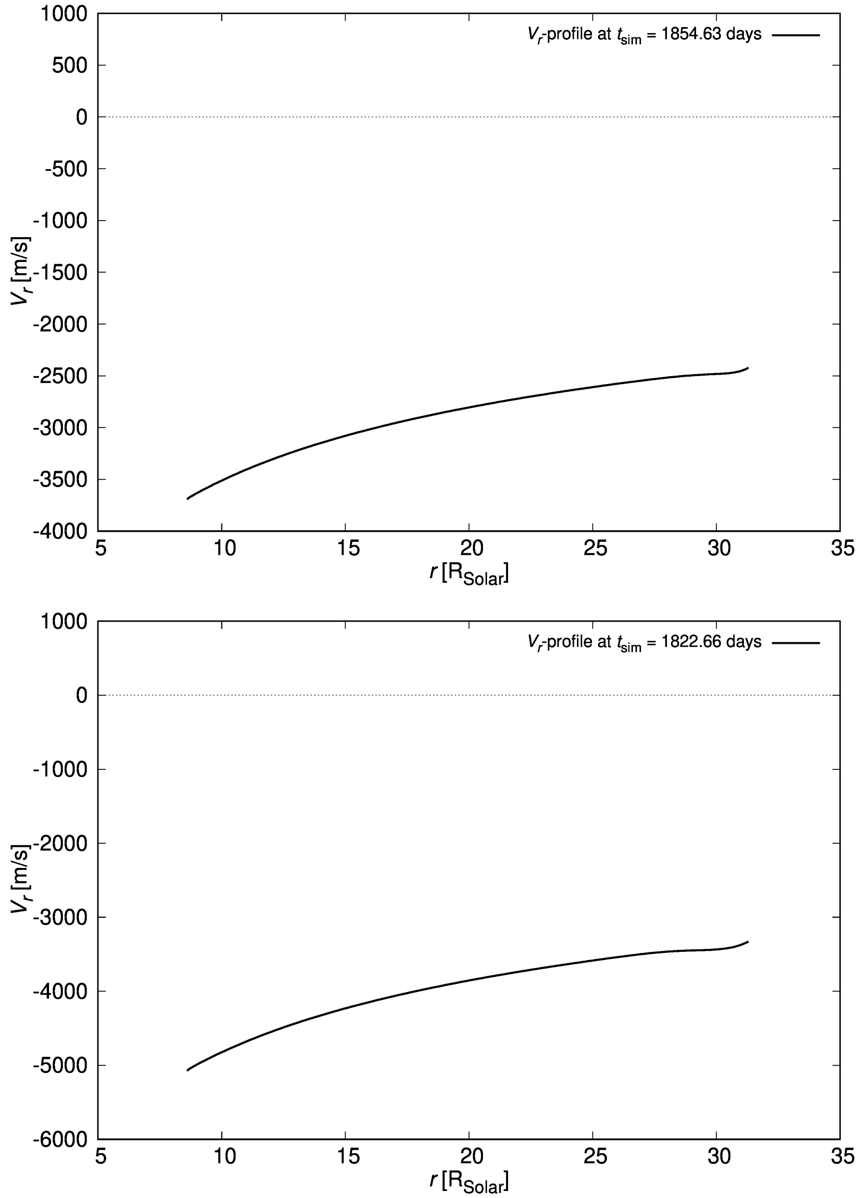

Figure 4.22: v_r profile of the model defined by parameters in tab. 4.7. For a full description of the notation see 4.1.3. This models assumes $\alpha = 1.0$.

Discussion of models with a high α viscosity parameter

- Both α models stopped showing temporal evolution within a year and a half of the simulation time in all studied quantities.
- In figures 4.19 and 4.20, we see a significant decrease in the difference between the here described numerical models and the kinematic model. The high α parameters logically decrease the vertically integrated densities by an order of magnitude. Fig. 4.22 confirms that the decrease in density is accompanied by an increase in radial velocities, keeping $\dot{M}$ constant throughout the disc. The temperatures decreased by almost half, this also implies a decrease in the aspect ratio (fig. 4.21), in the direction towards the "Vertically hydrostatic model".
- With a high α, the rate of angular momentum transfer is also high. Hence, we obtain the radial velocities approximately a hundred times the magnitude in the other simulations.

4.3 Modification of FARGO_THORIN to account for the radiation pressure

In our initial considerations of the β Lyr system, it was not clear how important the radiation pressure be in the dynamics (statics) of the system. We came up with a simple way of accounting for an additional pressure contribution due to radiation. We expect that radiation pressure will play a role mainly in mechanical processes, hence we introduced two new parameters in the model.

- The definition of H holds for an ideal gas but Montesinos et al. [2021] show that when the radiation pressure is accounted for, the pressure scale height changes by a specific factor. They also introduce a numerical scheme to implicitly find this parameter. We introduced this factor into our model in a simplified way, as a fixed parameter of the model:

  $$H_{\mathrm{r+p}} = hH\,, \tag{4.6}$$

  where h denotes the scale-height factor, it is dimensionless, H is the pressure scale height defined for the ideal gas and $H_{\mathrm{r+p}}$ is the pressure scale height with the radiation pressure accounted for. We modified the code so that H always follows this equation.
- The pressure also plays a role in the mechanics of the system, hence we introduced an additional dimensionless p factor as follows:

  $$P_{\mathrm{g}} + P_{\mathrm{r}} = pP_{\mathrm{g}}\,, \tag{4.7}$$

  in situations where the mechanics is of concern. As before, P_{g} denotes the ideal gas pressure and P_{r} the radiation pressure. That is the FARGO_THORIN hydrodynamical equations were modified to:

  $$\frac{\partial \Sigma}{\partial t} + \nabla \cdot (\Sigma v) = 0\,, \tag{4.8}$$

  $$\frac{\partial \boldsymbol{v}}{\partial t} + \boldsymbol{v} \cdot \nabla \boldsymbol{v} = -\frac{1}{\Sigma} p \nabla P + \frac{1}{\Sigma} \nabla \cdot \boldsymbol{\pi} - \frac{\int \rho \nabla \Phi \mathrm{d}z}{\Sigma}\,, \tag{4.9}$$

  $$\frac{\partial \epsilon}{\partial t} + \nabla \cdot (\epsilon \boldsymbol{v}) = -pP\nabla \cdot \boldsymbol{v} + Q_{\mathrm{visc}} + Q_{\mathrm{irr}} - Q_{\mathrm{rad}}\,, \tag{4.10}$$

  Where the sound speed is computed, the formula was modified to:

  $$c_s = \sqrt{\frac{pP_{\mathrm{g}}}{\rho}}\,. \tag{4.11}$$

We present a single simulation based on this modified version for the purpose of demonstrating its effects. We use the same set of parameters as described in sec. 4.2.1, but with the albedo set to zero, additionally we set the new parameters to:

Table 4.8: Models with the radiation pressure - input parameters

Parameter	Unit	Value
p	1	1.1
h	1	1.75

The value of p was estimated from the $P_{\mathrm{g}} \gg P_{\mathrm{r}}$, $\kappa = 10^{7.67}\rho^{0.72}T^{-0.1}$ analytical model (fig. 3.21) and h was estimated as the factor of the kinematic and "Vertically hydrostatic model".

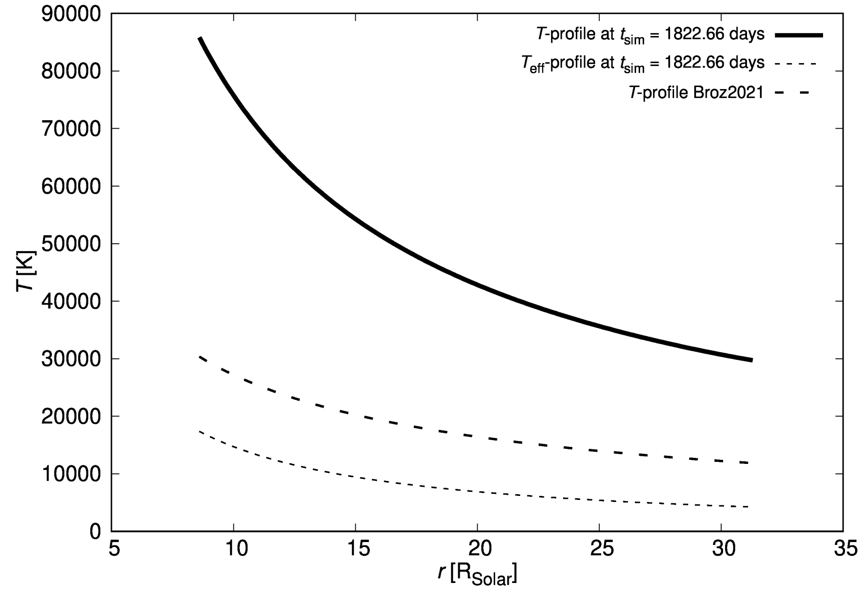

Figure 4.23: Temperature profiles to demonstrate the effects of including P_{r} in the FARGO_THORIN model (see sec. 4.3). For a full description of the notation see 4.1.3.

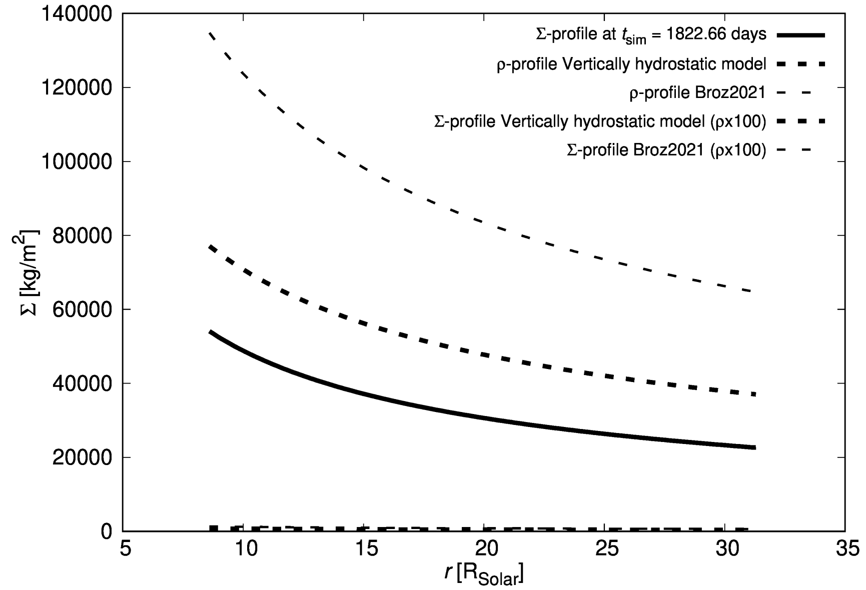

Figure 4.24: Σ profiles to demonstrate the effects of including P_{r} in the FARGO_THORIN model (see sec. 4.3). For a full description of the notation see 4.1.3.

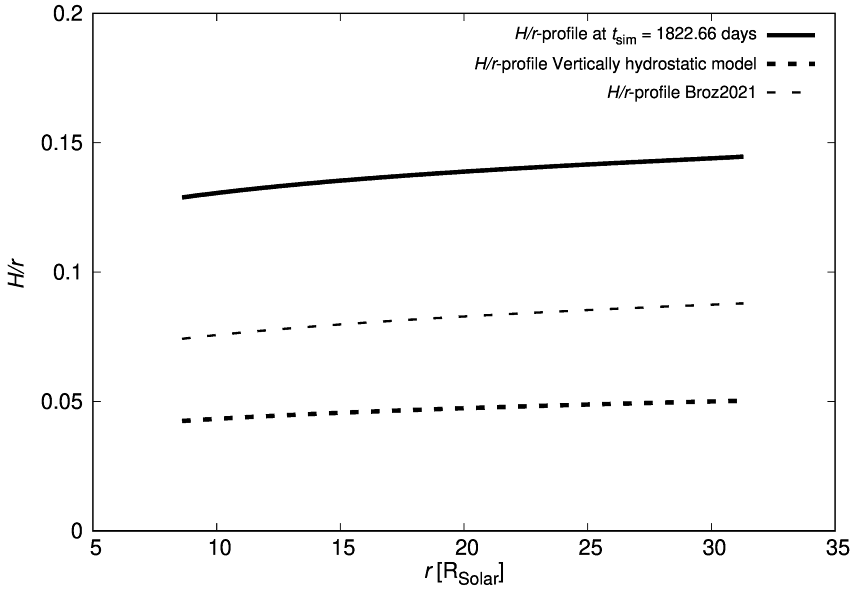

Figure 4.25: Aspect ratio profiles to demonstrate the effects of including P_{r} in the FARGO_THORIN model (see sec. 4.3). For a full description of the notation see 4.1.3.

Discussion of the modified FARGO_THORIN model

From the figures above, we observe the following coupled phenomenon caused by the introduction of radiation pressure into the model.

- The vertical hydrostatic equilibrium settles on a higher H values due to a larger pressure gradient acting against the gravity (fig. 4.25).
- The expansion to a higher pressure scale height results in a slight decrease of temperature (fig. 4.23), which intuitively follows from the ideal gas law.
- The vertically integrated density Σ remains the same (4.24). Considering that the amount of matter in the disc must remain the same and the H increased, this implies a decrease in the volumetric density ρ.
- The increase in the radial pressure gradient also results in the disc being slightly more sub-keplerian. Other studied quantities seem unaffected.

Conclusions

In this thesis, we computed a number of analytical models of accretions disks, derived as modifications of the classical models introduced by Shakura and Sunyaev [1973] or Pringle [1981]. We also computed numerical models, with the radiative hydrodynamic (RHD) code called FARGO_THORIN [Masset, 2002, Chrenko et al., 2017]. All these models were applied to the circumstellar disc observed in the β Lyræ A binary system. We always compared our results to the radiative-transfer kinematic model [Brož et al., 2021] that was constrained by photometric, spectroscopic and interferometric observations.

Let us briefly summarize the quantitative results implied by our modelling efforts.

- The midplane temperature of the disc is very high, $T_{\mathrm{mid}} \approx 10^5, \mathrm{K}$ on the inner edge and $3 \cdot 10^4, K$ on the outer edge.
- The irradiation T_{irr} and atmospheric T_{eff} temperatures are comparable to the kinematic model (30000 to 12000 K).
- The surface density Σ needed to sustain the mass transfer for $\alpha = 0.1$ is of the order of $10000\,\mathrm{kg\,m^{-2}}$. This is coupled with the radial velocities of the order of 100 of $\mathrm{m\,s^{-1}}$.
- The aspect ratio of $H/r \simeq 0.08$ found by Brož et al. [2021] is confirmed. In our model, we reach this value even at the hydrostatic equilibrium.
- From all our models, we infer that an α values of the order of 0.1 works best. This is in agreement with King et al. [2007] who collected evidence that for thin accretion discs, $\alpha = 0.1$ to 0.4.
- The opacity regime of the β Lyræ disc must be close to Krammer's opacity.

Hereinafter we summarize the problems and propose possible solutions.

- In order to reconcile our temperature profiles with those of the kinematic model we must consider a steep vertical temperature gradient.

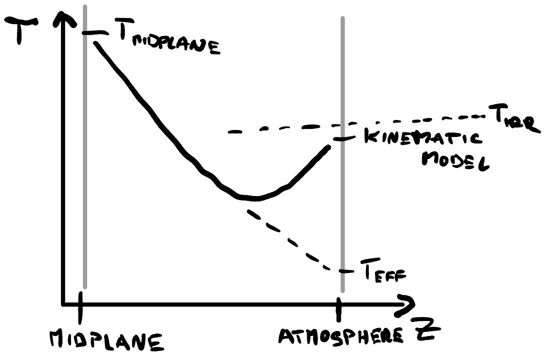

Figure 4.26: A non-artistic illustration of a proposed solution to the discrepancy between different temperatures, discussed in sec. 4.

  In fig. 4.26, we sketch a profile that could solve the discrepancy between different temperatures. The suggested atmosphere has a temperature inversion in the outer layers, not accounted for by the grey model of Hubený [1990]. Hence, the atmospheric temperatures may be lower than the ones inferred from observations. Moreover, the irradiation temperature serves as a thermodynamic limit to the atmospheric temperatures.

- Another solution to the temperature problem could be a vertical convective instability of the disc. Convective energy transfer would imply a shallow vertical temperature gradient, in other words, a more effective cooling. This way, lower mid-plane temperatures could be found, while keeping the same atmospheric temperatures.

- Another solution to the temperature problem could be a choice of α beyond the theoretical limit of 1. However, we prefer the solution with the steep vertical temperature gradients. The evidence from modeling and observations for $\alpha < 1$ corresponds to the theoretical limit [King et al., 2007].
- The aspect ratio may be further increased (even at lower mid-plane temperatures) by the radiation pressure gradients [Montesinos et al., 2021].

Bibliography

Rainer Arlt and Günther Rüdiger. Global accretion disk simulations of magneto-rotational instability. *A&A*, 374(3):1035–1048, 2001.

Steven A. Balbus and John F. Hawley. A Powerful Local Shear Instability in Weakly Magnetized Disks. I. Linear Analysis. *ApJ*, 376:214, July 1991. doi: 10.1086/170270.

Steven A. Balbus, John F. Hawley, and James M. Stone. Nonlinear Stability, Hydrodynamical Turbulence, and Transport in Disks. *ApJ*, 467:76, August 1996. doi: 10.1086/177585.

F.E. Baxandall and F.J.M. Stratton. *The Spectrum of B. Lyrae.* Annals of the Solar Physics Observatory, Cambridge. 1930. URL `https://books.google.cz/books?id=4FDhwAEACAAJ`.

K. R. Bell and D. N. C. Lin. Using FU Orionis Outbursts to Constrain Self-regulated Protostellar Disk Models. *ApJ*, 427:987, June 1994. doi: 10.1086/174206.

Henri Boffin. *Spiral Waves in Accretion Discs— Theory*, pages 69–87. 01 2008. ISBN 978-3-540-42213-6. doi: 10.1007/3-540-45339-3_6.

M. Brož, D. Mourard, J. Budaj, P. Harmanec, H. Schmitt, I. Tallon-Bosc, D. Bonneau, H. Božić, D. Gies, and M. Šlechta. Optically thin circumstellar medium in the β Lyr A system. *A&A*, 645:A51, January 2021. doi: 10.1051/0004-6361/202039035.

O. Chrenko, M. Brož, and M. Lambrechts. Eccentricity excitation and merging of planetary embryos heated by pebble accretion. *A&A*, 606:A114, October 2017. doi: 10.1051/0004-6361/201731033.

B. Czerny. *Accretion processes in astrophysics.* Nicolaus Copernicus centre for astronomy lecture series. 2019. URL `https://www.camk.edu.pl/en/archiwum/2019/08/14/accretion-processes-astrophysics/`.

M. de Val-Borro, R. G. Edgar, P. Artymowicz, P. Ciecielag, P. Cresswell, G. D'Angelo, E. J. Delgado-Donate, G. Dirksen, S. Fromang, A. Gawryszczak, H. Klahr, W. Kley, W. Lyra, F. Masset, G. Mellema, R. P. Nelson, S. J. Paardekooper, A. Peplinski, A. Pierens, T. Plewa, K. Rice, C. Schäfer, and R. Speith. A comparative study of disc-planet interaction. *MNRAS*, 370(2):529–558, August 2006. doi: 10.1111/j.1365-2966.2006.10488.x.

M. Flock, S. Fromang, N. J. Turner, and M. Benisty. Radiation Hydrodynamics Models of the Inner Rim in Protoplanetary Disks. *ApJ*, 827(2):144, August 2016. doi: 10.3847/0004-637X/827/2/144.

P. Harmanec. The ever challenging emission-line binary β lyrae. *Astronomische Nachrichten*, 323(2): 87–98, 2002.

I. Hubený. Vertical Structure of Accretion Disks: A Simplified Analytical Model. *ApJ*, 351:632, March 1990. doi: 10.1086/168501.

V. Karas. *Astrophysical Analogies: From quasars to pulsars.* Charles University lecture notes. 1996. URL `https://astro.mff.cuni.cz/vyuka/AST024/a.ps`.

Shigeo S. Kimura, Masanobu Kunitomo, and Sanemichi Z. Takahashi. From birth to death of protoplanetary discs: modelling their formation, evolution and dispersal. *MNRAS*, 461(2):2257–2265, September 2016. doi: 10.1093/mnras/stw1531.

A. R. King, J. E. Pringle, and M. Livio. Accretion disc viscosity: how big is alpha? *Monthly Notices of the Royal Astronomical Society*, 376(4):1740–1746, 03 2007. ISSN 0035-8711. doi: 10.1111/j.1365-2966.2007.11556.x. URL `https://doi.org/10.1111/j.1365-2966.2007.11556.x`.

H. Klahr and W. Kley. 3D-radiation hydro simulations of disk-planet interactions. I. Numerical algorithm and test cases. *A&A*, 445(2):747–758, January 2006. doi: 10.1051/0004-6361:20053238.

W. Kley. Radiation hydrodynamics of the boundary layer in accretion disks. I - Numerical methods. *A&A*, 208(1-2):98–110, January 1989.

W. Kley, B. Bitsch, and H. Klahr. Planet migration in three-dimensional radiative discs. *A&A*, 506(2): 971–987, November 2009. doi: 10.1051/0004-6361/200912072.

L. D. Landau and E. M. Lifshitz.

C. D. Levermore and G. C. Pomraning. A flux-limited diffusion theory. *ApJ*, 248:321–334, August 1981. doi: 10.1086/159157.

F. Masset. FARGO: A fast eulerian transport algorithm for differentially rotating disks. *A&AS*, 141: 165–173, January 2000. doi: 10.1051/aas:2000116.

F. S. Masset. The co-orbital corotation torque in a viscous disk: Numerical simulations. *A&A*, 387: 605–623, May 2002. doi: 10.1051/0004-6361:20020240.

Matías Montesinos, Nicolás Cuello, Johan Olofsson, Jorge Cuadra, Amelia Bayo, Gesa H. M. Bertrang, and Clément Perrot. Radiative Scale Height and Shadows in Protoplanetary Disks. *ApJ*, 910(1):31, March 2021. doi: 10.3847/1538-4357/abe3fc.

D. Mourard, M. Brož, J. A. Nemravová, P. Harmanec, J. Budaj, F. Baron, J. D. Monnier, G. H. Schaefer, H. Schmitt, I. Tallon-Bosc, J. T. Armstrong, E. K. Baines, D. Bonneau, H. Božić, J. M. Clausse, C. Farrington, D. Gies, J. Juryšek, D. Korčáková, H. McAlister, A. Meilland, N. Nardetto, P. Svoboda, M. Šlechta, M. Wolf, and P. Zasche. Physical properties of β Lyrae A and its opaque accretion disk. *A&A*, 618:A112, October 2018. doi: 10.1051/0004-6361/201832952.

T. W. A. Müller and W. Kley. Circumstellar disks in binary star systems. Models for γ Cephei and α Centauri. *A&A*, 539:A18, March 2012. doi: 10.1051/0004-6361/201118202.

J. E. Pringle. Accretion discs in astrophysics. 19:137–162, January 1981. doi: 10.1146/annurev.aa.19.090181.001033.

Thomas Rivinius, Alex C. Carciofi, and Christophe Martayan. Classical Be stars. Rapidly rotating B stars with viscous Keplerian decretion disks. *A&A Rev.*, 21:69, October 2013. doi: 10.1007/s00159-013-0069-0.

Forrest J. Rogers and Carlos A. Iglesias. Rosseland Mean Opacities for Variable Compositions. *ApJ*, 401: 361, December 1992. doi: 10.1086/172066.

N. I. Shakura and R. A. Sunyaev. Black holes in binary systems. Observational appearance. *A&A*, 24: 337–355, January 1973.

N. I. Shakura and R. A. Sunyaev. A theory of the instability of disk accretion on to black holes and the variability of binary X-ray sources, galactic nuclei and quasars. *MNRAS*, 175:613–632, June 1976. doi: 10.1093/mnras/175.3.613.

James M. Stone and Michael L. Norman. ZEUS-2D: A Radiation Magnetohydrodynamics Code for Astrophysical Flows in Two Space Dimensions. I. The Hydrodynamic Algorithms and Tests. *ApJS*, 80: 753, June 1992. doi: 10.1086/191680.

Bram Van Leer. Towards the ultimate conservative difference scheme. iv. a new approach to numerical convection. *Journal of Computational Physics*, 23(3):276–299, 1977. ISSN 0021-9991. doi: https://doi.org/10.1016/0021-9991(77)90095-X. URL `https://www.sciencedirect.com/science/article/pii/002199917790095X`.

K. Vitovský. A study of the long-term brightness and colour variations of the Be star 88 Herculis. 2019.

B. Wie. *Space Vehicle Dynamics and Control*. AIAA education series. American Institute of Aeronautics and Astronautics, 1998. ISBN 9781563472619. URL `https://books.google.cz/books?id=n97tEQvNyVgC`.

Zhaohuan Zhu, Lee Hartmann, Richard P. Nelson, and Charles F. Gammie. Challenges in Forming Planets by Gravitational Instability: Disk Irradiation and Clump Migration, Accretion, and Tidal Destruction. *ApJ*, 746(1):110, February 2012. doi: 10.1088/0004-637X/746/1/110.

Ladislav Šubr and Michal Švanda. Cosmic electrodynamics (nast008).

A. Supplementary models

A.1 Models with opacity approximations used in the analytical models

In this appendix, we present two numerical models, complementary to two of the analytical models, derived in chapter 3. The two models that we consider to be most successful are:

- $P_r \ll P_g$, $\kappa = 10^{7.67}\rho^{0.72}T^{-0.1}$,
- $P_\mathrm{g} \gg P_\mathrm{r}$, $\kappa = 10^{18.6}\rho^{0.77}T^{-2.5}$,

we implemented these opacities also in FARGO_THORIN.

Table A.1: Models with opacity approximations used in the analytical models - input parameters

Parameter	Unit	Value
$M_\star$	$M_\odot$	13.048
R_innb	$R_\odot$	5.987
R_outnb	$R_\odot$	31.5
$\dot{M}$	$M_\odot \cdot \mathrm{yr}^{-1}$	$2 \cdot 10^{-5}$
Σ_0	$\mathrm{kg} \cdot \mathrm{m}^{-2}$	26332.9
σ_0	1	0.42
$\left(\frac{H}{r}\right)_0$	1	0.05
κ	$\mathrm{cm}^2 \cdot \mathrm{g}^{-1}$	$\kappa = 10^{7.67}\rho^{0.72}T^{-0.1}$ and $\kappa = 10^{18.6}\rho^{0.77}T^{-2.5}$
C_k	1	0.6
α	1	1.0 and 1.5
γ	1	1.4
μ	AMU	0.5
$T_\star$	K	30000
$R_\star$	$R_\odot$	5.987
A	1	0.0
t_total	yr	5
N_r	1	200
N_ϕ	1	2

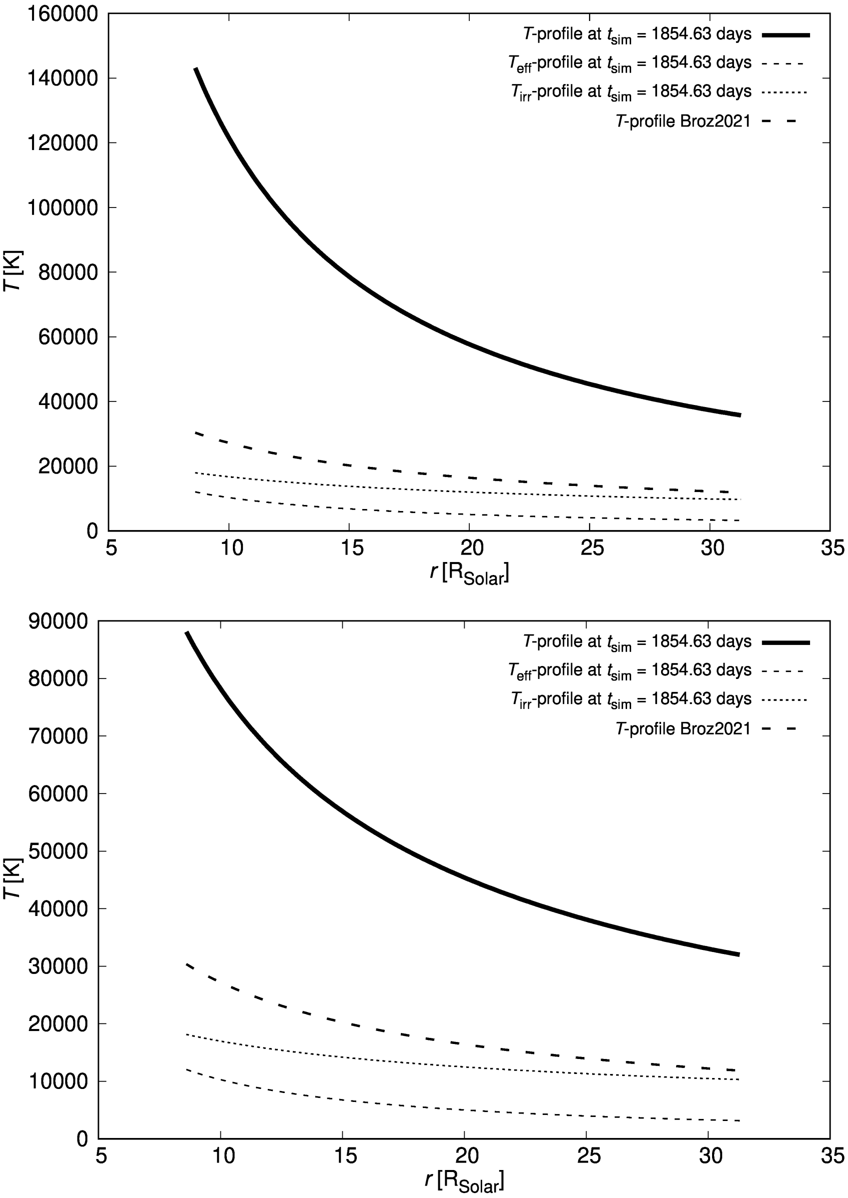

Figure A.1: Temperature profiles of numerical models based on the opacities from chapter 3. (Top) $P_{\rm g} \gg P_{\rm r}$, $\kappa = 10^{7.67}\rho^{0.72}T^{-0.1}$, (Bottom) $P_{\rm g} \gg P_{\rm r}$, $\kappa = 10^{18.6}\rho^{0.77}T^{-2.5}$. For a full description of the notation see sec. 4.1.3. The full set of parameters of this simulation is listed in tab. A.1

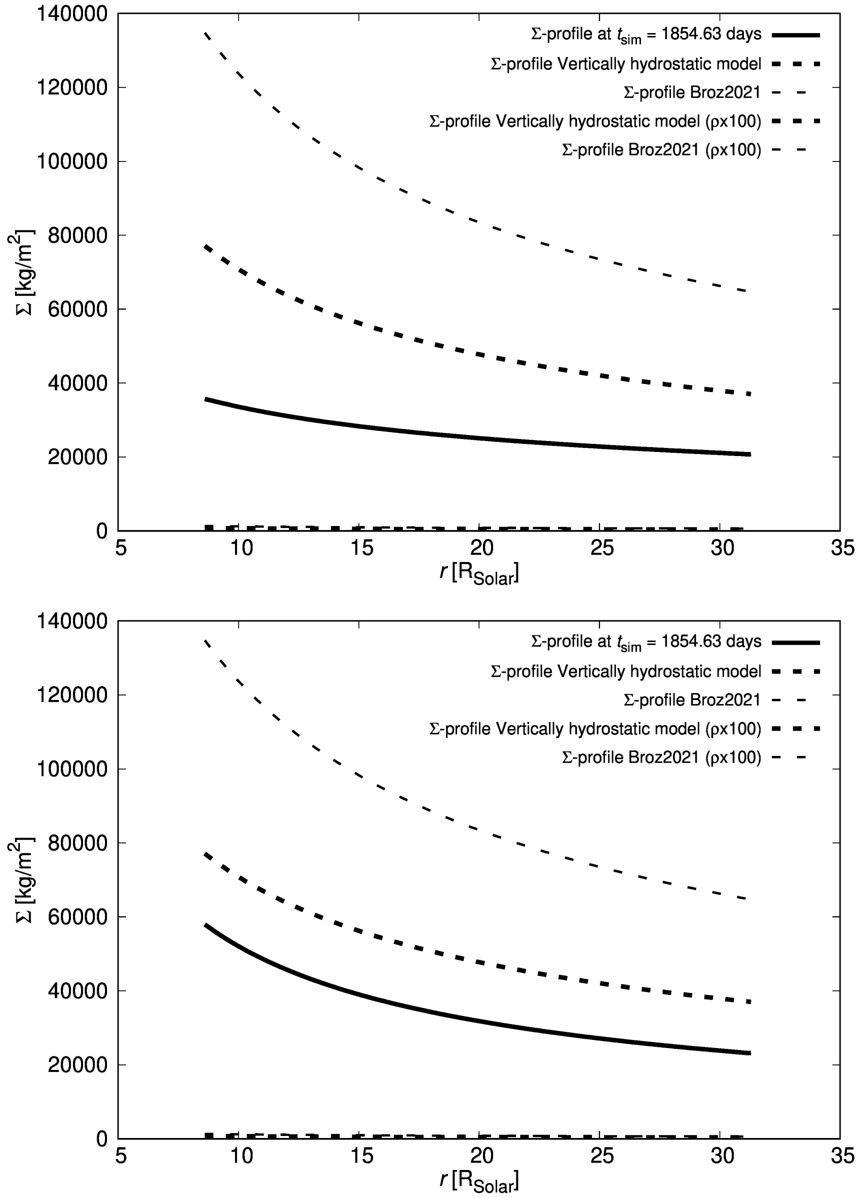

Figure A.2: Σ profiles of numerical models based on the opacities from chapter 3. For a full description of the notation see 4.1.3.

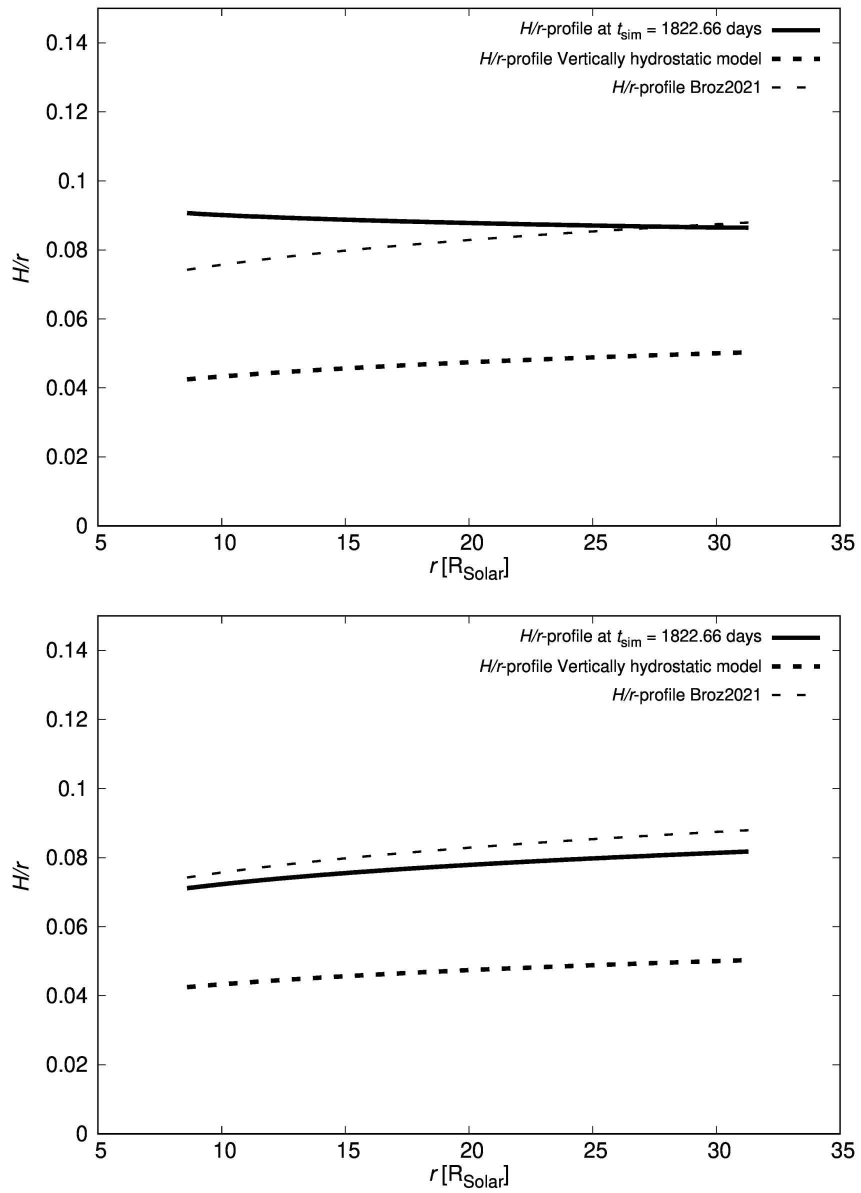

Figure A.3: Aspect ratio profiles of numerical models based on the opacities from chapter 3.For a full description of the notation see 4.1.3.

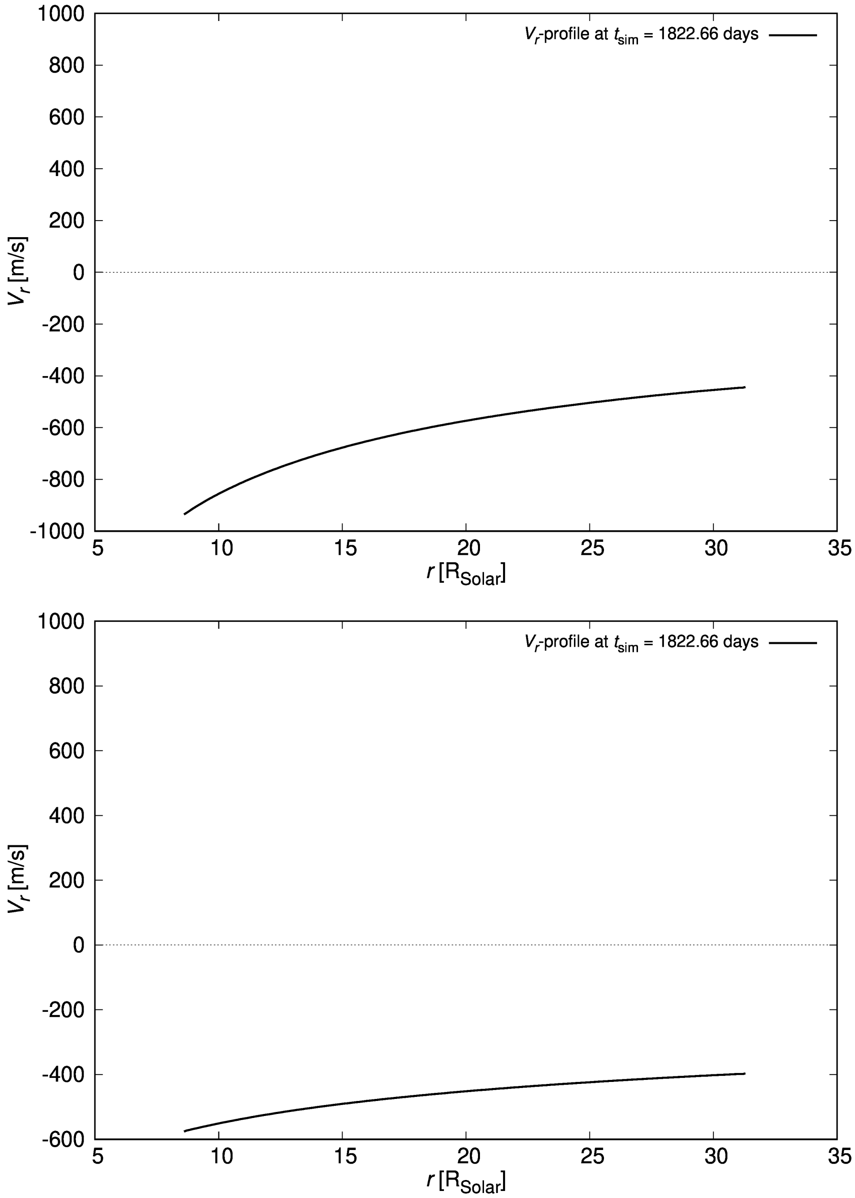

Figure A.4: v_r profiles of numerical models based on the opacities from chapter 3. For a full description of the notation see 4.1.3.

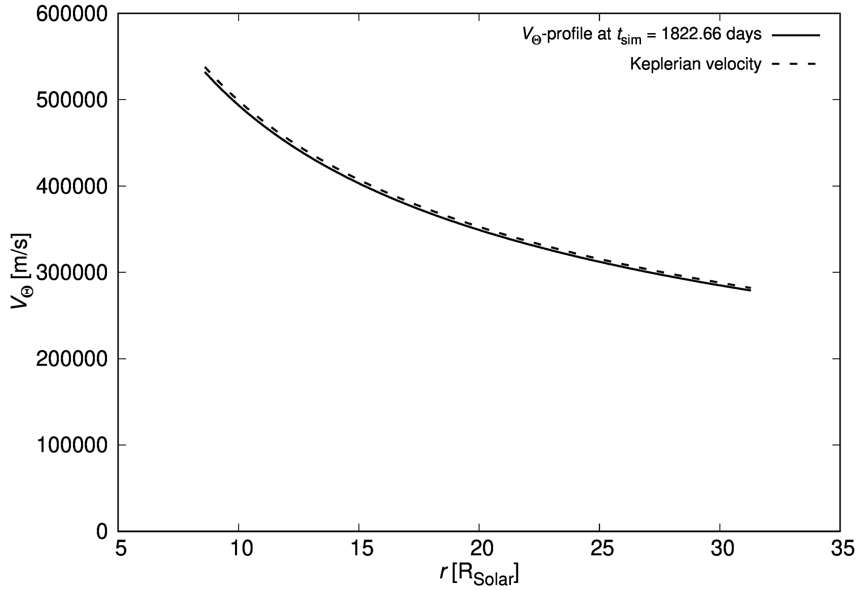

Figure A.5: The azimuthal velocity profile computed for a model analogous to the $P_{\rm g} \gg P_{\rm r}$, $\kappa = 10^{18.6}\rho^{0.77}T^{-2.5}$ analytical model derived in chapter 3. The full set of parameters of this simulation is listed in A.1.For a full description of the notation see 4.1.3.

Discussion of models with opacity approximations used in the analytical models

- The results of the simulation are plotted in figs. A.1,A.2,A.3, A.4 and A.5. The results are in good agreement with the analytical models. As was discussed in sec. 4.2.1, the analytical models are not simple power laws due to the term enforcing a boundary condition joining the azimuthal velocity of profile of the analytical models to an assumed sub-Keplerian rotation of the star. Since the disc is close to the star, this term can't be neglected completely even in the outer part of the disc. This pushes the analytical models to sligtly lower values of T, Σ and aspect ratio (see figs. 3.18,3.19 and 3.22 for $\kappa = 10^{18.6}\rho^{0.77}T^{-2.5}$ model and figs. 3.13, 3.14 and 3.16 for the $\kappa = 10^{7.67}\rho^{0.72}T^{-0.1}$ model.)
- The $\kappa = 10^{18.6}\rho^{0.77}T^{-2.5}$ closely resembles the numerical models with general opacity tables (see section 4.2.1). The Zhu et al. [2012] opacity tables places the disc into an opacity regime similar to the one of this analytical model. Calculated radial velocities A.4 are also in agreement with the numerical model from section 4.2.1.
- In fig. A.5 we confirm that the disc is close to Keplerian. Also, we stopped seeing temporal evolution in all profiles after about half of the simulation time had elapsed. Hence it seems that the profiles generated by the numerical model indicate that the disc can really be considered a standard Keplerian steady-state disc and follows the theory described in section 1.2.